IMPROVING BIOSENSOR PERFORMANCE USING MACHINE LEARNING AND

SIGNAL PROCESSING

By

Simon J. Ward

Dissertation

Submitted to the Faculty of the

Graduate School of Vanderbilt University

in partial fulfillment of the requirements

for the degree of

DOCTOR OF PHILOSOPHY

in

Electrical and Computer Engineering

May 10, 2024

Nashville, Tennessee

Approved:

Prof. Sharon M. Weiss, Ph.D.

Prof. Audrey K. Bowden, Ph.D.

Prof. Catie Chang, Ph.D.

Prof. Paul E. Laibinis, Ph.D.

Prof. Richard A. Peters, Ph.D.

To my beloved family.

ACKNOWLEDGEMENTS

I would like to first thank my family, in particular my wife Rachel, who has not only brought me great joy over these past few years, but is a formidable advocate, a comrade in the trenches, and best friend to celebrate successes and provide solace in the midst of defeat. Thank you to my family back in the UK, your boundless and unwavering support and encouragement have been a constant source of light in my life, which I have drawn on more than ever over the past five years. Thank you to Toni for making all of this happen, it wouldn't have been possible without your generosity and support. I will always cherish our adventures in the rain, meals at a particularly dependable restaurant, and much much more. Additionally, I thank all of my friends in the IMS program (both certified and honorary members), particularly Ryan who welcomed me into the fold, for the kindness they have shown me and for making Nashville feel like home when I arrived in the US. I would be remiss if I did not thank the chaps and Durham folks back in the UK for the laughs and your loyal friendship.

I am grateful to my committee members for their time, expertise, and uplifting and helpful dispositions, especially my advisor Prof. Sharon Weiss who has inspired, empowered, and invested in me to reach my full potential. I would like to thank all members of the Weiss and Ndukaife labs I had the pleasure of getting to know over the course of my PhD, for the banter, the bbqs, the practical jokes, the film nights, and camaraderie. KP, Yanrong, Josh, Sam, Ikjun, Theodore, Guodong, and others I got to know along the way, you all shaped my growth as a researcher and as a person, and I feel lucky to have gained many good friends. I thank in particular those with whom I worked closest. Tengfei, your unfailing optimism, patience, and generosity were a real blessing, as were your ground-breaking fruit experiments, thank you for graciously giving your time to help and teach me. Rabeb, you were a kindred spirit, thank you for your wisdom and

TABLE OF CONTENTS

LIST OF TABLES

LIST OF FIGURES

CHAPTER 1

Introduction

Parts of this chapter are adapted from "Morlet Wavelet Filtering and Phase Analysis to Reduce the Limit of Detection for Thin Film Optical Biosensors" published in ACS Sensors and reproduced with permission from publisher, and "Reduction in Sensor Response Time using Long Short-Term Memory Network Forecasting" published in SPIE Proceedings and reproduced with permission from publisher.

S. J. Ward, R. Layouni, S. Arshavsky-Graham, E. Segal, and S. M. Weiss, "Morlet Wavelet Filtering and Phase Analysis to Reduce the Limit of Detection for Thin Film Optical Biosensors," *ACS Sensors,* 6(8), 2967–2978 (2021).

S. J. Ward, and S. M. Weiss, "Reduction in Sensor Response Time using Long Short-Term Memory Network Forecasting," *Proc. SPIE,* 12675(126750E), 1–6 (2023).

Biosensors, devices to detect biological molecules, offer many advantages compared to alternative analytical tools, including compact form factor and portability; relative cost-effectiveness; ability to provide rapid detection of a wide range of analytes; and typically relatively simple operation and sample preparation. Biosensors are playing an increasingly important role in civilization today, with applications spanning medical diagnostics, food safety, and environmental monitoring [1–3]. However, the commercialization effort for the vast majority of biosensing platforms has been unfruitful, due in part to insufficient performance metrics, including detection limit, response time, stability and robustness, and specificity, which fail to meet the requirements

for many applications, offering little to no advantages above existing analytical tools and technologies [4–6]. The aim of this work is to enhance the performance, in particular the robustness, cost, response time, and detection limits of biosensors, using machine learning, statistics, and signal processing. To develop these methodologies, the platform of porous silicon (PSi) was used, which is a promising biosensing candidate due to its high surface area, strong light matter interaction with surface adsorbed molecules, and simple inexpensive fabrication [7]. However, the approaches presented in this thesis are designed, as far as possible, to be broadly applicable to any sensing modality.

In this chapter, a general description of biosensors and point-of-care diagnostics will be followed by discussion of machine learning, with a particular focus on relevant algorithms which have either previously had significant impact on the field of biosensing or other sensor technologies, or have great potential of improving biosensor performance. Subsequently, the nanomaterial and biosensing platform of PSi will be discussed, including formation, optical characterization, versatility (in terms of the diverse range of one-dimensional structures that are easily fabricable and commonly used), and the biosensing mechanism of PSi thin film structures. Finally, the current challenges facing wider biosensor adoption and commercialization are introduced, and steps towards addressing these challenges using machine learning and signal processing are presented in an overview of the dissertation.

1.1 Biosensors

Biosensors are self-contained integrated analytical devices, used to detect molecules of biological interest [8–10] which can range from biomarkers for disease providing critical medical

diagnostic information [3] to foodborne pathogens or allergens to ensure food safety [2] and heavy metals or pesticides providing crucial environmental monitoring [1]. Biosensors typically consist of three components. The first is a capture agent, which specifically binds to the target molecule in the analyte via a lock-and-key interaction such as enzyme-substrate interactions, antibody-antigen interactions, oligonucleotide interactions, or peptide interactions [11–13]. The second component of a biosensor is a transducer, which converts this binding into a measurable signal, via optical, electrochemical, thermal, or microelectromechanical means [5,14–18]. Finally, a data processing unit converts the transducer signal into the form of a useful output to the user. This framework differentiates biosensors from bioassays, which do not in general incorporate a transducer as an integral part of the analytical system. This thesis will focus on optical biosensors, specifically the platform of porous silicon (PSi).

To address the challenge of biosensor portability and cost, significant research effort has been devoted to developing point of care (POC) diagnostics which are operable by non-specialists in non-laboratory settings, providing fast and accurate results. These devices facilitate disease prevention and early detection, as well as management of medical conditions through continuous real-time monitoring, not just in wealthy geographic regions but also in resource-limited environments. The alternative is centralized clinical lab tests run on large and expensive instrumentation which can achieve impressive detection limits [19–23], but often have long associated test turn-around times: it can be days or weeks to receive a result. POC systems therefore are vital to enable earlier diagnoses to improve patient outcomes, continuous health monitoring, and more agile testing and tracking of fast-moving infectious diseases [24,25]. POC

tests have also been shown in many cases to reduce follow up clinical visits, better optimize treatment programs, and reduce the number and length of hospital visits [26,27].

Aside from glucose monitors which were the first example of a commercially successful biosensor [28], POC tests are usually paper-based [4,29], since paper is a cost-effective substrate which drives analyte flow through capillary forces and, to some extent, can provide filtering of non-target or contaminant molecules. Commonly used paper-based tests include pregnancy tests, and rapid diagnostic tests for diseases such as COVID, HIV, and Hepatitis C [30]. In addition, there has been much early stage development of POC tests incorporating smartphones [31]. For example, smartphone enabled POC tests have been used for genetic testing to detect multiple pathogens including E-coli [32], testing of sexually transmitted infections using the equivalent of an ELISA assay [33] and to demonstrate paper based colorimetric quantification by measuring pH [34]. Among the many advantages of using smartphones are their ubiquity, owned by roughly 66% of the world's population at the start of 2021 [31], their provision of increasingly expansive computing power, high quality cameras, their own light source in the form of the LED flashlight, and often an internet connection enabling cloud computing and data sharing.

1.2 Machine Learning

In the past few decades, machine learning has experienced a surge in research interest across almost every discipline, partly facilitated by the exponentially increasing volumes of data generated and accessible computational power. In the context of biosensing, machine learning has been used for the removal of background noise due to interference and biofouling [35], for pattern recognition to identify a molecule on the basis of its response to a sensor array [36], and for inverse

design of optical nanophotonic structures for sensing [37]. However, there is still huge untapped potential for machine learning to bridge the gap between the performance of current biosensor technologies and the requirements across a broad application space, to achieve clinical relevancy, among other goals. This thesis explores ways machine learning can be applied to biosensor data to overcome key challenges to commercialization.

The field of machine learning focuses on data-driven algorithms, which have the capacity to learn through experience [38]. Algorithms can either be supervised, for which training data includes associated 'ground truth' labels, unsupervised, where labels are either not provided or are unknown, or based on reinforcement learning, where an agent learns optimal behavior based on the rewards it receives. Supervised models can be further divided into classification algorithms, aiming to predict the category of a data example given some prior information, and regression algorithms, where instead of discrete categories the predicted output is a continuous variable. Unsupervised models consist of clustering algorithms, which group data points based on similarity in a particular metric, and dimensionality reduction algorithms, which are used to simplify the expression of the data with minimal information loss, useful for feature extraction, visualization, or noise reduction. Some of the machine learning tools most commonly utilized in this thesis are described below [35,39,40], and are illustrated in Figure 1.1.

1.2.1 Principal Component Analysis

Principal component analysis (PCA) (Figure 1.1 (a)) is an unsupervised statistical technique often used to reduce dimensionality of a dataset by finding and projecting the data onto orthogonal linear combinations of the original dimensions of the data, representing maximum variance in lower dimensional space [41]. The projections are the eigenvectors of the covariance

5

matrix of the data, with associated eigenvalues indicating the proportion of the variance that is represented. Often the number of projections is chosen such that they capture at least 95% of the original variance in the data.

1.2.2 Linear Discriminant Analysis

Linear Discriminant Analysis (LDA) (Figure 1.1 (b)) is a supervised statistical method often used to reduce dimensionality by determining a series of linear projections of a given dataset that best separate data points by their associated class [42]. This is achieved by solving the generalized eigenvalue problem for the ratio of between-class to with-in-class covariance matrices, which represents the maximum separation between classes with the tightest clusters within classes.

1.2.3 Support Vector Machines

Support vector machines (SVMs) (Figure 1.1 (c)) are supervised optimal margin classifiers, which have the advantages of interpretability, stability, and applicability to small datasets [43]. The power of SVMs lies in their compatibility with the 'kernel trick,' which allows the data to be mapped to a high (even infinite) number of dimensions, allowing SVMs to learn complex non-linear decision boundaries. Common kernels include linear, sigmoidal, polynomial, and radial bias function.

1.2.4 K Nearest Neighbor

The K-nearest-neighbor (KNN) algorithm (Figure 1.1 (d)) is one of the simplest classification methods, predicting class labels via a popular vote of the nearest k neighbors according to a pre-defined distance metric, and is particularly powerful when there is little prior knowledge about the underlying distribution of the data [44].

6

1.2.5 Artificial Neural Networks

Artificial neural networks (ANNs) (Figure 1.1 (g)) are universal approximators and are consequently able to learn features and relationships between features rather than requiring feature selection or prior knowledge of an analytical expression to fit the data [45,46]. As a result, ANNs need more training data, but when that requirement is satisfied, they can significantly outperform other machine learning approaches.

1.2.6 Random Forest

Random Forest classifiers (Figure 1.1 (f)) use a method of ensembling called 'bagging' to aggregate predictions of a multitude of decision tree classifiers [47,48]. Each decision tree is trained on a bootstrapped dataset, generated by sampling with replacement. Random forest significantly lessens the problem of overfitting often encountered when using individual decision trees.

1.2.7 Generalized Linear Models

Generalized Linear Models (GLMs) (Figure 1.1 (e)) were developed for application to data described by a distribution from the exponential family. Common examples are normally distributed continuous data which equates to linear regression, and Bernoulli distributed discrete data which corresponds to logistic regression [49].

1.2.8 Recurrent Neural Networks

Recurrent neural networks (RNNs) (Figure 1.1 (h)) are a variant of neural network which include an internal memory state, allowing predictions to be made using time series or sequential data as input, with the output dependent on both current and prior inputs [50]. The internal memory

is a summarization of relevant information from data seen earlier in the sequence, both in the near and distant past. Accordingly, RNNs are said to have an "infinite lookback window."

1.2.9 Long Short-Term Memory Networks

Long short-term memory (LSTM) networks (Figure 1.1 (i)), a variant of recurrent neural networks (RNN), were developed to address the issue of vanishing and exploding gradients that limit the ability of traditional RNNs to learn long-range dependencies in sequential data [51]. LSTMs have been widely applied to all manner of time series forecasting and anomaly detection tasks, amongst others, in domains ranging from machine health [52], to speech enhancement [53], weather forecasting [54], and text classification [55]. LSTM networks have much greater long-term memory of previous time points in sequential data than traditional RNNs, owing to the enhanced gradient flow in the network due to an internal memory which runs through each sequential LSTM cell, and is maintained with three gates. The first is the input gate, which determines the extent to which the current input to the LSTM cell should be stored in the internal cell memory, the second is the output gate which calculates the proportion of internal cell memory that should be included in the output of the cell, and the third is the forget gate which identifies less relevant information currently stored in the internal cell memory which should be forgotten. This architecture, enabling LSTMS to learn long and short-range dependencies in sequential data makes them particularly suitable to learn the complex kinetics of sensor responses such as the exposure of a target biomolecule to PSi biosensors
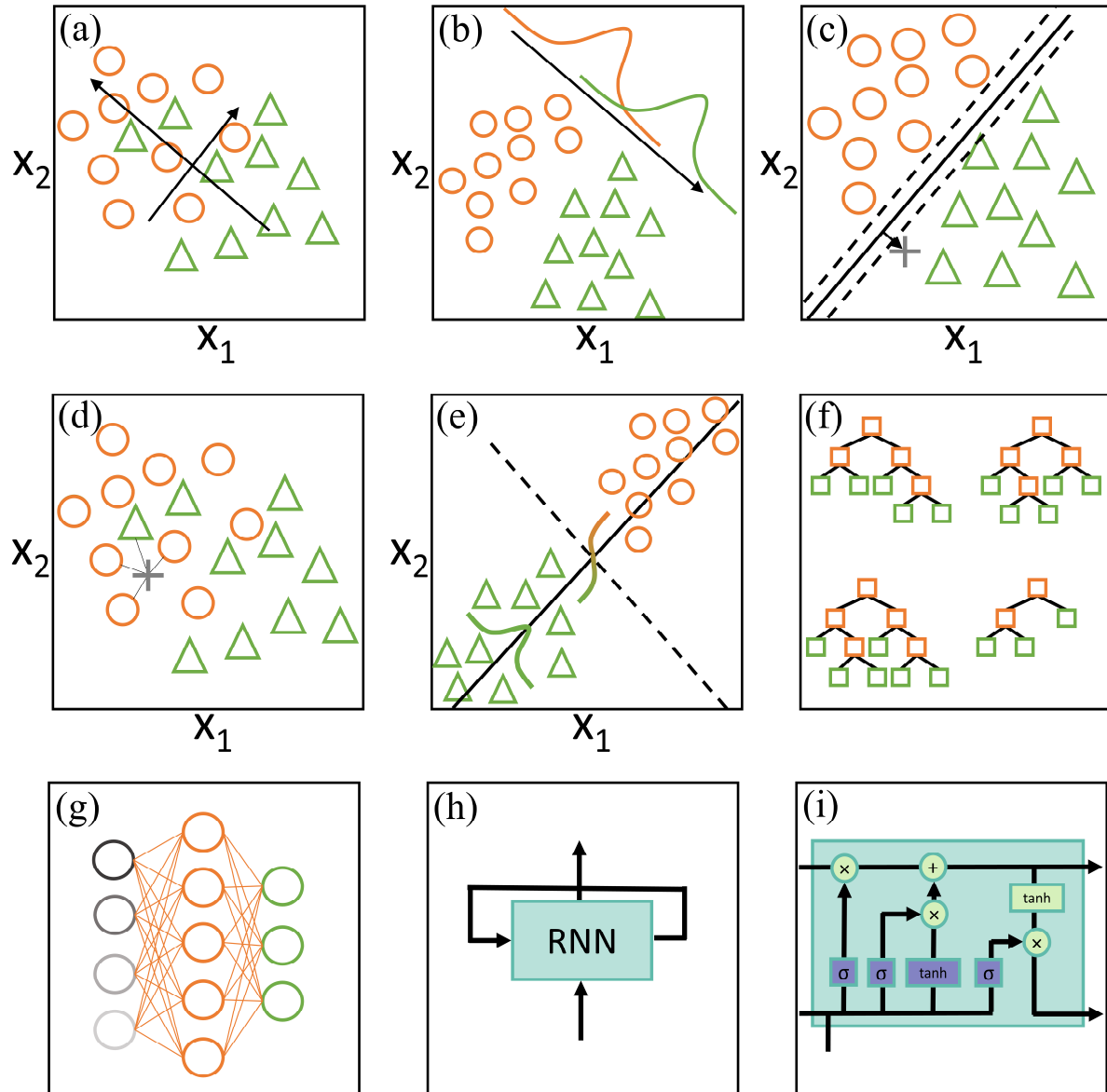
Figure 1.1. Illustrations of several common machine learning models, used for dimensionality reduction: (a) principal component analysis [41], and (b) linear discriminant analysis [42]; classification: (c) support vector machines [43], (d) k-nearest neighbour [44], (e) generalized linear models [49], and (f) random forest [47]; and deep learning models: (g) artificial neural networks [45], and (h) recurrent neural networks [50], (i) long-short term memory networks [51]

9

1.3 Porous Silicon (PSi)

There are many approaches to biosensing that have found success both academically and commercially, such as optical surface plasmon resonance [56], electronic FET-based [57], and electrochemical amperometric [58] biosensors. However, this thesis focuses on the optical biosensing platform of porous silicon (PSi), a nanomaterial originally discovered in the 1950s [59], which has been the subject of wide research interest for over two decades [60–63]. PSi is formed by electrochemical etching using a hydrofluoric acid (HF) electrolyte (Section 1.3.1). By tuning etch duration and etching current density to control layer thickness and pore size, PSi supports the design and easy fabrication of arbitrary 1D photonic structures (Section 1.3.4) without the need for cleanroom conditions, rendering PSi a tremendously versatile platform. Furthermore, unlike traditional colorimetric approaches which require, for example, a fluorescent species, nanoparticle aggregation, or an enzymatic reaction to cause a color change, PSi sensors can operate in a label-free manner while still experiencing a color change due to thin film interference. The advantages of PSi for sensing include a large surface area (> 100 m^2/cm^2) presenting many sites for molecular binding and enhanced light-matter interaction for surface adsorbed molecules, CMOS compatibility, low cost and scalable manufacture, and support of a wide range of surface chemistries. As a result, PSi biosensors show promise for use in POC devices. However, PSi faces many of the same challenges as other biosensing platforms, in particular poor mass transport [64–66] which hinders response times, and reduces sensitivity alongside unmitigated noise signatures which degrade signal to noise (S/N). These challenges restrict the benefits provided by the large surface area inside the pores. As a result of these limitations, typically it can take many hours for

a PSi biosensor to reach a stable equilibrium state, and detection limits often fall short of clinical

relevancy for many applications and lag behind other biosensing systems [63,67,68].

1.3.1 PSi Fabrication

A schematic diagram of the electrochemical etching cell typically used for PSi fabrication

is shown in Figure 1.2. A programmatically controlled current source is connected between a

platinum wire cathode, commonly in the form of a mesh or a spiral to achieve an approximately

uniform electric field, and an aluminum plate in contact with the bottom side of the silicon wafer

which acts as the anode. A current is applied through the HF/ethanol electrolyte, driving the

reaction between fluoride ions, silicon, and the positive charge carriers (holes) in the typically p-

doped silicon wafer, leading to anodization of the bulk silicon wafer. At sufficiently low current

densities, rather than etching away a homogeneous layer of silicon at the surface of the wafer,

known as electropolishing, nanoscale pore formation occurs.
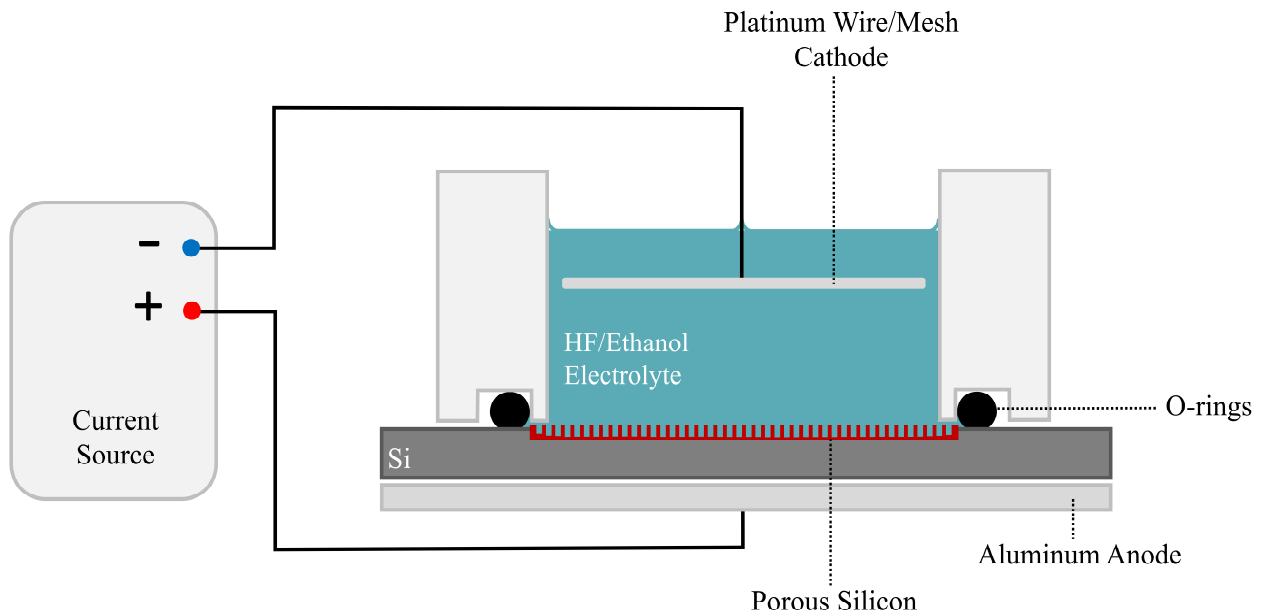
Figure 1.2. Illustration of an electrochemical etch cell used for porous silicon etching.

This process is a result of a combination of effects including instability of Si-H bonds, which are more strained in the $\langle 100 \rangle$ compared to the $\langle 111 \rangle$ crystal direction; charge carrier depletion in the pore walls compared to the bulk silicon due to resistive and space charge limited transport; and enhancement of the electric field driving the reaction at the tips of the pores due to the high radius of curvature of the silicon [7]. Top view and cross-sectional scanning electron microscopy (SEM) images of PSi shown in Figure 1.3 reveal that the pores propagate unidirectionally into the silicon wafer, with little interconnection, and that the pores are not of uniform size but follow a distribution dictated by the etching current density. For a given current density, the etch rate, pore size and morphology, and porosity are determined by the electrolyte concentration, level of doping in the Si wafer, and to a lesser extent temperature and photon flux.
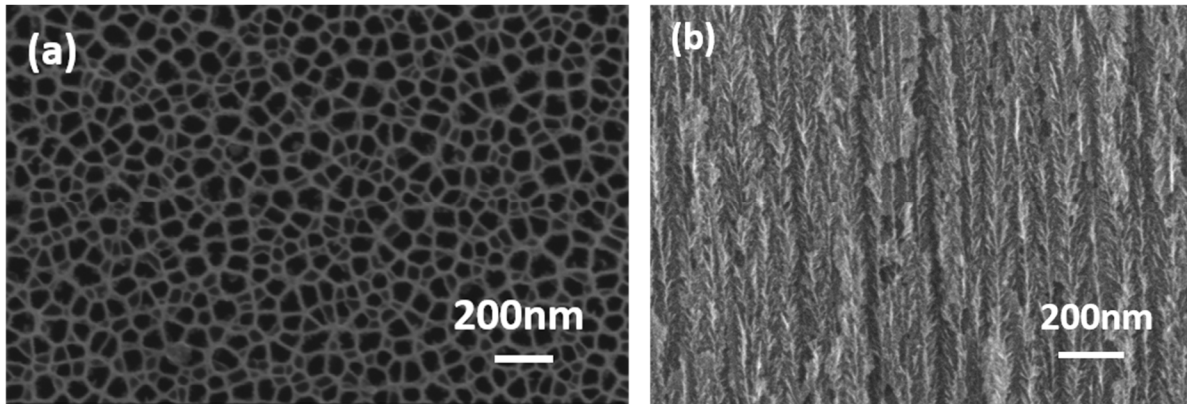
Figure 1.3. SEM images of PSi showing (a) top view and (b) cross sectional profile of the nanoporous structure.

1.3.2 Effective Index Approximation

PSi is not a uniform material with a single well-defined refractive index across all size scales, since a PSi film is comprised of silicon and in varying proportions. However, because the characteristic pore size of PSi films is much smaller than the shortest wavelength of visible light, PSi can be treated as a uniform effective medium, and hence the optical thickness and refractive index are referred to as the effective optical thickness and effective refractive index, respectively [69]. For PSi biosensing applications where the pores are partially filled with molecules, the effective refractive index of PSi depends on the volume fraction of air, silicon, and biological molecules in the pores. This relationship can be approximated using an effective medium approximation, such as those proposed by Maxwell Garnett [70], Bruggeman [71], and Looyenga [72]. Typically the Bruggeman effective index theory is used, since it is better suited for the irregularly shaped pores and relatively low porosities characteristic of PSi [69] and is usually in best agreement with experimental observations [73–75], which can be expressed as:

$$v_{Si}\frac{n_{Si}^2 - n_{PSi}^2}{n_{Si}^2 + 2n_{PSi}^2} + v_{void}\frac{n_{void}^2 - n_{PSi}^2}{n_{void}^2 + 2n_{PSi}^2} + v_{bio}\frac{n_{bio}^2 - n_{PSi}^2}{n_{bio}^2 + 2n_{PSi}^2} = 0 \qquad (1.1)$$

where v_{Si}, v_{void} and v_{bio} are the volume fraction of silicon, air, void space and biological material respectively, and $v_{Si} + v_{void} + v_{bio} = 1$. This predicts a roughly linearly decreasing trend of effective refractive index with increasing porosity $(1 - v_{Si})$, shown in Figure 1.4, and a linearly increasing trend in effective refractive index as the volume fraction of biological material – surface adsorbed biomolecules – increases.

13
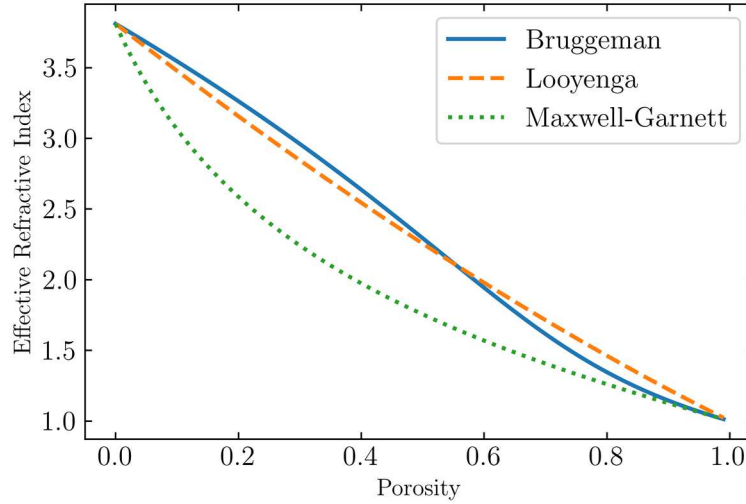
Figure 1.4. Comparison of three commonly used effective medium approximations, Bruggeman [71], Looyenga [72], and Maxwell-Garnett [70], used to calculate porous silicon effective refractive index as a function of porosity.

1.3.3 PSi 1D Photonic Structures

One unique advantage of PSi is the ease with which one dimensional stacks of layers with arbitrary effective refractive indices and thicknesses can be fabricated through the alteration of the current density during the etching process.

Single Layer

The simplest PSi structure most commonly used for biosensing is a single PSi layer, also termed a thin film interferometer, etched with constant current density. The reflectance spectrum of a thin film PSi layer is characterized by Fabry-Pérot fringes [76] (Figure 1.5 (a)), which are caused by interference from successive reflections from the front and back faces of the film. The reflectance of a prototypical Fabry-Pérot etalon, R_{tf}, is given in Eqn. (1.1).

$$R_{tf} = \frac{2R(1 - cos\phi)}{(1 - 2Rcos\phi + R^2)} \qquad (1.1)$$

14

In this equation, R is the square of the reflection coefficient at a single interface (i.e., $R = |r|^2$ where r is the Fresnel amplitude reflection coefficient). The round-trip phase shift is given by $\phi = \frac{4\pi nL}{\lambda}$, where n is the effective refractive index of the thin film, L is the thickness of the film which must be less than the coherence length of the incident light, and λ is the wavelength of light. The derivation of Eqn. (1.1) assumes negligible absorption, normal incidence of light on the thin film, and that the front and back sides of the thin film interface with the same material. The latter assumption is not strictly valid for many thin film sensors, which often interface with a solution of biomolecules at the front surface and a substrate with a different effective refractive index at the back surface. Accordingly, for many thin film sensors, the intensity of reflected light will be modified from the ideal Fabry-Pérot etalon case, and there may be a π phase shift in the Fabry-Pérot fringes. Nevertheless, the relationship indicated by Eqn. (1.1) that minima in reflectance spectra occur at $\phi = 2\pi m$, where $m = 0,1,2 \dots$, holds for all thin film sensors. This phase relationship corresponds to wavelengths that satisfy the relation, $2nL = m\lambda$. Hence, plotting R_{tf} against inverse wavelength (i.e., wavenumber) will yield a series of equally spaced sinusoidal fringes if no external noise sources are considered. The frequency of these fringes, directly proportional to the product of the thickness and effective refractive index of the thin film (2nL), is known as the effective optical thickness (EOT). Consequently, such reflectance spectra are well-suited to fast Fourier transform (FFT) processing, which in the ideal case contains a single peak analogous to the Fourier transform of a sine wave mapping to a Dirac delta function, and in practice allows identification of the dominant peak corresponding to the effective optical thickness as discussed further in chapter 2. We note that since the independent variable – wavenumber – is in

15

units of inverse distance, the frequency of the reflectance fringes is given, in this case, in units of distance.

Double Layer

Another simple type of PSi structure consists of a stack of two PSi thin film layers with different effective refractive indices, fabricated using two different current densities. The reflectance spectra of a double layer PSi structure (Figure 1.5 (b)) can be intuitively understood by considering partitioning of the structure into an upper layer, a lower layer, and a layer which encompasses the entire double layer structure, which have optical thicknesses $EOT_{upperlayer}$, $EOT_{lowerlayer}$, and $EOT_{doublelayer}$, respectively. The optical thicknesses are related as follows: $EOT_{doublelayer} = EOT_{upperlayer} + EOT_{lowerlayer}$. Light can be reflected at the interface of each of these layers, and as a result, the reflectance spectrum in Figure 1.5 (b) is a superposition of sinusoidal Fabry-Pérot fringes with three distinct frequencies corresponding to the three different EOTs, each clearly visible in the FFT spectrum.

Bragg Mirror

Bragg mirrors are formed by an alternating pair of layers with carefully designed thicknesses and effective refractive indices to give theoretically 100% reflectance around a central wavelength. While the effective refractive index of each of the two layers is different, the EOT of both is the same due to different thicknesses for each of the two layers, and is equal to one quarter of the central wavelength of the high reflectance stop band. As such, Bragg mirrors are often referred to as quarter-wavelength stacks. This EOT ensures that reflected light undergoes perfect constructive interference and transmitted light undergoes perfect destructive interference. Bragg

stacks are commonly used for optical components such as filters and mirrors. The index contrast between the two layers is proportional to the width of the high reflectance stop band. A narrow band Bragg mirror with low index contrast is shown in Figure 1.5 (c). For extremely narrow stop bands, rather than having discrete steps between the two effective refractive indices of the two layers, current density can be continuously varied to give a sinusoidally varying effective refractive index, which is known as a rugate filter. This can be intuitively thought of as the inverse case to the single layer, in terms of Fourier analysis. Rather than a sinusoidal reflectance spectrum with a single Dirac delta function peak in the Fourier domain corresponding to one layer with a single EOT, the sinusoidally varying EOT for an effectively infinite number of layers gives an approximately sinusoidally varying spectrum in the Fourier domain. Under the inverse Fourier transform this gives a single Dirac delta function peak in the reflectance spectrum, which manifests as a narrow high reflectance stopband with a width theoretically approaching an infinitesimally small value.

Microcavity

The microcavity is closely related to the Bragg mirror, with identical structure apart from a cavity introduced by inverting the alternating sequence of the pair of layers in the middle of the stack, which creates an imperfection in the periodic structure. This inversion leads to a half-wavelength thickness layer, bounded by two perfect Bragg reflectors, which confines light and, in the reflectance spectrum, leads to a sharp resonant dip at the central wavelength in the otherwise high reflectance Bragg mirror stop band, illustrated in Figure 1.5 (d).
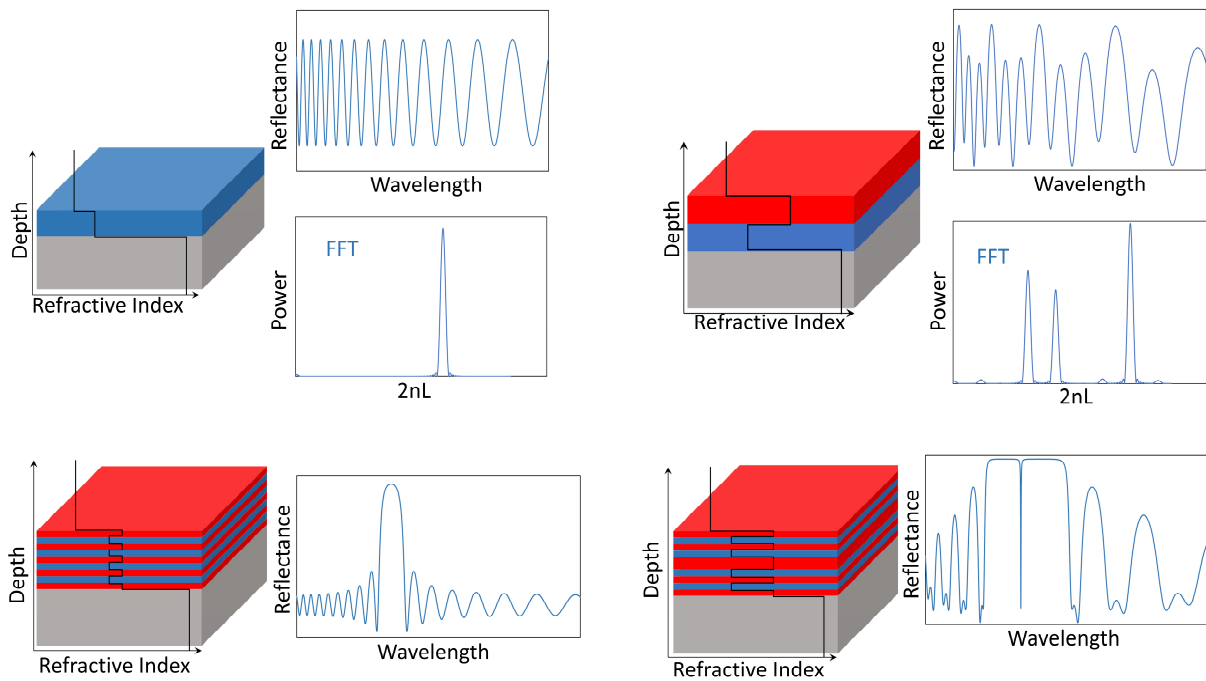
Figure 1.5. Common PSi structures utilized for optical biosensing applications and their associated optical reflectance spectra: (a) single-layer interferometer, (b) double-layer inteferometer, (c) Bragg stack (low index contrast), (d) microcavity. High and low refractive index layers are shown in red and blue, respectively.

1.3.4 PSi Optical Measurements

Optical properties of PSi films can be characterized through the reflectance spectra, measured using the experimental setup shown in Figure 1.6. Light from a quartz tungsten halogen broadband white light source is coupled into a bifurcated optical fiber and is focused onto the PSi biosensor on an optical stage with a microscope objective lens secured in a lens tube housing. The height of the lens relative to the PSi sample can be adjusted to achieve the desired spot size on the surface of the PSi film.
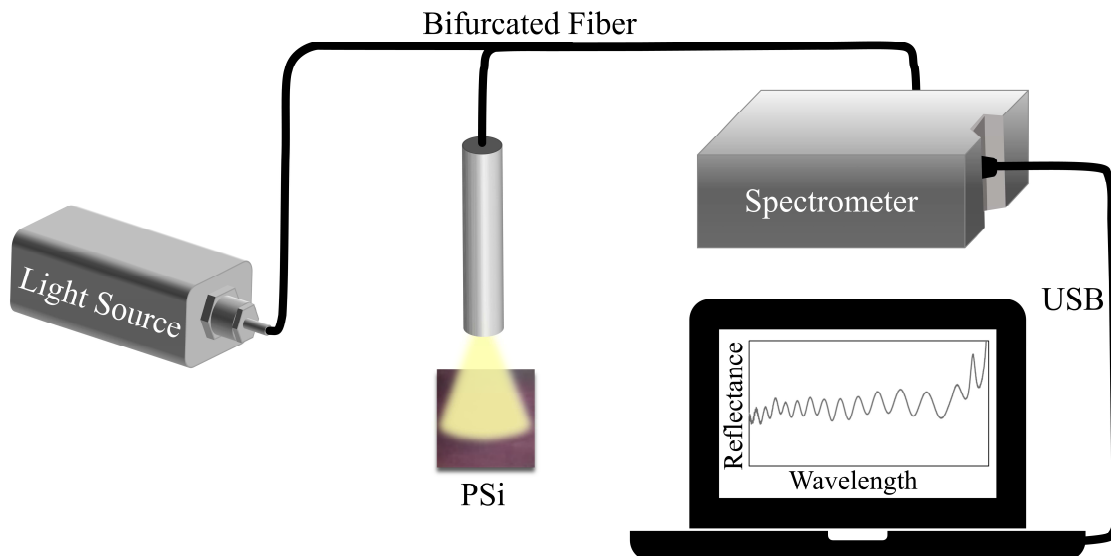
Figure 1.6. Experimental setup to measure the reflectance spectrum of a porous silicon thin film structure.

The reflected light is then collected by the same lens and coupled via the other arm of the bifurcated fiber into a USB CCD spectrometer, which splits the light into constituent wavelengths using a diffraction grating onto a CCD pixel array. Typical dynamic range is between 200 and 1100nm with a spectral resolution of 10 to 0.1nm. The spectrometer is connected to a PC running software to integrate, average, and record spectra for further processing.

1.3.5 PSi Biosensing Platform

The sensing mechanism of PSi relies on the infiltration, diffusion and adsorption of target molecules inside the pores upon analyte exposure. This process leads to an increase in effective refractive index of the PSi layer (or layers) since the refractive index of the biological material is higher than that of air (typically $n_{analyte} \approx 1.5$), causing a shift in the optical reflectance spectra to higher wavelengths, the magnitude of which can be used to quantify the number of adsorbed molecules in the pores. Conversely, removal of material or dissolution of the PSi matrix will cause

a decreased effective refractive index, shifting spectral features to lower wavelengths. For a single layer of PSi with sinusoidal spectral intensity variations in wavenumber space, an increase in effective refractive index increases the frequency of the fringes. It is common practice for single layer PSi biosensors to be used to measure biomolecule diffusion and adsorption profiles by tracking the peak in the FFT spectrum [77]. However, our work presenting an alternative signal processing technique, discussed in chapter 2, shows that wavelet processing can achieve better immunity to commonly encountered noise signatures, allowing lower detection limits [78]. For double layer PSi structures, the peaks in the FFT spectra corresponding to each of the two layers can be tracked independently, elucidating not only the number of molecules adsorbed in the structure as a whole but also identifying the layer in which they reside. This can mitigate biofouling and provide size selectivity of molecules, among other benefits [77]. For other photonic structures such as microcavities (Figure 1.5 (d)) or low-index-contrast Bragg stacks (Figure 1.5 (c)), peak detection methods can be used to sensitively quantify spectral shifts [79–81].

1.4 Key Biosensor Challenges

Despite the commercial success of many biosensor systems [82], such as glucose monitors, pregnancy tests, and other lateral flow assays, there remain a vast array of applications which are out of reach of current biosensor platforms and technologies, and for which the solution, if one exists, often requires highly sophisticated, costly, and complex instrumentation. Accordingly, the current gold standard mainstream technologies for detecting important biomolecules, providing an alternative to biosensors, include polymerase chain reaction (PCR) [21], enzyme-linked immunosorbent assay (ELISA) [22], and mass spectrometry [23]. These can achieve high

20

specificity, sensitivity, and often low detection limits and are widely used in laboratories and hospitals. However, these approaches generally require instrumentation that is prohibitively large, expensive, and complex to operate, often involving strict sample preparation procedures. This restricts their use for many applications, particularly in low-resource environments without trained personnel, where cost effectiveness, portability, and ease of use are of paramount importance. One example is light chain (AL) amyloidosis, a deadly disease which at an early stage leads to an imbalance in serum free light chains (SFLC). As it progresses, AL amyloidosis causes abnormal deposition and build-up of amyloid fibrils in the tissue and organs. This condition often remains undiagnosed during a patient's lifetime [83], due to the complex and costly gold standard laboratory testing approach using mass spectrometry, which precludes routine screening and early stage diagnosis.

To overcome these limitations and provide viable solutions to the most pressing problems across medical diagnostics, food safety, and environmental monitoring, several biosensor performance metrics [84] need significant improvement, alongside other considerations such as cost, ease of use, and form factor.

1.4.1 Detection Limit

The limit of detection (LOD) of a biosensor is the minimum concentration or number of molecules that can be reliably detected. A normal distribution of measurements can be built up both before and after biomolecule exposure, termed the blank and shifted distributions, respectively. The LOD is typically quantified as the concentration of the target molecule leading to a response such that the lower bound of the highest 5% of the blank distribution, which lies 1.65

standard deviations above the mean, coincides with the upper bound of the lowest 5% of the shifted distribution, which lies 1.65 below the mean [85]. Equivalently stated,

$$\mu_{\text{shift}} - \mu_{\text{blank}} = 1.65\sigma_{\text{blank}} + 1.65\sigma_{\text{shift}} \approx 3.3\sigma_{\text{blank}} \tag{2.2}$$

where μ_{blank} and μ_{shift} are the mean of the blank and shifted distributions, respectively, and σ_{blank} and σ_{shift} are the standard deviations of the blank and shifted distributions, respectively. The standard deviations are typically assumed to be approximately equal. It is important to note that μ_{blank}, the average sensor response in the absence of the target biomolecule, is in general not zero; making the assumption that $\mu_{\text{blank}} = 0$ can lead to inflated LOD estimates and ignores adsorption of non-target molecules, corrosion, and other cumulative changes in the sensor response. However, we note that this assumption is falsely applied across the literature, which in addition to the practice of collecting only experimental data at relatively high concentrations and extrapolating to much lower concentrations, can form the basis of unrealistic claims of wildly overestimated detection limits.

For many applications, the best detection limits achieved by state-of-the-art biosensors are not sufficient for clinical, physiological, or environmental relevancy, lagging behind the gold standard laboratory analytical instrumentation [86–88]. Additionally, the lowest LODs achieved in the literature using PSi biosensors are typically higher than those based on other biosensing systems [63,67,68]. To improve detection limits, aside from signal processing techniques discussed in chapter 2, other sensitivity enhancing methods include incorporating secondary-detection capture-agent probes [62] or quantum dots [89,90].

1.4.2 Stability and Robustness

It is important for a biosensor's response to be stable over time, without deterioration due to light exposure or varying temperature and humidity, since environmental instability and drift lead to inaccurate test results and restrict shelf-life. The weak link, in terms of biosensor stability and robustness, is usually the capture agent [91–93], which typically denature or degrade in extreme climates such as those experienced in low-resource developing nations, where there is often the greatest need for cheap and reliable POC medical diagnostics suitable for use outside of controlled environments. Additionally, capture agents often require low temperatures to be maintained for long-term storage and transport, which is not always feasible.

1.4.3 Response Time

The response time of a biosensor is the time taken to return the test result, usually when the response has reached equilibrium. Response time of a sensor is an important metric, particularly in safety critical applications. For example, there is a great need for biosensors with fast response times to enable rapid tests for medical diagnostics, which can increase healthcare access and markedly improves patient outcomes [94,95]. The challenge is that many sensing modalities have inherently slow response times, often due to poor mass transport limited by diffusion as well as the timescales of adsorption and desorption [96].

1.4.4 Specificity

Specificity is defined as the ability of a sensor to provide an isolated response to a target species, irrespective of the presence of other molecules and contaminants, to avoid false positive test results. Traditionally, capture agents, which include antibodies, enzymes, nucleic acids, aptamers, and molecularly imprinted polymers, provide specificity through strong and selective

23

affinity to the target molecule. However, fouling and non-specific binding, both of which reduce specificity, pose a pervasive problem, subject to considerable research effort [97–99]. Furthermore, capture agents are often expensive, can be complex to design and manufacture, and have significant associated development time. It would therefore be advantageous to eliminate the need for a capture agent and provide the high selectivity and strong affinity of capture agents by another means. To address these issues, sensor arrays have been developed to mimic the mammalian olfactory system, which is thought to be able to detect trillions of different volatile odorant molecules by using hundreds of cross-reactive olfactory receptor epithelial cells with varying affinity for a wide range of molecules and pattern recognition in the brain [100–102]. In synthetic "electronic noses," [36,39,103] the collection of olfactory receptors are replaced with array-based sensors relying on one of the following mechanisms: optical sensors comprising fluorometric or colorimetric dyes [104], electrochemical sensors such as amperometric [105] and metal oxide semiconductor sensors [106], and microelectromechanical mass sensors such as piezoelectric [107] and surface acoustic wave (SAW) sensors [108]. Machine learning is then used to classify and quantify different molecules using pattern recognition and prediction algorithms.

1.5 Overview of Dissertation

Biosensors are playing an increasingly important role in keeping people around the world healthy and safe. The focus of this dissertation is on strategies which employ machine learning, statistics and signal processing to enhance biosensor performance, enabling applications which are out of reach with current biosensor technologies. The first challenge to be addressed is reducing detection limits (Chapter 2) by applying wavelet denoising to PSi reflectance spectra, filtering

24

noise signatures and providing a more sensitive measure of spectral shifts for thin film optical sensors. This approach brings clinically relevancy within reach for many medical diagnostic applications. The second advance is the development of a capture-agent-free sensor (Chapter 3), by creating a biosensing system using PSi arrays and using machine learning to identify biomolecules, increasing robustness and reducing cost and complexity. This novel sensor design could ensure that populations of low resource geographic regions which experience extreme climates can also reap the benefits of effective biosensors. The third challenge to be addressed is that of reducing sensor response time (Chapter 4), which enable quicker medical diagnostics allowing earlier treatment, identification of toxic molecules in food or the environment more rapidly to minimize their harmful impact, and open up the possibility for many biosensing platforms to reformulated as point-of-care devices. Finally, Chapter 5 summarizes the key outcomes of this dissertation and discusses the broader impact and implications of the results within the fields of biosensing, machine learning, applied statistics, and signal processing.

CHAPTER 2

Reducing Detection Limits using Signal Processing

Parts of this chapter are adapted from "Morlet Wavelet Filtering and Phase Analysis to Reduce the Limit of Detection for Thin Film Optical Biosensors" published in ACS Sensors and reproduced with permission from publisher, and "Reducing detection limits of porous silicon thin film optical sensors using signal processing" published in SPIE Proceedings and reproduced with permission from publisher.

S. J. Ward, R. Layouni, S. Arshavsky-Graham, E. Segal, and S. M. Weiss, "Morlet Wavelet Filtering and Phase Analysis to Reduce the Limit of Detection for Thin Film Optical Biosensors," *ACS Sensors,* 6(8), 2967–2978 (2021).

S. J. Ward, and S. M. Weiss, "Reducing detection limits of porous silicon thin film optical sensors using signal processing," *Proc. SPIE, 11662*(116620J), 1–9 (2021).

2.1 Introduction

Detecting low levels of an analyte is crucial for a wide variety of sensing applications, including medical diagnostics in which early detection of low concentrations of disease biomarkers enables preventative measures and treatments with exponentially higher rates of positive patient outcomes [109], and environmental monitoring in which detection of toxic substances harmful to humans at ultra-low levels can save lives [110]. Of the many ways to improve limit of detection (LOD), arguably the cheapest and easiest strategy is signal processing, which can enhance

detection limits by removing various noise signatures. Signal processing for noise reduction is applicable to all systems, from costly, high resolution and highly accurate laboratory instruments to compact, simple and cheap point-of-care devices.

Signal processing has been used in a wide variety of biosensing platforms to enhance noise immunity, achieve lower detection limits, and provide deeper insight into the physical properties of the sensor and the sensing mechanism. For surface plasmon resonance sensors, one of the most prevalent optical biosensing platforms, techniques such as polynomial fitting [111], centroid detection [79] and tracking [80], complemented by dynamic baseline algorithms [112], linear data analysis [81], locally weighted parametric regression [113], and the radon transform technique [114] have been used for higher resolution resonance detection and reduced noise susceptibility. The performance of quartz crystal microbalance sensors, another effective and widely used biosensing platform, has also benefitted from signal processing methods, such as the fractional Fourier transform [115], heterodyning [116], and moving average and Savitzky-Golay filtering [117]. Additionally, frequency locking along with nonlinear filtering has been used to lower the noise floor of microtoroid optical biosensors, enabling single molecule detection [118], and a range of signal processing methods have been applied to measure spectral shifts of guided mode resonant filter biosensors such as cross correlation and maximum likelihood techniques [119]. The most appropriate signal processing approach to utilize depends on the application and the characteristics of the measured signal.

For many applications, including biosensing, there is particular interest in being able to determine small changes between two measured thin film optical spectra: several different signal processing approaches can be applied to help interpret thin film optical spectral shifts. In this

chapter, we introduce a signal processing approach based on Morlet wavelet convolution and phase analysis that can dramatically lower the detection limit of thin film biosensors, which are among the simplest optical biosensor platforms. We utilize porous silicon (PSi) thin film biosensors for our demonstration of the benefits of this signal processing approach. One common signal processing approach to measure changes in the Fabry-Pérot interference fringes due to adsorbed biomolecules is the reflective interferometric Fourier transform spectroscopy (RIFTS) method [77], which involves determining the dominant frequency of these fringes by carrying out a Fast Fourier Transform (FFT) on the reflectance spectra, and then identifying the peak interference fringe frequency. This method gives important physical information about the optical properties of the film, but its accuracy is deteriorated by noise. More recently, promising improvements in LOD of PSi thin films have been reported [120,121] using the Interferogram Average over Wavelength (IAW) technique. However, the robustness of the IAW method is an issue when there are offset and amplitude variations modulating the Fabry-Pérot interference fringes. These noise sources, found in most data sets, originate from the measurement system (e.g., light source, spectrometer, imperfect calibration of the system), as well as scattering of light by molecules adsorbed to the surfaces of the PSi thin film and to the surfaces of microfluidic channels when they are utilized [122]. Moreover, noise contributions tend to be more pronounced in sensing assays carried out in complex media.

Since the Fabry-Pérot fringes characteristic of thin film reflectance spectra are approximately sinusoidal, they are well suited to band pass filtering, designed to remove undesired low frequency variations as well as white noise at all frequencies above and below the pass band, which improves robustness and enables lower detection limits. In this chapter, we show that

application of complex Morlet wavelet convolution, which has previously been used to filter electrical signals generated from electrodes monitoring brain or heart activity [123], and seismic activity [124], is a highly effective approach to reduce noise signatures in optical spectra of thin films such as PSi single layer biosensors. We coin the name, Morlet wavelet phase method, to describe our approach that utilizes both a complex wavelet and extracted phase information. The Morlet wavelet phase technique enables a reduction of the LOD by almost an order of magnitude relative to RIFTS and IAW, and makes thin film sensors, such as those based on PSi, potentially viable options for many clinical applications. We note that the Morlet wavelet phase signal processing technique does not negatively impact manufacturability, cost, complexity, or response time, and can be applied alongside other sensitivity enhancing and noise reduction techniques. We additionally note that although the RIFTS, IAW, and Morlet wavelet phase methods are applied only to single layer thin films in this work, these signal processing techniques could also be applied to analyze any signal containing a finite number of approximately sinusoidal frequency components. The noise immunity, sensitivity and linearity of Morlet wavelet phase method is benchmarked against several other signal processing methods by applying the different techniques to a large set of simulated porous silicon thin film optical spectra that contain various types of noise signatures.

2.1.1 RIFTs and IAW Methods

One approach to characterizing the reflectance spectra of thin films is to measure optical thickness by monitoring the frequency of the Fabry-Pérot fringes in wavenumber-space. We note that it is essential to plot the reflectance of the film as a function of wavenumber so that the Fabry-Pérot fringes are equally spaced across the spectrum. Changes in optical thickness of thin films are

29

characterized by changes in the frequency of these Fabry-Pérot fringes. The RIFTS method aims to identify the dominant frequency of the Fabry-Pérot fringes, corresponding to the optical thickness, from the FFT of the reflectance spectra. The RIFTS technique consists of the following four operations:

1   Plot the reflectance spectra against wavenumber using cubic spline interpolation to generate equally spaced points (Figure 2.1 (a) (i)).

2   Apply a Hann window to the chosen spectral measurement range to enforce periodicity and consequently reduce spectral leakage (Figure 2.1 (a) (ii)).

3   Increase the length of the data by zero padding to realize the desired resolution of 2nL values when the FFT is applied (Figure 2.1 (a) (ii)). Note that the highest efficiency is achieved when the number of points is a power of two.

4   Carry out an FFT and identify the frequency of the dominant peak (Figure 2.1 (a) (iii)).

Changes in optical thickness caused by biomolecule attachment can therefore be determined in a straightforward manner, by monitoring the change in the peak frequency result from the RIFTs method applied to spectra measured before and after exposure of the thin film to biomolecules.

Since a change in Fabry-Pérot fringe frequency causes the Fabry Pérot fringes to shift (by an amount proportional to wavenumber), another strategy to measure biomolecule attachment is to calculate the difference between spectra before and after biomolecule exposure. The IAW method uses this approach, and is implemented as follows:

30

1   Find the difference between a 'reference' reflectance spectrum before exposure of the target biomolecule, and an 'analyte' spectrum after biomolecule exposure, termed the 'interferogram' (Figure 2.1 (b) (i)).

2   Zero the interferogram by subtracting the mean from each value (Figure 2.1 (b) (ii)).

3   Integrate the absolute value of each point in the interferogram over the chosen spectral measurement range (Figure 2.1 (b) (iii)).

It should be noted that the magnitude of the IAW signal change is strongly dependent on the changing amplitude of the Fabry Pérot fringes at each given wavenumber in the reference and analyte spectra, which in turn makes the technique more susceptible to noise contributions that affect the measured amplitude of the spectra. The RIFTS technique, on the other hand, is not strongly affected by the relative amplitudes of the spectra.

2.1.2   Alternate Candidate Signal Processing Approaches

Directional IAW

Directionality can be introduced to the IAW method by first summing sections of the difference spectrum, or interferogram, corresponding to regions between adjacent peaks and valleys in the reference spectrum, which can be done with the assistance of a polynomial fit [125]. If the analyte spectrum is red-shifted relative to the reference spectrum, then this summation will lead to a positive value. Next, separately sum sections of the interferogram corresponding to regions between adjacent valleys and peaks in the reference spectrum. If the analyte spectrum is red-shifted relative to the reference spectrum, then this second summation will lead to a negative value. Finally, subtract the latter summation from the former summation and the sign of the result indicates the direction of the spectral shift between the analyte and reference spectra (i.e., positive

31

sign = red-shift). To our knowledge, there are no documented prior implementations of such a directional IAW method.

Least Squares Fitting Fabry-Perot Fringes

One method of extracting physical parameters of a sensing system is to calculate an analytical function of the theoretical response, and then optimize the unknown parameters to minimize mean squared error between the analytical prediction and the experimental data. This approach has been applied to many sensing platforms including quartz crystal microbalance [117]. In a similar way, the frequency of thin film interference fringes can be measured by performing least squares fitting of the Fabry-Perot fringe functional form, optimizing parameters of amplitude, phase, and frequency. Refractive index changes cause a change in Fresnel amplitude coefficients, and consequently the amplitude of the Fabry-Perot fringes. Hence, the amplitude could be combined with frequency to enhance the signal, as it does for the IAW method, but this approach would also suffer from false positive responses when amplitude variations are part of the noise contributions of the measurement system. We note that in the case of PSi thin films, refractive index changes not only change the amplitude, but also modify the frequency of the Fabry-Perot fringes.

Cross Correlation

Cross-correlation is a signal processing technique that is widely used in the context of sensing, including optical sensors based on optical fibers [126,127]. The cross-correlation is a measure of similarity of signals and has good noise immunity. It therefore provides good discrimination between noise variations in the absence of a target molecule and a change in the signal caused by the presence of the target molecule, which decreases the signal similarity and

32

therefore the cross-correlation. While cross-correlation has not been applied to thin film optical sensors, to our knowledge, summing the cross-correlation of a reference spectra and analyte spectra is a promising way of measuring spectral shifts of Fabry-Perot fringes. A combination of autocorrelation, the cross-correlation of a signal with itself, and peak detection was also explored to measure frequency, but was found to be less effective [125].

Multiple Signal Classification (MUSIC)

The MUSIC algorithm was developed to estimate parameters of noisy sinusoids by performing covariance matrix eigenvalue decomposition. It is used for direction finding and resolving multiple sources, as well as for spectral parameter estimation [128], but to our knowledge has not been applied specifically to thin film optical spectra. The advantages of this approach include super-resolution frequency estimation not limited to discrete frequency bins, and the ability to specify the number of sinusoidal constituents resulting in more efficient noise rejection.

Finite Impulse Response (FIR) Filtering

FIR is a category of digital filter which is ubiquitous in the domain of signal processing and is commonly used in sensing applications, due to its tunability by using least squares linear phase filter design. FIR filters have been successfully applied to Fabry-Perot fringes of optical fiber interferometric sensors [129], and consequently show promise for the similar problem of filtering thin film optical spectra. For this purpose, the superior performance and stability of FIR filters compared to Infinite Impulse Response (IIR) filters are worth the extra computational complexity [130].

2.1.3   Complex Morlet Wavelet Convolution: Morlet wavelet phase method

Because the LOD for thin film sensors is limited by both high frequency white noise and low frequency noise signatures in the reflectance spectrum, band pass filtering is a promising signal processing approach to apply. In particular, complex Morlet wavelet convolution [131] is well suited for filtering the spectra of thin film sensors as a means of maximally removing noise while retaining the desired optical signal. A complex Morlet wavelet is a complex exponential with a Gaussian envelope, which is localized in time and results in a Gaussian line shape in frequency space. As a result, a Morlet wavelet, unlike alternative band-pass filtering approaches, is able to provide an optimal tradeoff between temporal and spectral precision [132], or in the case of optical thin film biosensors, resolution in both wavenumber and fringe frequency. In contrast, the Fourier transform implicitly assumes signal stationarity which is violated for thin film fringes due to dispersion, leading to a variation in the frequency of fringes as a function of wavenumber. Consequently, the dominant frequency peak in the FFT spectrum of optical thin film sensors is smeared, reducing the resolution, and diminishing the minimum frequency shifts of the fringes that can be reliably measured and results in sub-optimal detection limits. Through careful choice of the width of the wavelet, the optimal tradeoff between resolution in wavenumber and fringe frequency can be achieved, maximizing the filtering of noise sources superimposed on the thin film fringes in tandem with the best preservation of the thin film fringes with non-stationary frequency. The convolution of a Morlet wavelet with a signal is equivalent to multiplication in frequency space, which can act as a strict band pass filter. Since the wavelet is complex, the filtered result is a complex signal from which phase and amplitude can be extracted. The first stage of the

Morlet wavelet phase method, complex Morlet wavelet band pass filtering, is summarized by the following steps:

1 Plot reflectance spectra against wavenumber, using linear interpolation so points are equally spaced (Figure 2.1 (c) (i)).

2 Zero pad the data to obtain the desired resolution in frequency space.

3 Carry out an FFT and identify the center frequency and full width at half maximum (FWHM) of the dominant peak (Figure 2.1 (c) (ii)).

4 Use the center frequency and FWHM of the dominant peak to define a complex Morlet wavelet, shown in the green trace in Figure 2.1 (c) (i) in wavenumber space. An FFT of the complex Morlet wavelet is shown in the green trace in Figure 2.1 (c) (ii) and reveals the band pass filtering ability of the Morlet wavelet. The spacing between wavenumber values of the wavelet should be the same as for the interpolated reflectance spectra.

5 Convolve the wavelet with the reflectance data (Figure 2.1 (c) (i)) to obtain the complex filtered output, the real part is shown in Figure 2.1 (c) (iii).

6 The phase and amplitude can then be extracted from the real and imaginary components of the filtered output over the spectral measurement range; the extracted amplitude is shown in Figure 2.1 (c) (iii) alongside the real part of the filtered output. The amplitude can subsequently be used to normalize the Fabry-Pérot fringes (Figure 2.1 (c) (iii), (iv)).

By carrying out a FFT of the uniform amplitude normalized fringes using a Hann window function, it becomes clear in frequency space that the high and low frequency noise components have been removed from the filtered data (Figure 2.1 (c) (v)). For the Morlet wavelet phase method, only the phase is used, as this was found to be the most accurate way of transducing frequency

35

shifts; however, for some applications, it may be useful to obtain normalized fringes, for example as a preprocessing step to remove noise signatures before carrying out the IAW or RIFTS methods. The first three steps of complex Morlet wavelet band pass filtering are calculated in a similar way to the RIFTS method, with the exception that no Hann window is applied to avoid broadening the dominant frequency peak (i.e., to give a more accurate FWHM of the frequency peak that is used in defining the wavelet), at the expense of having greater spectral leakage and extra lobes introduced. Additionally, through empirical studies, we found that linear interpolation gave the best performance for Morlet wavelet filtering, in contrast with the RIFTS method which performs best with cubic spline interpolation.

The Morlet wavelet phase method [133] uses complex Morlet wavelet filtering to measure changes in optical thickness as follows:

1 Apply complex Morlet wavelet band pass filtering, as described previously, to a 'reference' reflectance spectrum before exposure of the target biomolecules and to an 'analyte' spectrum after biomolecule exposure (Figure 2.1 (d) (i)). The real part of the filtered output is shown in Figure 2.1 (d) (ii).

2 After extracting the phase from the complex results of filtering the reference and analyte spectra (step 6 in Morlet wavelet band pass filtering), unwrap the phase by adding 2π every time it goes through another complete cycle to give a continuous linearly increasing phase, rather than being confined to the interval $[0,2\pi]$, for both the reference and analyte spectra (Figure 2.1 (d) (ii)).

3 Correct for the phase of reference and analyte spectra starting in different cycles. For example, if the initial phase of the reference spectra at the lowest wavenumber in the measurement

36

window has a phase just below 2π, biomolecule adsorption could cause the initial phase to shift into the next cycle with a phase just above 0 for the analyte spectra, which causes an additional 2π difference between the reference and analyte phase at every value of wavenumber, unrelated to biomolecule adsorption. To correct for this difference in the initial phase of the reference and analyte spectra, a coarse value of initial phase is estimated using the FFT dominant fringe frequency, alongside the accurate Morlet Wavelet extracted phase, to determine when the phase has entered a different cycle. The coarse estimate can be defined as $2nL/\lambda_{end}$, where 2nL is the optical thickness given by the RIFTS method, and λ_{end} is the higher wavelength bound for the spectral measurement range. The fine estimate is the extracted phase from the Morlet wavelet filtered signal at the lowest value of wavenumber, $\frac{1}{\lambda_{end}}$. The difference between coarse and fine estimates for the reference and analyte spectra are compared; when they differ by a multiple of 2π, this is corrected.

4 Average the difference between the unwrapped linear phase for the reference and target spectra, which yields the Morlet wavelet phase result (Figure 2.1 (d) (iii)).

5 Optionally, a scaling factor and offset can be applied to convert the Morlet wavelet phase result to units of effective optical thickness changes rather than arbitrary units. The scaling factor is calculated by generating many spectra with incrementally increasing effective refractive indices over a large range, carrying out both RIFTS and Morlet wavelet phase analysis, and finding a linear fit to convert between them.

To optimize the performance of all signal processing methods, the spectral measurement range to analyze should be chosen to include as much of the measured spectra as possible while

rejecting the extremes of the spectra with poor signal to noise ratio (S/N). Hence, the most appropriate spectral range for the signal processing methods is dependent on the limitations of the optical components and spectrometer utilized in the measurements. In this work, a spectral measurement range of 500-800 nm was used unless otherwise noted in order to facilitate comparison between techniques and previous studies.
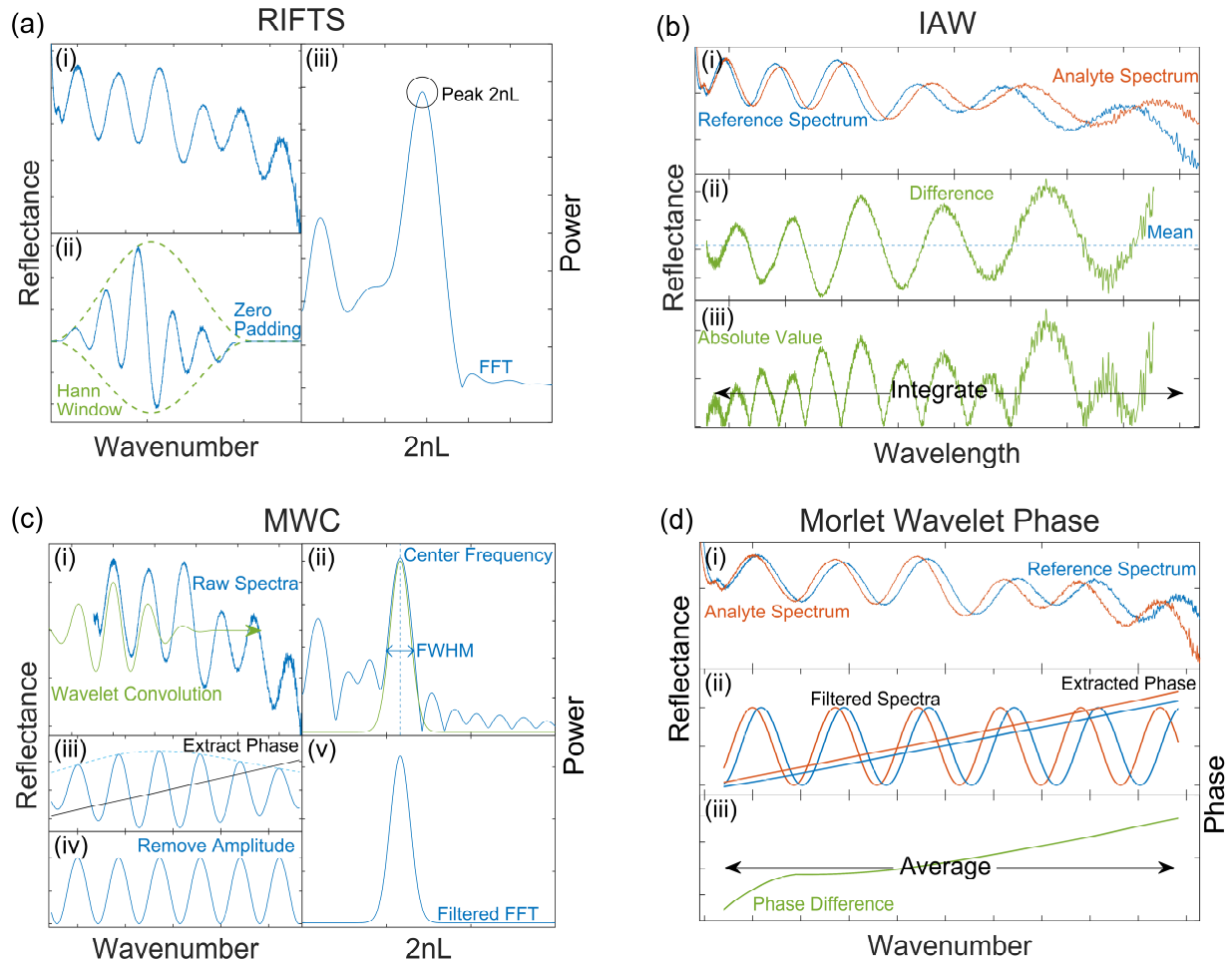
Figure 2.1. Illustration of signal processing techniques: (a) RIFTS, (b) IAW, (c) complex Morlet wavelet convolution, and (d) Morlet wavelet phase, applied to experimentally measured reflectance spectra of a single layer PSi thin film. The steps for each method are described in detail in section 2.1.3.

2.1.4 Computational Generation of Spectra

To provide a comprehensive comparison between different signal processing techniques, reflectance spectra of a single layer PSi thin film were simulated using the transfer matrix method [76]. White Gaussian noise was added to the simulated spectra to better mimic measured data. The simulated thin film was defined as a 2.4 µm thick layer with effective refractive index of 1.2, which are realistic parameters comparable with experimental data sets. To rigorously test

39

each signal processing method and mirror noise encountered in real experimental spectra as closely as possible while keeping the analysis simple and generalizable, three different noise contributions were considered: (1) a simple shift of the Fabry-Pérot fringes due to a refractive index change with added white Gaussian noise, (2) a refractive index change with white Gaussian noise and a unitary wavelength dependent linear offset applied to the Fabry-Pérot fringes, and (3) a refractive index change with white Gaussian noise and a unitary wavelength-dependent linear amplitude variation applied to the Fabry-Pérot fringes. These noise contributions can be expressed as

$$f(\lambda) = R(\lambda)\left(1 + a\frac{(\lambda - \lambda_{start})}{(\lambda_{end} - \lambda_{start})}\right) + o\frac{(\lambda - \lambda_{start})}{(\lambda_{end} - \lambda_{start})} + \sigma_n \qquad (2.2)$$

where $R(\lambda)$ is the wavelength dependent reflectance generated using the transfer matrix method, a is the amplitude variation term, o is the offset variation term, σ_n is the white Gaussian noise term, λ_{end} and λ_{start} are the upper and lower bounds of the wavelength measurement range, respectively, and $f(\lambda)$ is the resulting noisy spectra. The S/N when comparing the signal to the white Gaussian noise was 27.7 dB. The S/N decreased to 7.9 dB and 7.7 dB when the linear offset was superimposed or the linear amplitude variation was introduced, respectively. A linearly varying offset and amplitude are simple modifications to fringes with a relatively complex spectral composition, testing the signal processing methods immunity to a wide variety of noise signatures seen experimentally.

When introducing the offset or amplitude gradient to the reflectance spectra, the resulting change in response was isolated by calculating the blank distribution with and without the gradient

at a constant refractive index. The effect on the response of each signal processing technique when applying a gradient to the offset or amplitude, Δg, was added to the blank-distribution standard deviation σ_{blank}, resulting in a LOD of $3.3(\sigma_{blank} + \Delta g)$. Including this effect as part of the standard deviation of the blank distribution enables modeling a distribution of offset or amplitude gradients that occur in tandem with any refractive index change and white noise-induced interference fringe shifts. The mean and standard deviation of the blank and shifted distributions, as well as the blank distributions incorporating an offset or amplitude gradient, were each calculated from 1000 separately generated spectra with a random white noise contribution.

MATLAB (R2019b) was used to generate the noisy spectra. In addition, the Signal Processing Toolbox in MATLAB was utilized to implement each of the signal processing algorithms investigated in this work. The algorithmic code was run on both simulated data and experimental data.

2.2 Experimental Methods

Signal processing approaches were applied to the measured data from two experimental systems: (1) non-specific bovine serum albumin (BSA) assay in buffer to investigate the LOD, and (2) anterior gradient 2 (AGR2) protein biosensor to investigate (i) the robustness of the signal processing approaches in buffered and complex media and (ii) selectivity in comparing target and non-target proteins. Non-specific adsorption of BSA is commonly utilized to demonstrate the proof-of-concept performance of biosensing platforms, and AGR2 is a biomarker for many types of cancer. These assays were executed in different labs (Vanderbilt University and Technion Israel Institute of Technology), with different experimental setups, different experimental procedures,

41

and different materials, to demonstrate the broad applicability of the Morlet wavelet phase technique when encountering different noise fingerprints.

2.2.1 BSA Assay (carried out at Vanderbilt)

Materials

Chemicals were all analytical grade, used without further purification. De-ionized (DI) water with resistivity 15 MΩ cm, from a Millipore Elix water purification system was used for all solutions. Single side polished, boron doped silicon wafers (⟨100⟩, 0.01−0.02 Ω cm, 500−550 μm) were purchased from Pure Wafer. Ethanol and BSA were purchased from Thermo Fisher Scientific, and pH 4 reference standard buffer, used for BSA solutions, was obtained from Sigma-Aldrich. Aqueous hydrofluoric acid (HF) (48-51%) was purchased from Acros Organics. Solution pH was measured using a Mettler Toledo Seven Easy pH-meter.

Fabrication of Single Layer PSi

Single layer PSi thin films were fabricated by anodic etching of p-type silicon wafers with HF, described in detail elsewhere [7,134]. A solution of 15% (v/v) HF in ethanol was used, and the wafer was etched using an Advanced Micromachining Tools (AMMT) MPSB porous silicon wafer etching system. First, a sacrificial layer was etched with a current density of 70 mA cm^2 for 100 s and then dissolved in 1 M KOH solution. Next, the sample was thoroughly cleaned with DI water and ethanol and then etched again at 70 mA cm^{-2} for a further 50 s. Finally, the wafer was oxidized in ambient air at 800°C for 10 min using a Lindberg/Blue M box furnace to passivate the silicon by forming an insulating layer of SiO_2. The PSi films were 1.77 μm thick, with a porosity and average pore diameter of 67% and 49 nm, respectively, as determined by scanning electron microscopy (SEM) image analysis and effective optical thickness measurements.

42

Optical Reflectance Measurements

Broadband white light from a Newport Oriel 6000 Q light source was fiber coupled to an Ocean Optics USB4000 CCD spectrometer, averaging and recording 100 spectra per second using the Ocean Optics Spectra Suite software. The spot size was focused to a 5 mm diameter on the surface of the PSi films, achieved using an Olympus SPlan 10x microscope objective lens.

Experimental Procedure

PSi samples 5 mm × 5 mm were cleaved from the etched wafer, washed with water and ethanol, and dried under nitrogen. Reflectance spectra were then measured to obtain a baseline effective optical thickness and an IAW and Morlet wavelet phase reference spectrum. A further 100 measurements were taken to quantify the noise floor for each method: the blank distribution standard deviation σ_{blank}. Different concentrations of BSA were prepared in 80% pH 4 reference standard buffer, 20% DI water solutions v/v (3 pM, 300 pM, 30 nM, 300 nM, 3 µM, 30 µM, 300 µM) and were drop cast on the samples and left to incubate for 2 hours. The samples were subsequently washed in a water bath for 10 s, which removes unbound and potentially a small number of weakly bound molecules in the pores and from the surface. The change in reflectance after this wash step showed almost no dependence on wash duration. After washing, the PSi was dried under nitrogen and measured again. There were 16 repeats performed at each concentration. A number of adsorption isotherms were fit to the data using a least squares fit weighted by the variance due to the heteroscedasticity of the data, and the chi-squared goodness of fit was calculated to quantify quality of model fit and determine the most appropriate adsorption model. The predicted LOD was then calculated, given by the concentration where the best fit line intersects $3.3\sigma_{blank} + I$, where I is the intercept of the adsorption model line of best fit.

2.2.2 AGR2 Biosensor (carried out at Technion)

Materials

Chemicals were all analytical grade, used without further purification. Double distilled water (ddH$_2$O) with resistivity 18.2 MΩ·cm from a Milli-Q water purification system was used for all solutions. Heavily p-doped silicon wafers (⟨100⟩, 0.90–0.95 mΩ cm) were purchased from Sil'tronix Silicon Technologies. Aqueous 48% HF, and ethanol were purchased from Bio-Lab ltd. (3-Aminopropyl)triethoxysilane (APTES), diisopropylethylamine (DIEA), succinic anhydride, N-(3-Dimethylaminopropyl)-N′-ethylcarbodiimide hydrochloride (EDC), N-Hydroxysuccinimide (NHS), acetonitrile and all buffer salts were supplied by Merck. Anti-AGR2 aptamer sequence33, 5'-TCT-CGG-ACG-CGT-GTG-GTC-GGG-TGG-GAG-TTG-TGG-GGG-GGG-GTG-GGA-GGG-TT-3', was purchased with a 5'-amino modification from Integrated DNA Technologies. AGR2 protein was purchased from MyBio-Source Inc. Rabbit Immunoglobulin G (IgG) was purchased from Jackson ImmunoResearch Labs Inc. Human blood plasma from healthy subjects was purchased from Merck. Selection buffer (SB) was composed of 137 mM NaCl, 20 mM KCl, 10 mM Na$_2$HPO$_4$ and 2mM KH$_2$PO$_4$ (pH 7.4).

Fabrication of Single Layer PSi

Single layer PSi thin films were fabricated by anodic etching of p-type silicon wafers with HF. First, a sacrificial layer was etched with a current density of 300 mA cm^{-2} for 30 s, using 3:1 (v/v) aqueous HF to ethanol solution, and then dissolved in 0.1 M NaOH solution, to remove surface impurities and oxides. Another layer is formed using identical conditions to the sacrificial layer, and the resulting PSi films were thermally oxidized at 800°C for 1 hour in a Thermo Scientific, Lindberg/Blue M Split-Hinge tube furnace. The PSi film thickness and range of pore

sizes were measured with a Carl Zeiss Ultra Plus high-resolution SEM at an accelerating voltage of 1 keV, and were found to be ~4.9 μm and 40-60 nm, respectively, and the average porosity was determined to be 74% using the spectroscopic liquid infiltration method (SLIM) [135].

Surface Chemistry Preparation

Amino-terminated aptamers, consisting of the anti-AGR2 sequence, were attached to the surface of the PSi films by carbodiimide coupling chemistry and amino silanization, as detailed elsewhere [136,137]. Briefly, the oxidized PSi films were amino-silanized in a solution of 1% APTES and 1% DIEA in ddH$_2$O (v/v) for 1 h and annealed at 100°C for 15 min. Subsequently, surface carboxylation was carried out in a solution of 10 mg mL^{-1} succinic anhydride and 2% (v/v) DIEA in acetonitrile for 3 h, followed by surface activation with 10 mg mL^{-1} EDC and 5 mg mL^{-1} NHS in 0.5 M MES buffer (pH 6.1) for 1 h. The activated surface was then reacted with the 50 μM amino-terminated aptamers for 1 h, followed by blocking with Tris buffer (50 mM Tris base, pH 7.4).

Optical Reflectance Measurements

For the biosensing experiments, the anti-AGR2 aptasensor was mounted in a custom-made Plexiglas cell, detailed elsewhere [138]. Light from a tungsten light source was fiber-coupled to an Ocean Optics USB4000 CCD spectrometer. A spot size of approximately 1mm^2 on the surface of the PSi was measured, focused using an objective lens.

Experimental Procedure

All experiments were performed without flow, in a static mode. Firstly, a baseline was established by incubating the aptasensor in SB. Next, an AGR2 protein solution either in SB or in

50% blood plasma in SB was injected into the cell and incubated on top of the sample for one hour. It should be noted that the blood plasma was diluted 1:1 in SB to ensure aptamer's proper folding and functionality in the complex media. Finally, the sample was washed with SB with a volume of ~10 mL until equilibrium was reached and all unbound molecules were removed.

2.3   Results and Discussion

2.3.1   Simulation Results Comparing LOD of Candidate Signal Processing Techniques

The minimum detectable refractive index change of a thin film was calculated by applying different signal processing techniques to reflectance spectra simulated using the transfer matrix method with additive white Gaussian noise. In order to systematically evaluate the robustness of the signal processing techniques to noise contributions often arising during experimental measurements, the LOD analysis was carried out with (1) no added systematic noise contributions, (2) a linearly varying signal offset, and (3) a linearly varying amplitude increase. Figure 2.2 shows the calculated LOD in each of these cases, given in terms of the minimum resolvable (i.e., 3.3σ) refractive index unit (RIU) change of analyte solution exposed to the PSi thin film, after application of the signal processing techniques to the simulated spectra, sorted in approximately descending order. In all cases, the lowest LOD was found when only Gaussian white noise was present. RIFTS, Morlet wavelet filtered IAW, and the Morlet wavelet phase method all demonstrated relatively good noise immunity to linearly varying amplitude changes. FIR filtered IAW and the Morlet wavelet phase method demonstrated relatively good noise immunity to linearly varying offset changes. Overall, the Morlet wavelet phase method was found to be most effective regardless of the type of noise present.

46

(a)

	Constant Offset and Amplitude	Linearly Varying Offset	Linearly Varying Amplitude
MUSIC	6.5×10^{-4}	1.8×10^{-2}	1.0×10^{-1}
Cross-Correlation	3.8×10^{-4}	5.5×10^{-2}	6.8×10^{-2}
RIFTS	8.3×10^{-4}	9.4×10^{-3}	9.2×10^{-4}
IAW	4.4×10^{-4}	2.3×10^{-2}	2.0×10^{-2}
Fabry-Perot Fringe Fit	5.6×10^{-4}	6.2×10^{-2}	1.2×10^{-2}
FIR filtered IAW	1.8×10^{-4}	2.4×10^{-4}	1.9×10^{-2}
Morlet Wavelet Filtered IAW	5.9×10^{-5}	1.7×10^{-4}	1.1×10^{-4}
(sign added)	(1.3×10^{-4})	(9.2×10^{-4})	(2.0×10^{-4})
Morlet Wavelet Phase	5.9×10^{-5}	1.5×10^{-4}	7.9×10^{-5}

(b)
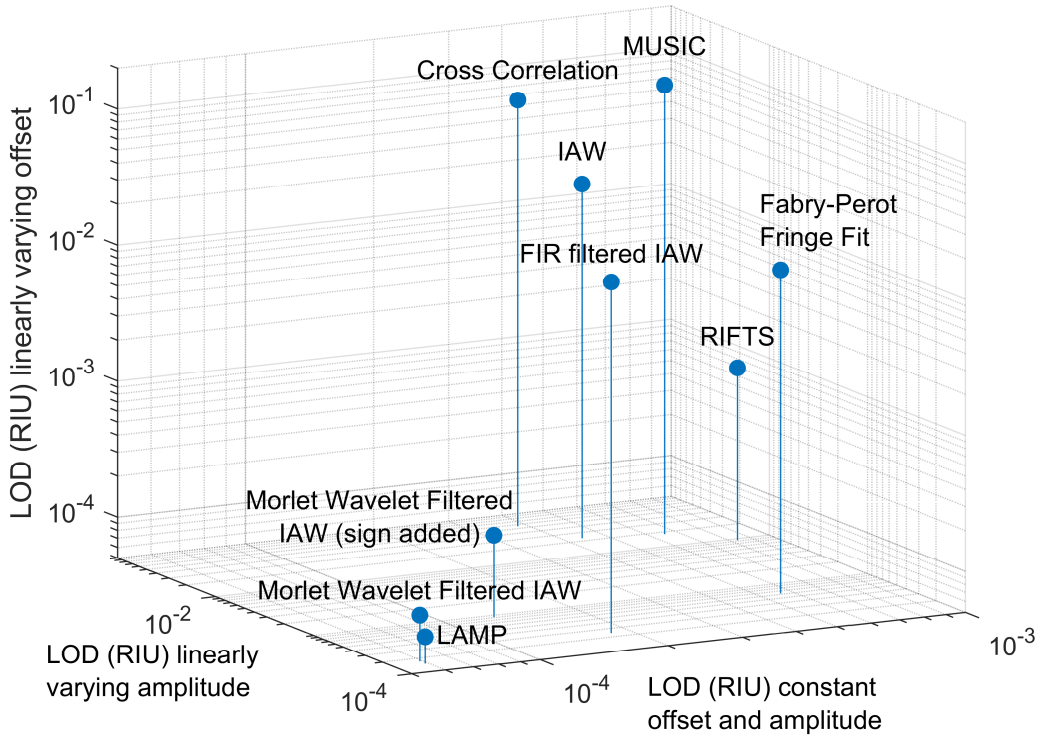
Figure 2.2. Limit of detection in refractive index units (RIU) of analyte solution for several signal processing techniques applied to PSi thin film optical reflectance data generated computationally with added noise, shown in the form of (a) a table and (b) a 3D plot: the closer to the origin, the better the overall noise immunity.

Because the Morlet wavelet is well matched to the Gaussian line shape of the dominant peak of the Fabry-Perot fringes in frequency space, Morlet wavelet convolution is able to apply much stricter band pass filtering than FIR filtering and as a result was much more successful. We note that although Morlet wavelet filtered IAW appears to be competitive with the Morlet wavelet phase method in terms of LOD, for practical application of the technique with PSi sensors, the sign of the reflectance fringe shift must be considered (i.e., directional IAW), which increases the LOD by a factor of approximately 2 – 5 depending on the type of noise present in the signal.

The LOD achievable with each signal processing technique applied to the simulated data sets was then investigated as a function of S/N. Figure 2.3 shows that in the cases of added (a) Gaussian white noise alone and in combination with either (b) offset variation or (c) amplitude variation, increasing S/N leads to a reduction in LOD for nearly all signal processing approaches. For the simulations including only white Gaussian noise, the constant ratio between LOD for any two signal processing techniques indicates that the relative performance of each signal processing method is independent of S/N. However, this is no longer the case in the presence of offset and amplitude variations. For example, the MUSIC algorithm performs exponentially worse as offset variations are increased, whereas other methods employing filtering are relatively insensitive to such noise signatures. When considering the LOD achieved by the RIFTS method, it is interesting to note that although RIFTS yields the highest LOD when applied to simulated reflectance spectra that only include white noise, this method is relatively robust when offset and amplitude changes are introduced. When offset and/or amplitude variations are present in the reflectance spectra, RIFTS outperforms all other signal processing approaches that do not include a separate filtering step. Overall, there is a clear separation in LOD between methods employing filtering and those

48

that do not, which is even more pronounced in the presence of offset and amplitude changes. The exception is FIR filtering which is unable to remove amplitude variations. While amplitude normalization techniques can be applied as a further step after FIR filtering, for example using the Hilbert transform, these techniques were found to be less effective than Morlet wavelet convolution and more expensive computationally so they were not explored further. The final conclusion of the simulation results shown in Figure 2.3 (a-c) is that the Morlet Wavelet Phase method outperforms all other signal processing methods investigated, regardless of the type of noise or S/N. Moreover, there is an approximately linear relationship between S/N and signal processing response in most cases for Morlet Wavelet Phase. Finally, the normalized output of each signal processing technique applied to simulated reflectance data with different refractive index changes was calculated. As shown in Figure 2.3(d), the Morlet Wavelet Phase, RIFTS and Fabry-Perot fringe fitting methods exhibit a linear response to refractive index change, which is advantageous for sensing applications and suggests that these signal processing techniques can be applied to data with a large dynamic range of Fabry-Perot fringe shift.
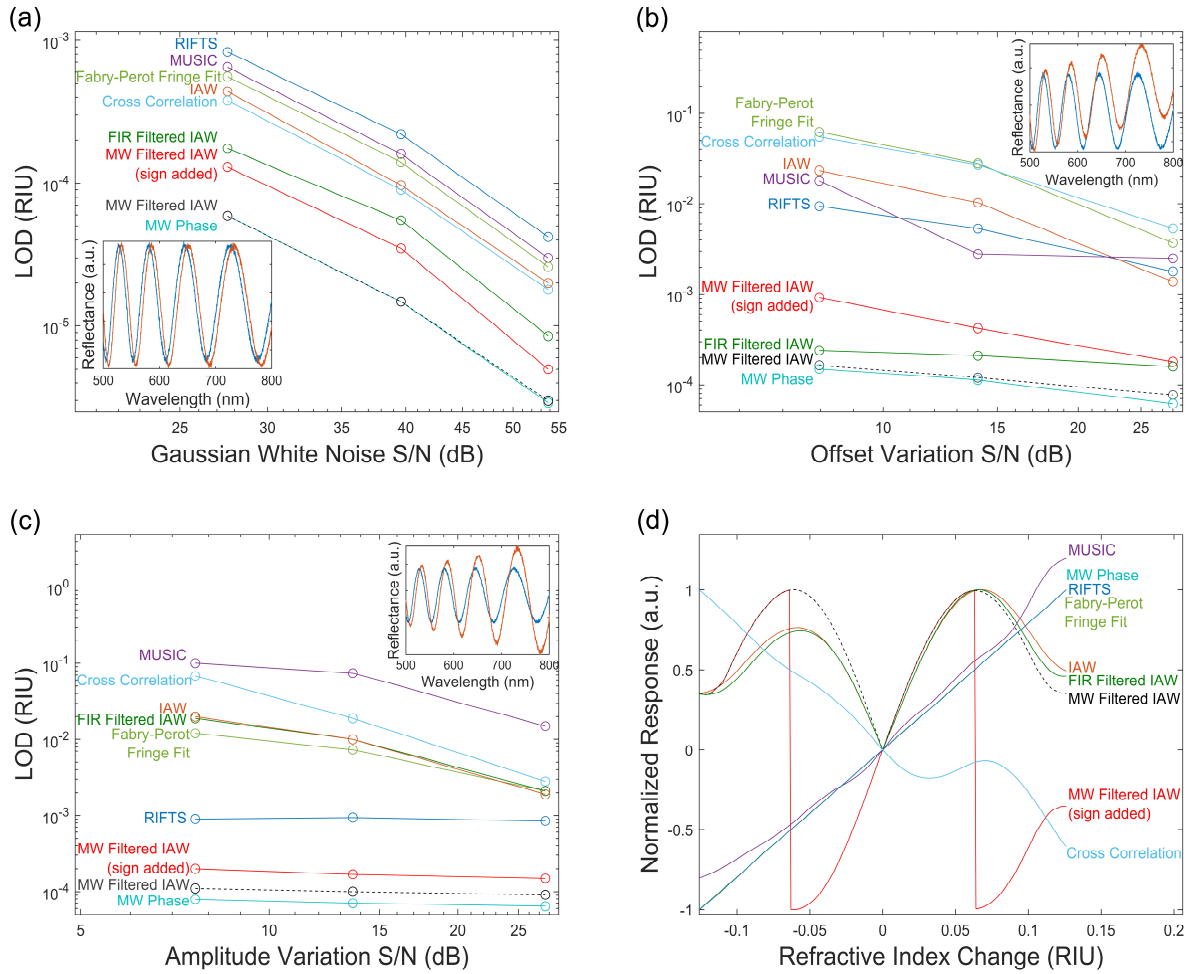
Figure 2.3. Trend between limit of detection and noise level of (a) white Gaussian noise, (b) offset variations and (c) amplitude variations, for a collection of signal processing methods applied to simulated PSi thin film reflectance spectra. (d) Response of each signal processing technique as a function of the refractive index change of analyte applied to a PSi thin film.
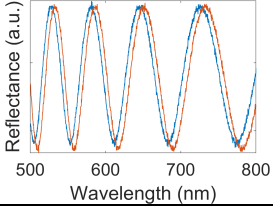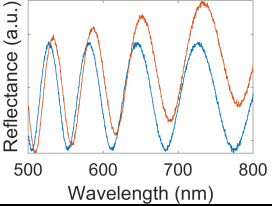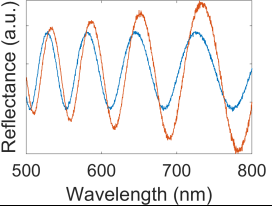
In contrast, all techniques built around the IAW method have a non-linear response with respect to refractive index change. Furthermore, the IAW method returns the maximum response for a shift of the fringes equal to the free spectral range, beyond which the response begins to fall, rendering further shifts unmeasurable. Also notable is that the IAW response is symmetric about the line of zero refractive index shift, meaning that negative refractive index changes cannot be

distinguished from positive refractive index changes unless directionality is introduced into the technique, as shown in the red trace. The cross-correlation approach also suffers from problematic nonlinearities, as does the MUSIC algorithm to a lesser extent. Considering the linear relationship of Morlet wavelet phase signal processing output to refractive index change, and its superior performance in LOD in the presence of multiple types of noise contributions over a large range of S/N, Morlet wavelet phase is clearly a signal processing approach that can improve the performance of thin film optical sensors such as PSi sensors.

2.3.2 Simulation Results Comparing Morlet wavelet phase Method to Gold Standard

As shown in Table 2.1, the Morlet wavelet phase technique achieves a substantially lower LOD than both gold standard RIFTS and IAW methods in all cases of additive white Gaussian noise, linearly varying offset and amplitude signal variations. Since a linear relationship was found between S/N and LOD for each signal processing technique (Figure 2.3), such that the relative merit of the techniques shown in Table 2.1 can be considered independent of Gaussian noise level.

Table 2.1. LOD in refractive index units (RIU) for several signal processing techniques applied to single layer PSi reflectance data generated computationally using the transfer matrix method with added noise.

	Simple refractive index change	Refractive index change with linearly varying offset	Refractive index change with linearly varying amplitude
RIFTS	8.2×10^{-4}	2.5×10^{-3}	8.9×10^{-4}
IAW	3.9×10^{-4}	1.7×10^{-3}	1.9×10^{-2}
Morlet wavelet phase	5.7×10^{-5}	1.3×10^{-4}	7.4×10^{-5}

The RIFTS method performs relatively poorly in the presence of offset variations since the maximum of the dominant fringe frequency peak is shifted by the superposition of lower frequency components. On the other hand, the LOD for RIFTS is almost unchanged for amplitude variations, which only change the power of the dominant fringe frequency peak rather than its position. The IAW method is negatively affected by both offset and amplitude variations; both increase the difference between fringes, which manifests as spurious contributions to the IAW signal. In contrast, the Morlet wavelet phase method gives a comparably low LOD with and without offset or amplitude variations. This reduced sensitivity to noise is a result of the Morlet wavelet convolution, which is an effective technique for filtering thin film interference fringes because it acts as a very strict band pass filter. The shape of a Morlet wavelet closely resembles the shape of Fabry-Pérot fringes in terms of fundamental frequency constituents.

Additionally, due to dispersion, the Fabry-Pérot fringe frequency will not be constant across the spectra; the Morlet wavelet filtering is able to capture this variation because it is localized in wavenumber, while the RIFTS and IAW methods process the data across the spectra simultaneously. Other than noise immunity, complex Morlet wavelet convolution also provides an integrated way of extracting and therefore normalizing amplitude variations; other filtering methods require an additional step, such as applying the Hilbert transform. Furthermore, the inclusion of an FFT in the signal processing pipeline has another advantage, which is a coarse frequency indicator enabling an unlimited measurement range. The IAW method, which does not utilize an FFT, is thus limited to measuring relatively small spectral shifts, particularly when the reference fringe frequency is high: the IAW signal starts to decrease once the peaks of the analyte spectra shift further than the valleys of the reference spectra.

While the computational complexity of the Morlet wavelet phase method may initially appear to be a potential concern for future point-of-care applications, given the combined steps of a FFT, wavelet convolution, and phase difference calculation, embedded implementation of real time FFT and wavelet convolution algorithms have been realized [139]. Accordingly, no insurmountable difficulty is anticipated in designing an instrument using these techniques that can update its readout every few seconds, particularly since such computation time is negligible compared to sensor response times.

Further reduction in achievable LOD with the Morlet wavelet phase technique could be achieved by using a thicker film, optimizing wavelet parameters, and tuning the range of filtered data. Thicker films have higher frequency Fabry-Pérot fringes and an increased optical thickness, which enables better discrimination between the desired signal frequency and unwanted low frequency noise contributions.

However, thick PSi layers may suffer from mass transport challenges that result in longer response times and sensitivity limitations. Mitigation of these challenges may be possible by using larger pore diameters, mixing approaches, and flow through configurations [64,65], although selecting the most appropriate PSi thickness ultimately depends on a balance between noise mitigation and mass transport limitations. Lower LOD may also be achievable by optimizing the width of the wavelet. In this work, the width of the wavelet was intuitively selected to be equivalent to the FWHM of the dominant FFT peak to enable maximum generalizability to any given system. However, there is no fundamental reason why choosing this width would provide the best rejection of noise while retaining the maximum useful portion of the signal. The optimum width of the wavelet depends on the nature of the noise of the system: if the noise is closer in frequency content

to the fringe frequency, a narrower wavelet width will provide a better signal to noise ratio, and vice versa. In this investigation, the range of spectral data filtered and processed is the same for all signal processing techniques. However, in practice some sensing systems will benefit from filtering a wider range of spectral data, but then discarding sections of filtered data at the highest and lowest wavenumber values before processing and obtaining the Morlet wavelet phase result. Finally, higher resolution of the interpolated data and wavelet will improve accuracy at the expense of computational complexity, which is a tradeoff governed by sensor performance requirements.

2.3.3 Comparison Signal Processing Techniques Applied to Experimental Data

BSA Assay

The LOD achievable through application of the Morlet wavelet phase and gold standard signal processing methods to an experimentally obtained data set was investigated by exposing PSi thin film sensors to a series of BSA concentrations, from 0 to 300 μM. The spectra were analyzed, and several adsorption isotherms [140] were fit to the data using nonlinear regression. We assumed that the measurements were independent and normally distributed, while recognizing the heteroscedasticity of the data. As a result, the adsorption model fit required the minimization of the sum of the squared residuals weighted by the inverse of the variance, according to maximum likelihood estimation.

The Redlich-Peterson adsorption isotherm, which is applied to calculate the trend lines shown in Figure 2.4, was the best fit to the data, as determined by calculating the reduced chi squared goodness of fit metric. This adsorption isotherm model implies imperfect monolayer adsorption.

The Redlich-Peterson isotherm is of the form shown in Eqn. (2.1)

$$\theta = I + \frac{AC_e}{1 + BC_e^{\beta}} \tag{2.1}$$

where θ is the response of the signal due to biomolecule adsorption, C_e is the equilibrium concentration of BSA solution, and the fitting parameters are: I, the intercept or predicted response to a pure buffer control, A, the Redlich-Peterson isotherm constant, B, a constant, and β, another constant between 0 and 1. The IAW line of best fit is complicated by the inherent nonlinearity of the method, as evidenced by the IAW response decreasing when the BSA concentration is increased from 3 to 300 μM (Figure 2.4 (b)). The Morlet wavelet phase and RIFTS responses, which are linear, show that this concentration range is nearing the saturation region (Figure 2.4 (a) and (c)), and thus the response should continue to increase in this range. The apparently different trend for IAW can be accounted for by observing that the largest spectral shift for a concentration of 300 μM, exceeds the free spectral range limit of the IAW method (Figure 2.4 (d) inset). To take the nonlinearity into account, the deviation from a linear response as a function of percentage change in RIFTS response was determined by simulation using the transfer matrix method and was fit with a second order polynomial. The adsorption isotherm was then scaled by this nonlinearity using the measured percentage change in RIFTS response, but was otherwise fit to the data in the same way as the other methods. The LOD was determined by finding the concentration at which the Redlich-Peterson adsorption isotherm line of best fit exceeds its intercept by $3.3\sigma_{blank}$, the noise floor in the blank. The fitting parameters and LOD for the RIFTS, IAW and Morlet wavelet phase methods are shown in Table 2.2, and the data, the Redlich-Peterson adsorption isotherm line of best fit and the noise floor for each method are shown in Figure 2.4. The Redlich-Peterson adsorption models simplifies to the Langmuir isotherm when $\beta = 1$. For all

three signal processing methods, the optimal value for β is close to 1, suggesting only a small perturbation from ideal monolayer formation on a homogenous surface.

The relative differences in LOD values between the signal processing techniques seen experimentally (Table 2.2) are in good agreement with the theoretical predictions of Table 2.1. Since the BSA assay is a simple experiment in buffer solution, the presence of noise signatures is minimal and compares favorably with the simple refractive index change case in Table 2.1. The lowest LOD achievable for BSA is 200 pM (4 femtomoles in a 20 μL solution) when the Morlet wavelet phase method is applied, which is one order of magnitude lower than for IAW and RIFTS methods. The LOD values shown in Table 2.2 are not as low as those recently reported in the literature for a PSi sensor [121]. The predominant reason lies in the method of calculating LOD. Common practice is to center the noise floor around 0, rather than centering the noise floor around the intercept of the line of best fit. However, centering the noise floor around 0 is misleading because if the intercept is increased, the LOD can be artificially decreased and, more-over, the LOD becomes undefined when the intercept is outside the noise floor. Hence, the method we use for calculating LOD in this paper is a more conservative, and importantly, a more robust approach, and is consistent with the formulation defined by IUPAC and others [85,141]. A similar LOD to that reported here is obtained when this approach (i.e., centering the noise floor at the intercept) is applied to other comparable published datasets [121].
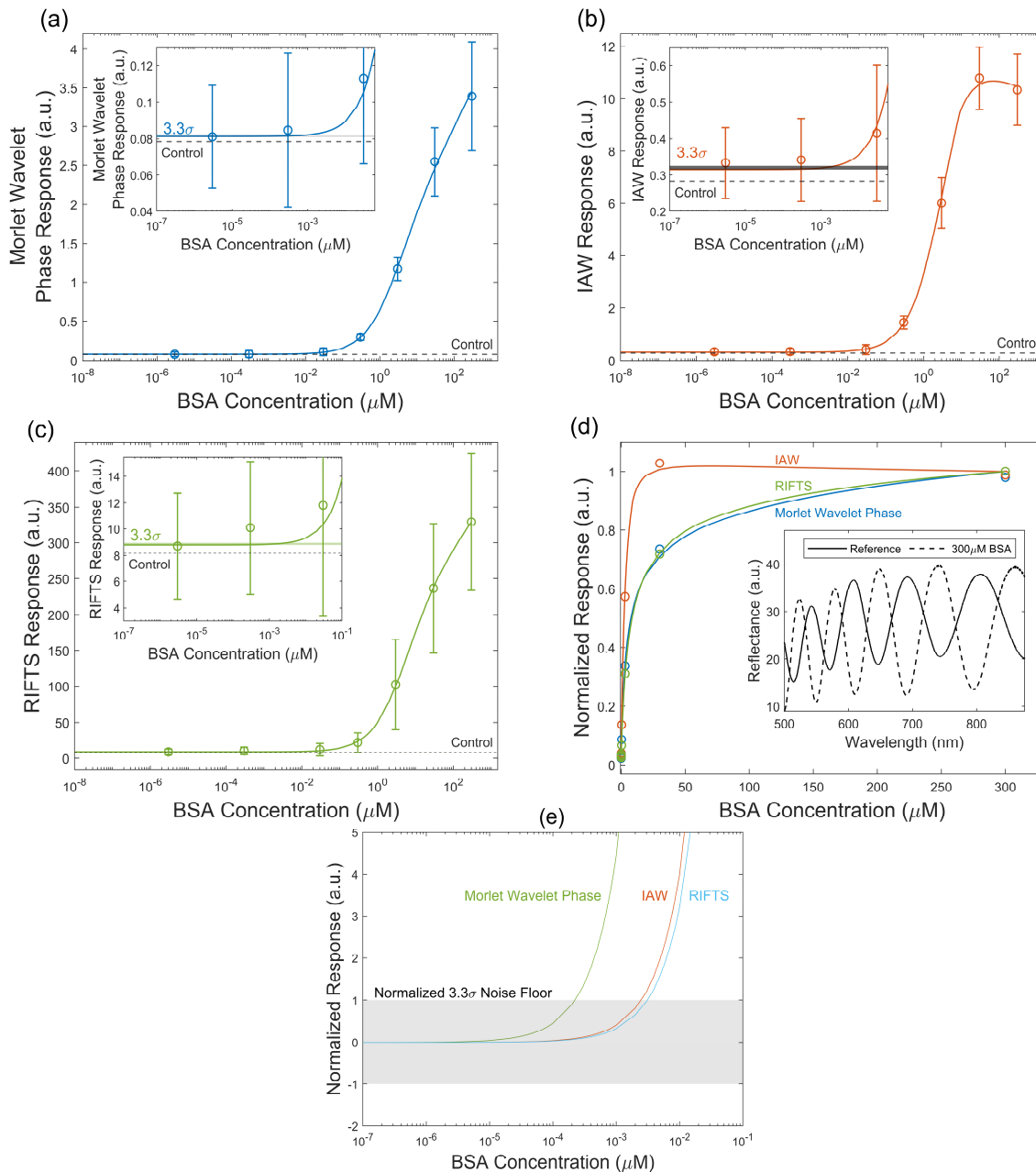
Figure 2.4. Results of exposing a single layer of oxidized PSi to solutions of BSA in buffer, with concentrations between 0 and 300 μM, analyzed using (a) Morlet wavelet phase, (b) IAW, and (c) RIFTS signal processing methods, shown on a semi-log plot. A Redlich-Peterson adsorption isotherm line of best fit is overlaid, as well as the noise floor for each method. The insets show the data, noise floor and trendline in the region of the LOD. Responses of all signal processing techniques as a function of BSA concentration normalized by the saturation response (d) on a linear scale, with an inset illustrating the maximum shift caused by 300 μM BSA exposure, and by the noise floor (3.3σ) (e) on a log scale.

Table 2.2. LOD for BSA exposure analyzed using IAW, RIFTS and Morlet wavelet phase signal processing methods, showing noise level and Redlich-Peterson adsorption isotherm fit parameters.

	3.3σ (a.u.)	LOD (nM)	I (a.u.)	A(LM^{-1})	B(LM^{-1})	β
RIFTS	1.62×10^{-1}	3.2	8.78	50.16	0.24	0.92
IAW	1.00×10^{-2}	2.5	0.32	4.02	0.37	0.95
Morlet wavelet phase	1.85×10^{-4}	0.2	0.08	0.82	0.47	0.88

AGR2 Assay

The robustness of the Morlet wavelet phase method to low frequency offset and amplitude variations, in comparison to the RIFTS and IAW methods, was investigated through the application of the signal processing techniques to experimental data of an aptamer-based single-layer PSi biosensor. This biosensor is designed to selectively target AGR2 protein and consists of oxidized PSi thin films, in which amino-terminated anti-AGR2 aptamers [142] are immobilized via NHS/EDC coupling chemistry [137]. Reflectance measurements of the biosensor upon exposure to the target AGR2 protein and non-target IgG protein (at a concentration of 100 µg mL^{-1} and 200 µg mL^{-1}, respectively) in buffer solution and 100 µg mL^{-1} AGR2 in plasma were carried out. The reflectance data shown in the insets of Figure 2.5 reveal that both offset and amplitude variations are present in the measured data.

We note that the magnitude of the RIFTS, IAW, and Morlet wavelet phase processed signals were normalized to lie within the same range for ease of comparison. Common trends are shown in the data processed with RIFTS, IAW, and Morlet wavelet phase: (1) a relatively stable baseline value is established during buffer solution incubation, (2) a large increase in signal magnitude occurs when the AGR2, IgG protein, or plasma alone is introduced due to the change in the refractive index of the introduced solution compared to the baseline buffer and diffusion into

the pores, (3) as the solution is incubated on top of the PSi, for solutions containing AGR2 there is a more gradual increase in signal due to target protein binding to the aptamers immobilized on the pore walls, conversely for control solutions negligible additional signal change occurs, (4) a signal reduction occurs when a buffer rinse is carried out to remove unbound protein from the pores, and (5) a relatively stable new baseline value is established in most cases upon incubating the sample with buffer solution once again.
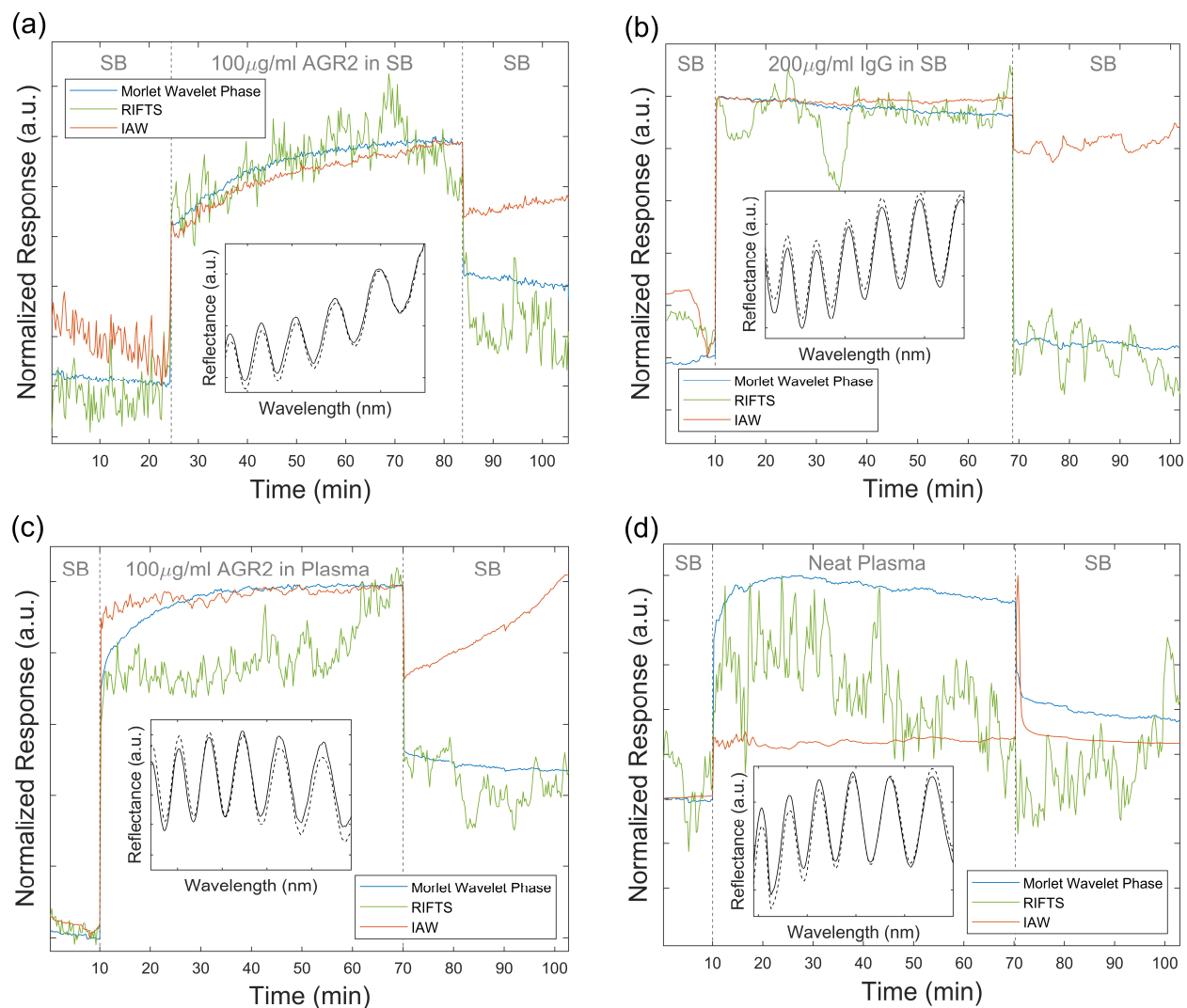
Figure 2.5. Comparison of signal processing techniques applied to experimental data collected by exposing the single-layer PSi biosensor to (a) $100\,\mu g\,mL^{-1}$ AGR2, the target protein, in buffer solution, (b) $200\,\mu g\,mL^{-1}$ non-target protein IgG in buffer, (c) $100\,\mu g\,mL^{-1}$ AGR2 spiked in 50% plasma in buffer, and (d) 50% neat plasma in buffer. In all cases, there is a pre- and post-wash in buffer. Insets show reflectance spectra taken during the pre- and post-wash steps; signal offset and amplitude variations (i.e., noise signatures) can be observed.

Key differences in S/N, ability to resolve protein capture dynamics, and accuracy of the biosensing result can be seen by comparing the signals processed by RIFTS, IAW, and Morlet wavelet phase methods in Figure 2.5. When using RIFTS, the noisy signal makes it difficult to

determine the magnitude of the signal change due to protein capture with high accuracy and also makes it more challenging to ascertain target protein capture dynamics. Low frequency noise signatures lead to false trends for protein capture in IAW data, which is of significant concern for the accuracy of the PSi biosensor. In Figure 2.5 (b), the IAW method suggests that there is a large signal change when the sensor is exposed to the non-target protein, giving a false positive result. In Figure 2.5 (d), artifacts in the IAW signal are present due to the IAW response predominantly to offset changes. Moreover, in Figure 2.5 (a, c), the IAW method suggests an unexpected continually increasing signal during the post-protein exposure buffer rinse and incubation, which is not consistent with the RIFTS and Morlet wavelet phase results and is physically misleading. Such an increase in the optical signal would typically be attributed to molecules diffusing into the porous layer, leading to a corresponding increase in the PSi effective refractive index; however, no protein is present in the solution on top of the biosensor at this stage [65]. It is important to note that because the IAW processed response can be dominated by the change in offset and amplitude of the reflectance spectra, instead of by frequency shifts that are present due to molecular attachment, caution must be taken to eliminate systematic noise sources in experiments when utilizing the IAW method. Otherwise, it is possible that the IAW result may be disconnected from the physics of the system, as exemplified in Figure 2.5 (c, d). We note that the data presented in Figure 2.5 are representative of all the data collected: the IAW response exhibited artifacts or a false response that did not reflect the physical system in more than 50% of all experiments and in 100% of the non-specific protein experiments.

In all cases studied in Figure 2.5, the Morlet wavelet phase method is shown to be the most robust and reliable signal processing approach. There is a clear distinction between signal changes

for target protein capture, negligible signal change when the biosensor is exposed to a non-target protein in buffer, and a small non-specific binding induced signal change when the biosensor is exposed to non-spiked plasma. While the Morlet wavelet phase and RIFTS signal processing techniques lead to similar final results for most biosensing experiments, the Morlet wavelet phase signal has a much higher S/N ratio than the RIFTs signal, which should lead to a lower experimentally demonstrated LOD. Moreover, the Morlet wavelet phase method clearly elucidates the target protein capture dynamics.

2.4 Summary

Applying the Morlet wavelet phase technique, which is based on complex Morlet wavelet band pass filtering and calculation of average phase difference, to PSi thin film biosensor reflectance data provides a robust, low noise measure of frequency shifts that arise due to biomolecular recognition and binding events in the pores. The key benefits of the Morlet wavelet phase method are reducing the effect of noise present across the frequency spectrum and mitigating spurious signal changes that otherwise result from low frequency variations in the offset and amplitude of measured spectra. Analysis of both simulated data and experimental data from a BSA assay demonstrate that the Morlet wavelet phase method achieves a LOD that is approximately one order of magnitude lower than that of RIFTS and IAW – two other signal processing approaches used to analyze data from PSi thin film sensors and biosensors. Moreover, it was shown that the Morlet wavelet phase method can be reliably applied to noisy data acquired in complex biological media. Improved S/N and selectivity were demonstrated by applying Morlet wavelet phase to data from an aptamer-based biosensor for targeting a cancer biomarker, AGR2 protein,

compared to the application of RIFTS and IAW to the same data set. The robustness and lower

detection limit achievable by employing the Morlet wavelet phase signal processing technique can

benefit many applications where noise in data sets cannot be perfectly controlled and low detection

limits are required for clinical relevancy.

CHAPTER 3

Capture Agent Free Biosensing using Porous Silicon Sensor Arrays and Machine Learning

Parts of this chapter are adapted from "Protein Identification and Quantification Using Porous Silicon Arrays, Optical Measurements, and Machine Learning" published in Biosensors and reproduced with permission from publisher, and "Analysis of Machine Learning Techniques for Capture Agent Free Biosensing with Porous Silicon Arrays" published in SPIE Proceedings and reproduced with permission from publisher.

S. J. Ward, T. Cao, X. Zhou, C. Chang, and S. M. Weiss, "Protein Identification and Quantification Using Porous Silicon Arrays, Optical Measurements, and Machine Learning," *Biosensors* 13(879), 1–12 (2023).

S. J. Ward, Tengfei Cao, Catie Chang, and S. M. Weiss, "Analysis of Machine Learning Techniques for Capture Agent Free Biosensing with Porous Silicon Arrays," *Proc. SPIE, 11979* (1197907), 1–6 (2022).

3.1 Introduction

The need to detect biological analytes for applications including medical diagnostics, environmental monitoring, and food safety, is typically met by a biosensor composed of three primary components: a capture agent (also sometimes referred to as a probe molecule or bioreceptor), which specifically binds to the desired target analyte, a transducer, which converts the binding of the target species into a measurable optical, electrochemical, thermal, or

microelectromechanical signal [5,6,14–18], and a data processing unit which converts this measurable signal into a user friendly and accessible output such as a reading on a display. Examples of specific capture agent–target analyte 'lock and key' interactions are antibody–antigen interactions, enzyme–substrate interactions, peptide interactions, and oligonucleotide interactions [11–13]. However, despite their effectiveness and well-established use in many applications, the reliance on capture agents for analyte detection can bring about several challenges. The first is that a capture agent, by design, typically only binds to one species. If the aim is to identify and quantify multiple molecular constituents in a solution of unknown composition, multiple capture agents are required, which leads to larger, more complex, and expensive biosensors. Furthermore, if the appropriate capture agents are not present on a sensor, there is a possibility of hazardous species going undetected. In addition, many capture agents denature or degrade over time and/or in harsh environments, which limits the shelf life, ease of transportation, and types of locations where the sensor can be used [91–93]. Finally, when challenged with detecting a new target molecule of interest for which there is no existing capture agent, it can take significant time to develop an effective capture agent with sufficient specificity and affinity [143–145].

While there are molecular sensing approaches that do not require capture agents, they are not without their challenges as well. For example, spectroscopic techniques and many other protein detection assays typically require costly and bulky instrumentation, and their performance for analytes in complex media can often be limited [146]. Moreover, cost, ease and scalability of manufacture, and high sensitivity remain significant challenges for molecular imprinting approaches [147,148]. In addition, electronic noses or tongues typically face a trade-off between

sensitivity and robustness, stability, complexity, and cost, especially when operating outside of controlled environments [36,39,149–154]. Different sensor platforms used in cross-reactive sensor arrays have their own inherent limitations. For example, colorimetric sensor arrays, which have been the subject of wide research interest, are limited in terms of their number of array elements due to the complexity of their manufacture, reproducibility, and printing quality; the minimum spot size of chemo-responsive dyes as a result of edge effects and a limited printing resolution; and their utility in detecting analytes in the aqueous phase, which poses additional significant challenges and often results in underwhelming detection limits (>1 μM) [149].

In this chapter, we report an initial demonstration showing that, under the appropriate preparation conditions, an array of porous silicon (PSi) sensors [7,60,63,68,155–157] has the potential to robustly classify, quantify, and discriminate a select number of molecular species without capture agents, based on their size, conformation, and surface charge. In particular, we demonstrate the detection of three proteins—bovine serum albumin (BSA), chicken ovalbumin (OVA), and avidin—separately, without the use of capture agents. These proteins, suspended in buffer solutions with varying pHs, are exposed to PSi films with different pore sizes. The proteins were chosen for this initial demonstration based on their overlapping combinations of isoelectric points and molecular weights, and because they are well characterized, which allows for the incorporation of prior knowledge into the machine learning analysis. The proteins can be discriminated at concentrations down to at least 300 nM, meeting clinically relevant detection limits for many applications [158–160] with 100% accuracy when the discrete set of possible concentrations is known, and 87.5% accuracy when classifying the protein type only for unseen concentrations. Given the large internal surface area and strong light matter interaction afforded

by PSi, we anticipate that lower detection limits are achievable with further refinement of the platform and the inclusion of more degrees of freedom in the array element design and experimental testing conditions. The novel approach presented here for protein identification and quantification uniquely bridges the trade-off between the robustness and sensitivity of current sensor arrays by probing a wide reactivity space (encompassing more than purely hydrophobicity [39]) without requiring any surface treatments. Furthermore, PSi sensor arrays are cost effective, straightforward to fabricate, and easily scalable to high-volume manufacturing and large numbers of sensor array elements, to an extent which is not possible with most other platforms. This work opens the door to more advanced studies investigating the limits of using capture-agent-free PSi arrays for molecular identification and quantification in mixtures and other complex solutions.

3.2   Experimental Methods

3.2.1   Preparation of Single Layer PSi

Single-layer PSi thin films were fabricated [7,60] by electrochemically etching p-type single-side polished, boron-doped silicon wafers ($\langle 100 \rangle$, 0.01−0.02 Ω cm, 500−550 μm, Pure Wafer, San Jose, USA) using a 15% v/v solution of aqueous hydro-fluoric acid (HF; 48–51%, Acros Organics, Antwerp, Belgium) in ethanol (Thermo Fisher Scientific, Waltham, USA) in an Advanced Micromachining Tools (AMMT, Frankenthal, Germany) MPSB PSi wafer-etching system. Note that HF is an extremely dangerous chemical and should be handled with the utmost caution [7], and that alternative fabrication methods exist [161]. The wafer was secured in a wafer holder, which was immersed in a HF bath. The wafer holder was subsequently clamped against an

inner wall of the etching tool with an o-ring seal, which isolated two half cells, each containing a platinum mesh electrode. The anode was in contact with the exposed back side of the wafer in one of the half cells, the cathode was immersed in the HF bath in the other half cell, and a voltage was applied between the electrodes to provide a constant etching current. Firstly, a sacrificial layer was etched using a current density of 70 mA cm^{-2} for 100 s, which was subsequently dissolved in a 1 M NaOH solution. Secondly, the wafer was washed with deionized (DI) water (resistivity 15 MΩ cm, Elix water purification system, Millipore, Burlington, USA) and ethanol to remove the HF residue and then etched again at a current density of either 55 mA cm^{-2}, 40 mA cm^{-2}, or 25 mA cm^{-2}, to form thin films with different pore size distributions for the different elements in the sensing array. The etching time used to fabricate the PSi films (57 s, 66 s, and 93 s for 55 mA cm^{-2}, 40 mA cm^{-2}, and 25 mA cm^{-2}, respectively) was tailored to give approximately the same thickness, regardless of the etching current density (and associated etch rate). We note that, if experimental conditions such as the HF electrolyte concentration, temperature, and electrode size, position, and conductivity are precisely controlled, then the fabrication is repeatable. Thirdly, the wafer was diced into square 5 mm × 5 mm samples using a DISCO (Tokyo, Japan) DAD3220 dicing saw. Finally, the samples were oxidized at 800 °C in ambient air for 10 min, forming a passivating surface layer of SiO$_2$, which is hydrophilic and accumulates a negative surface charge in pH > 2 conditions.

3.2.2 Material Characterization

The properties of the PSi films were measured by analyzing scanning electron microscope (SEM) top-view and cross-sectional images; one PSi sensor for each etching current density was imaged to calculate the pore size distribution (Figure 3.1) and four PSi sensors for each etching

current density were imaged to compute the mean pore size, porosity, and thickness (Table 3.1). To extract the pore distribution and average pore size, analysis was carried out in MATLAB (R2022b) [162] in a similar manner to that previously reported [89,163]. First, the contrast of the top-view SEM images was made uniform across the image and enhanced using the adapthisteq MATLAB function [164], and then a threshold was used for conversion into a binary image. Isolated pixels were removed and a median filter was applied. The perimeter and area of each of the pores were found using the regionprops MATLAB function, and the pixel to nm conversion was performed using the scale bar in the SEM images. The count of pores in each bin of the pore distribution histogram was weighted by the average perimeter length for each of the pores in that bin. The four top-view SEM images for each etching current density, representing an area of 5.3 μm^2 or approximately 0.1% of one PSi sensor, were analyzed and the results were averaged to extrapolate the pore size distribution of the PSi as a whole. Similarly, ten measurements across four cross-sectional images were used to calculate the thickness of the PSi layer for each etching current density. For both the pore size distribution and thin film thickness, the errors reported are the standard deviation of the measurements.

3.2.3 Optical Reflectance Measurements

Reflectance spectra were collected by fiber-coupling broadband white light from a quartz tungsten light source into a bifurcated optical fiber through one fiber port and measuring the reflected light using an Ocean Optics (Orlando, USA) USB 4000 CCD spectrometer connected to the second fiber port. The height of the fiber was adjusted to form a spot size with a 5 mm diameter on the PSi sensor surface. The result from averaging 100 successive output spectra was saved once per second.

3.2.4 Experimental Procedure

The PSi samples (5 mm × 5 mm) were washed with water and ethanol and dried under nitrogen. The reflectance spectra of the sensing elements in an array were measured before protein incubation to establish a baseline reference spectrum; representative reflectance spectra for each etching current density are shown in Figure 3.1 (d). To keep the experimental conditions as consistent as possible across the large number of experiments needed to compile a reasonable dataset for analysis, bulk protein solutions were prepared in DI water (10 g/L) and stored at 4 °C. The bulk protein solutions were further diluted with either pH 10 and pH 4 reference standard buffers (Sigma-Aldrich, Burlington, USA) and water to prepare three concentrations of each protein (2 g/L, 0.2 g/L, and 0.02 g/L). The ratio of DI water:reference standard buffer (pH 4 or pH 10) was maintained at 1:4 for all the experiments; this ratio was chosen as a tradeoff between maximizing the proportion of the buffer for optimal pH control and stability and a sufficiently high volume of protein solution to enable a large dynamic range of accessible concentrations using 10 g/L stock protein solution. The pHs of the solutions using the pH 4 buffer and pH 10 buffer were found to be 4.0 ± 0.1 and 10.0 ± 0.1, respectively, measured using a Mettler Toledo (Columbus, USA) Seven Easy pH meter. The corresponding molar concentrations of the protein solutions were 30 µM, 3 µM, and 300 nM for BSA (pI = 4.63, MW = 66.4 kDa, Thermo Fisher Scientific), 45 µM, 4.5 µM, and 450 nM for OVA (pI = 4.54, MW = 44.3 kDa, Thermo Fisher Scientific), and 30 µM, 3 µM, and 300 nM for avidin (pI = 10, MW = 66–67 kDa, Thermo Fisher Scientific). A 20 µL volume of protein solution was drop cast on each sensing element in the array and left to incubate for 2 h under ambient conditions in a sealed container to prevent evaporation. Afterwards, the sensors were placed in an 800 mL water bath for 10 s, and then removed and dried under nitrogen.

The purpose of this wash was to remove unbound molecules from the PSi surface and inside the pores. A much smaller number of weakly bound molecules were also removed, but the reflectance change during the washing was small and almost entirely independent of the wash duration, indicating that most molecules were adsorbed strongly enough to remain in the pores. Each sensing element in the array was then dried under nitrogen and measured again, and the resulting spectrum was compared to the reference spectrum before protein solution exposure by calculating the Morlet wavelet phase response (Section 2.1.3) [78]. The total number of elements in each array that were exposed to one concentration of a given protein was twelve, corresponding to three average pore sizes, two buffers, and two repeats which were averaged. Since each sensor element was 5 mm × 5 mm, the total area of each sensor array was 300 mm^2. Linear discriminant analysis (LDA) was used to reduce the dimensionality and visualize the six-dimensional sensor array responses in 3D, elucidating the separability of the three proteins.

3.2.5 Data Analysis

A selection of machine learning models, with the potential of making accurate predictions on this comparatively small training dataset, were implemented using Scikit-learn [165] and trained on both the original and reduced dimensionality training datasets. The accuracy of the machine learning models was estimated using leave one out cross validation due to the limited training data. The specific models investigated were support vector machines (SVMs) with linear, radial bias function and sigmoid kernels, random forest, logistic regression, and k nearest neighbor classifiers [166]. Additionally, the accuracy achieved when averaging the response matrices from two sensor arrays was compared to the case where there was no averaging. For the pairwise averaging training dataset, the pairs of repeated data points to average were randomly selected,

71

and similarly for the non-averaged training dataset half the data points were randomly selected and the other half were discarded to keep the training data set size consistent, which ensures a fairer comparison.

3.3 Results and Discussion

The PSi thin films were fabricated using three different current densities, achieving three distinct pore size distributions with different average pore sizes. The pore size distributions were weighted by the circumference of the pores, which is proportional to the number of binding sites.

Table 3.1 shows the average pore diameter and thickness, which were determined by analyzing the SEM images; porosity, which was calculated from the optical reflectance measurements; and average effective optical thickness and refractive index, which were calculated through an analysis of the reflectance spectra, as a function of the etching current density.

The appropriate selection of PSi formation conditions, including current density, etching time, HF concentration, and silicon wafer doping, enables a relatively wide range of tunability in the PSi properties shown in Table 3.1 [7]. Both Figure 3.1 and Table 3.1 show the pore size distributions shifting to larger diameters as the etching current density was increased. Important for size selectivity, the fraction of larger (>30 nm) pores dramatically increased by an order of magnitude as the etching current density increased from 25 mA cm^{-2} to 40 mA cm^{-2} and increased again by a factor of nearly three as the etching current density was increased to 55 mA cm^{-2}. We believe this metric was a dominant effect governing the response of the PSi films to protein exposure compared to the average pore size, which exhibited only a modest increase with etching current density. While the porosity also increased as a function of the etching current density,
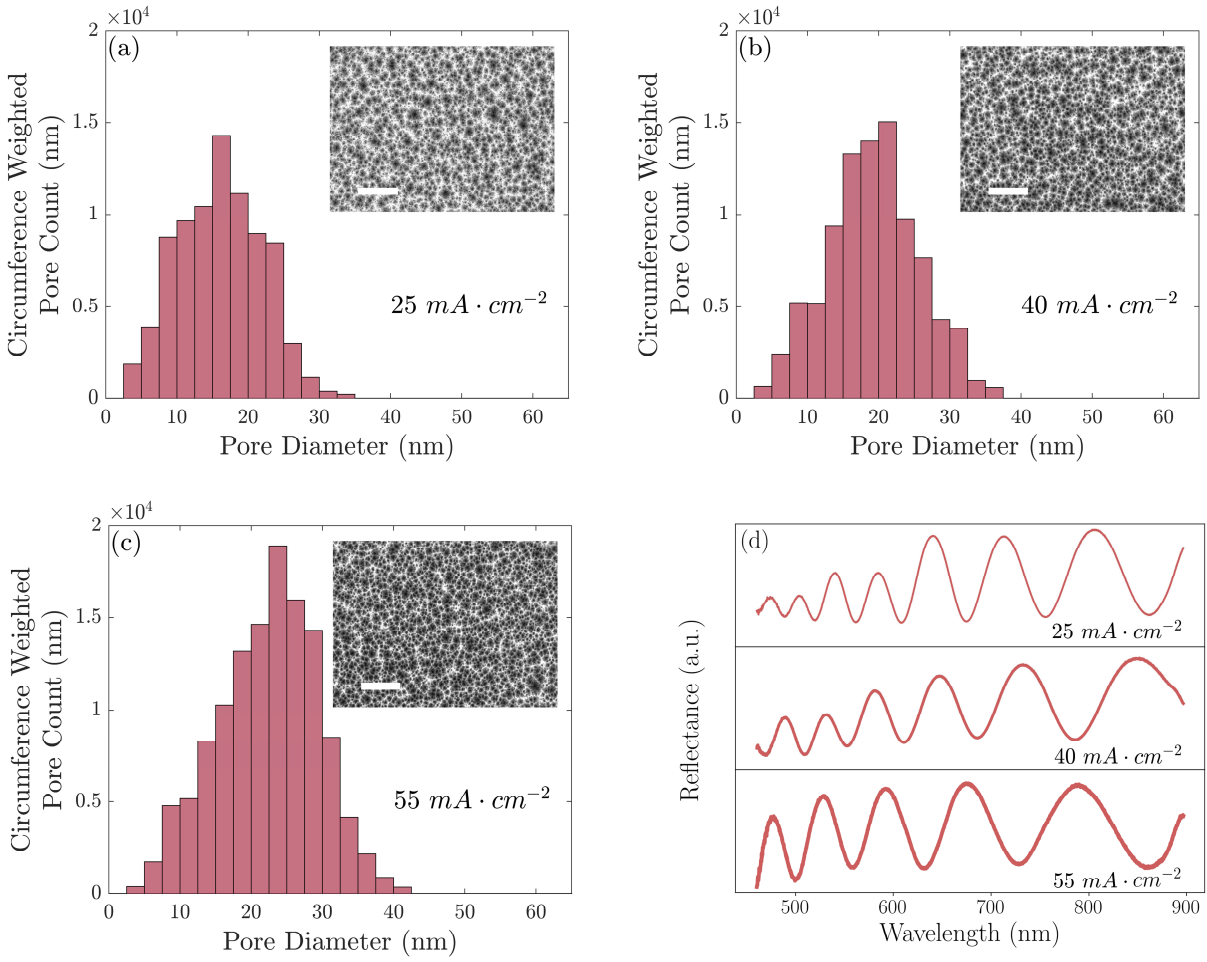
Figure 3.1. Pore diameter distributions and SEM top-view images for three PSi films, one for each etching current density, formed with current densities of (a) 25 mA cm⁻², (b) 40 mA cm⁻², and (c) 55 mA cm⁻². (d) Measured reflectance spectra for each of these PSi films. Scale bars on SEM images are 500 nm.

Table 3.1. Average pore size, porosity, thickness, and fraction of pores larger than 30 nm determined from measurements of four PSi thin films for each of the three etching current densities used to fabricate elements of the sensor array.

Etching Current Density	25 mA cm⁻²	40 mA cm⁻²	55 mA cm⁻²
Mean Pore Diameter (nm)	12.0 ± 0.2	15.1 ± 0.2	17.3 ± 0.2
Pore Diameter Standard Deviation (nm)	6.0 ± 0.2	6.7 ± 0.3	7.9 ± 0.3
Thickness (μm)	1.78 ± 0.01	1.94 ± 0.01	2.04 ± 0.01
Mean Effective Optical Thickness in Air (μm)	6.91	6.34	5.82
Mean Effective Refractive Index in Air	1.94 ± 0.02	1.63 ± 0.01	1.43 ± 0.01
% Porosity	53 ± 1	61 ± 1	66 ± 1
Fraction of Pores > 30 nm	0.2 ± 0.1%	2.0 ± 0.4%	5.8 ± 1.3%

porosity changes would alter the response of all the proteins proportionally and, consequently, would provide no additional discriminatory information, unlike the pore size, which had an important differential effect [167]. We note that our analysis of the top-view SEM images established a clear general trend of an increasing pore size with an increasing etching current density. Thresholding to convert the images from greyscale into binary was performed manually and the fine structure of the pore branches within the pores was not rigorously taken into account. Consequently, although the standard deviation of the repeated independent measurements was low, there could have been systematic uncertainty associated with the resolution of the SEM images and manually chosen thresholds. Further detailed analyses of the pore size and morphology for PSi layers fabricated using a range of different etching conditions can be found elsewhere [155,168,169].

Solutions of BSA, OVA, and avidin at three different concentrations and a negative control with no protein were prepared in DI water and either pH 4 or pH 10 buffers at a ratio of 1:4, resulting in overall solvent pHs of 4.0 ± 0.1 and 10.0 ± 0.1, respectively. The solutions were drop cast and incubated for 2 h on the PSi films with three different pore sizes, resulting in six combinations of pore sizes and pHs in the sensing array. Sixteen of these sensor arrays were constructed for every concentration of each protein, and randomly sampled pairs of array measurements were averaged to reduce the variance in the response arising from the nature of the adsorption phenomenon, yielding eight independent repeats, allowing for an estimation of the mean and variance for every experimental condition. The reflectance spectrum of each sensor array element was measured before and after the protein solution exposure, and spectral shifts indicative

of infiltration and adsorption in the pores were transduced by processing the spectra using Morlet wavelet phase analysis [78]. Here, infiltration refers to the diffusion of molecules into the pores and adsorption refers to the attachment of the molecules to the pore walls.

From the response of each sensor in the array (Figure 3.2), it was clear that the differences between the proteins were subtle at low concentrations, but easily discriminable by eye at the highest concentrations, allowing for several observations to be made. Firstly, the response to all the protein solutions was proportional to the pore size: as the pore size distribution shifted to higher diameters and the average pore size increased, the response increased, as expected [170]. Notably, the relationship between the response and pore size for a given protein was not linear, and there were three regimes to consider: (1) at higher average pore sizes, the proteins experienced essentially uninhibited entry and diffusion into the majority of the pores, (2) at lower average pore sizes, inhibited molecular transport began to pinch off the response because there were few pores large enough to permit infiltration and adsorption, and (3) at intermediate pore sizes, there was a transition between the other two regimes.

A second observation can be made regarding the effect of pH on the response of the PSi films. Multiple studies have shown that the maximum infiltration of proteins in the pores occurs when the pH environment is at the isoelectric point of the protein, resulting in a net neutral molecular charge [171,172]. This condition provides the minimum inhibition of protein transport and promotes close packing in the pores by avoiding extensive protein–protein and protein–PSi interactions. Accordingly, the results in Figure 3.2 show that the largest response of the PSi to each of the proteins occurred when the pH of the solution was approximately equal to the isoelectric point of that given protein. We note that the surface of the oxidized PSi was negatively charged

75

when the pH of the environment was above 2, which was the case for all the experiments carried out in this work [173]. We further note that, while the pH at which maximum adsorption occurred was indicated simply by a molecule's isoelectric point, the dependence of the adsorption characteristics on the pH will generally have a different shape for every molecule, providing another fingerprinting mechanism: the properties governing infiltration and adsorption, such as protein charge distribution [174], agglomeration, and conformational changes [175], are unique to any given molecule and are pH-dependent.
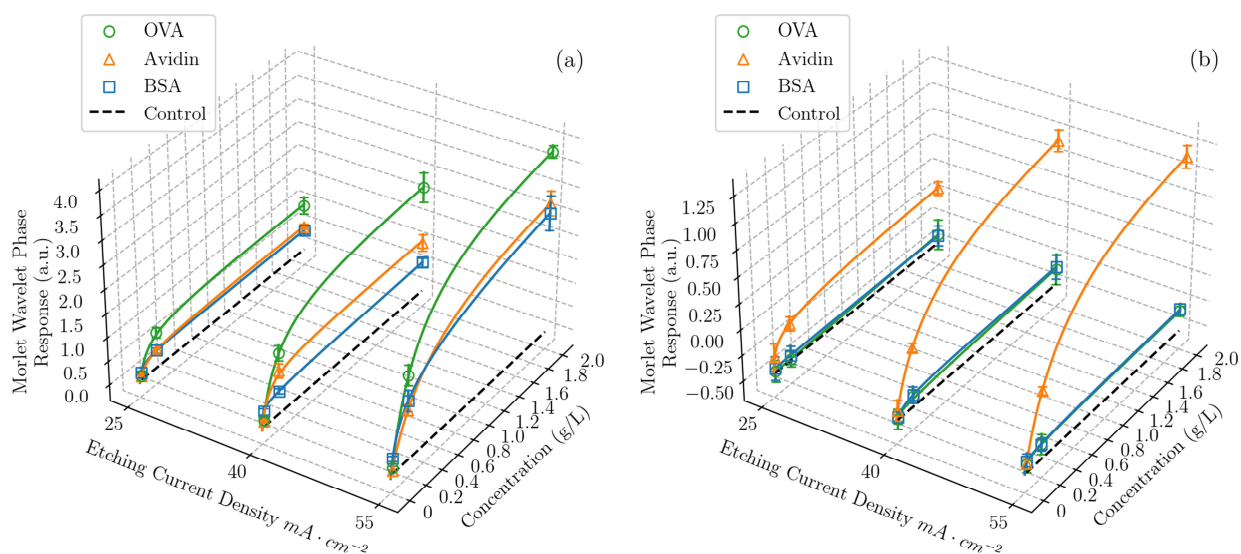
Figure 3.2. Morlet wavelet phase response as a function of both etching current density (proportional to average pore size) and concentration for three proteins—OVA, BSA, and avidin—and a negative control with no protein, in solutions of DI water and (a) pH 4 and (b) pH 10 buffer, in a ratio of 1:4 (v/v). The data points represent the average value of sixteen measurements taken at the same condition and the error bars represent the standard deviation of the measurements. Each response curve was fit with the Redlich–Peterson adsorption isotherm [176].

Thirdly, by combining the first two observations, we can understand that, when the pH 4 buffer was used, close to the isoelectric point of both OVA and BSA, a higher response was given by OVA due to its smaller molecular size.

Finally, for the solutions using the pH 10 buffer, the baseline was negative due to the oxidation and dissolution of the PSi matrix by the hydroxide ions present in the basic protein solutions [7,177], which competed with the rising response due to the protein adsorption in the pores. This dissolution effect diminished the sensor array response to all three proteins and notably caused the sensor array response to avidin in the pH 10 buffer to be lower than that of avidin in the pH 4 buffer, even though the latter condition was farther from avidin's pI. Importantly, machine learning models can utilize all this information to discriminate between proteins, implicitly taking the complex interplay of adsorption and dissolution effects into account.

To summarize, each protein at each different concentration gave a unique combination of responses to each of the sensor elements in the sensor array, which all had different properties. The resulting fingerprint of the responses for this protein was distinct from that of other proteins. For example, while 2 g/L of BSA gave a very similar response to 2 g/L of avidin when exposed to a sensor etched with 55 mA cm^{-2} in the pH 4 buffer, when the pH 10 buffer was used instead, the BSA response was negligible and the two proteins were easily distinguishable.

Following the optical measurements and Morlet wavelet phase analysis, LDA was used to reduce the dimensionality of the sensor array response matrices from six-dimensional (due to the combination of the three unique formation conditions of the PSi films and two pH values used in the experiments) to three-dimensional, enabling a visualization of the degree to which the three

proteins could be separated. LDA was selected for its ability to maximize the ratio of between-class variance to with-in-class variance [42].

Next, the concentrations of each of the three proteins were classified with several different machine learning algorithms, including support vector machines (SVMs) with linear, radial bias function and sigmoid kernels, random forest, logistic regression, and k nearest neighbor classifiers [166]. Given the labor intensity of the data collection process, the training data set is relatively small for typical machine learning applications.
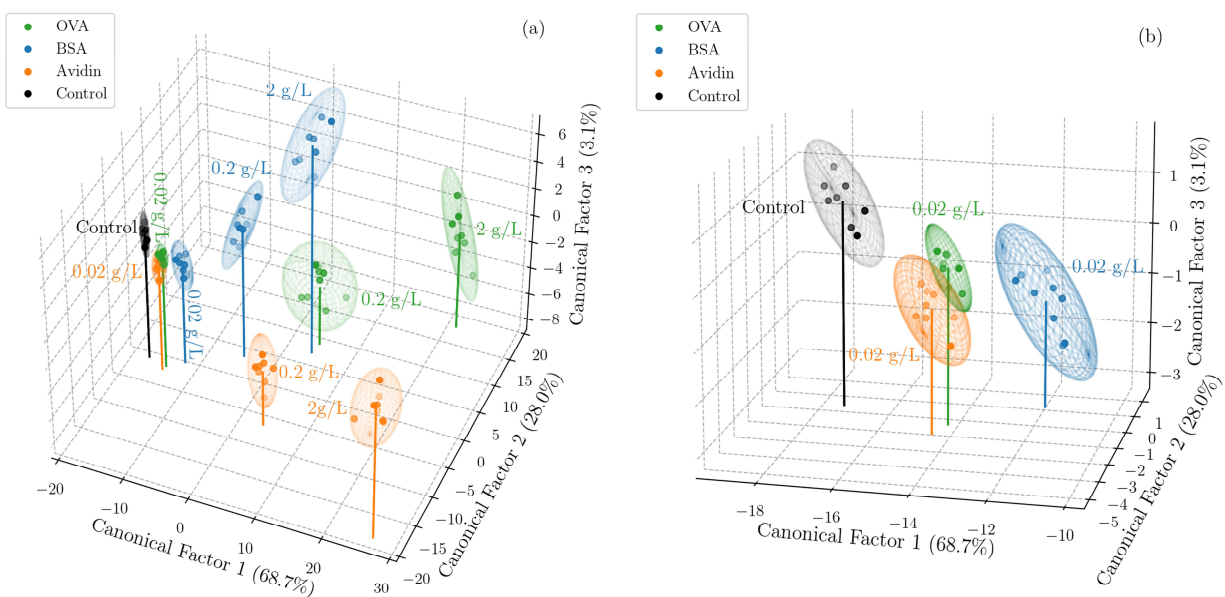
Figure 3.3. Canonical score plot of the three dominant factors obtained from LDA for (a) 3 proteins (OVA, BSA, and avidin) at 3 concentrations (2 g/L, 0.2 g/L, and 0.02 g/L) and a negative control with no protein, and (b) the same 3 proteins at the lowest concentration (0.02 g/L) and a negative control. The ease of classification and quantification of the proteins at the higher concentrations can be observed, as well as the separability at a low concentration.

As a result, to avoid overfitting, no hyperparameter tuning was carried out. Instead, hyperparameters were chosen either using prior intuition or estimation of reasonable values. The number of neighbors for k nearest neighbors was trivially chosen to be 7 (1 less than the number of members of each class), the number of trees when training the random forest algorithm was chosen to be 100, and the regularization parameter denoted as 'C' was chosen to be 100 for SVMs (regardless of kernel) and 10 for logistic regression, all informed by the analysis of a small preliminary dataset. A larger dataset would allow for cross validation to tune hyperparameters and provide a better idea of how the algorithms generalize, but the results shown here give an indication of the accuracy that can be achieved, and which algorithms hold more promise.

The accuracy of prediction for each of the machine learning algorithms investigated was compared when applied to the original 6D dataset and to the 3D reduced dimensionality datasets generated using PCA or LDA. Four scenarios were explored. Firstly, leave one out cross validation was used to indicate the accuracy with which models are able to predict both concentration and type of protein when both have been seen before in the training dataset. This scenario was carried out with both randomly sampled pairwise averaging (Figure 3.4 (a)) and no averaging (Figure 3.4 (b)). Secondly, to test the ability of the model to classify unseen concentrations, the same machine learning models were retrained to classify the protein type only, and a test set was compiled by carrying out further experiments, in which sixteen sensor arrays were exposed to OVA at a new concentration of 0.1 g/L. accuracy of predictions of protein type for an independent test set collected using an intermediate concentration, which was not used to train the models, was examined. This choice of protein and concentration was made to rigorously test the system. It was clear that avidin could be trivially classified due to the large differential effect of pH, whereas in

the training dataset (Figure 3.3), OVA and BSA were less easily discriminable, particularly at low concentrations. Again, this scenario was carried out with both pairwise averaged (Figure 3.4 (c)) and non-averaged data (Figure 3.4 (d)). To prevent data leakage, the mean and standard deviation of the training set were used to standardize both the training and test set. Similarly, the PCA and LDA analyses were applied to the training data, and the test dataset was transformed by the resulting principal components or linear discriminants. For leave one out cross validation, the test set refers to the one data point left out of the training set and on which predictions are made.

Typically, dimensionality reduction techniques are used as a preprocessing step to reduce the complexity and computational burden of training a model, or to visualize high dimensional data (Figure 3.3). However, another advantage of dimensionality reduction can be to reduce noise while retaining maximum signal, which can lead to higher accuracy predictions, as seen in Figure 3.4. Generally, using LDA as a preprocessing step increases accuracy compared to training models on the original dataset. On the other hand, using PCA can be seen to lower accuracy, suggesting the signal to noise ratio is being deteriorated and useful information is being lost, causing models to underfit the data; with a larger dataset, cross validation could be used to examine whether retaining different numbers of principle components could yield higher accuracy classification.

We note that, while the third canonical factor in Figure 3.3 represented a small percentage of the discriminatory power (3.1%), it played a critical role in separating BSA and OVA, which have a similar pI but different molecular weights, and almost identical trajectories when projected only onto the first two canonical factors. Consequently, the third canonical factor has a large contribution to the accuracy of models trained on the dimensionality reduced training set. As a result, the discriminatory power was not the best indicator of feature importance in the context of

discriminating proteins, which was partly a consequence of investigating different concentrations of each target molecule.

The accuracy of many of the algorithms shown in Figure 3.4 drops dramatically when applied to unseen concentrations, compared to concentrations that were present in the training dataset. The source of this instability can be found in Figure 3.3, namely the unique trajectories followed by each of the proteins when varying concentration. An unseen concentration should be classified according to the closest protein trajectory, rather than the protein cluster within the smallest Euclidian distance, which is explicitly the case for k nearest neighbors resulting in severe reduction in classification accuracy. Similar logic applies to the thresholds given by random forest classification as well as support vector machines with radial bias function and polynomial kernels: these models are overfitting and placing too much emphasis on proximity to individual clusters rather than protein concentration trajectories. It is possible regularization or instilling information about the trajectory of each protein would improve these models and lead to more accurate predictions. Conversely, SVM with linear kernel or sigmoidal kernel, and logistic regression do much better at avoiding overfitting and capturing information about the trajectories of each protein, resulting in higher accuracy.

The effect of averaging multiple independent repeated measurements is twofold. Firstly, when classifying concentrations previously seen in the training dataset, pairwise averaging almost always increases accuracy. Since variance of the data is reduced, each class is clustered more tightly and is consequently easier to discriminate.

(a) **Previously Seen Concentration:**
Pairwise Averaging

Machine Learning Algorithm		Original Dimensionality	PCA	LDA
	Linear Kernel	98%	98%	100%
	RBF Kernel	94%	96%	98%
SVM	Sigmoidal Kernel	55%	50%	51%
	Polynomial Kernel	98%	93%	99%
Random Forest		98%	88%	94%
Logistic Regression		96%	94%	90%
K Nearest Neighbors		93%	94%	93%

(b) **Previously Seen Concentration:**
No Averaging

Machine Learning Algorithm		Original Dimensionality	PCA	LDA
	Linear Kernel	91%	89%	90%
	RBF Kernel	91%	80%	94%
SVM	Sigmoidal Kernel	55%	43%	46%
	Polynomial Kernel	90%	80%	91%
Random Forest		91%	79%	91%
Logistic Regression		88%	90%	86%
K Nearest Neighbors		83%	80%	91%

(c) **Previously Unseen Concentration:**
Pairwise Averaging

Machine Learning Algorithm		Original Dimensionality	PCA	LDA
	Linear Kernel	75%	13%	88%
	RBF Kernel	0%	0%	0%
SVM	Sigmoidal Kernel	100%	88%	100%
	Polynomial Kernel	0%	0%	38%
Random Forest		0%	0%	38%
Logistic Regression		88%	100%	88%
K Nearest Neighbors		0%	0%	25%

(d) **Previously Unseen Concentration:**
No Averaging

Machine Learning Algorithm		Original Dimensionality	PCA	LDA
	Linear Kernel	100%	0%	100%
	RBF Kernel	0%	0%	0%
SVM	Sigmoidal Kernel	100%	25%	100%
	Polynomial Kernel	0%	0%	50%
Random Forest		0%	0%	63%
Logistic Regression		100%	50%	100%
K Nearest Neighbors		0%	0%	38%

Figure 3.4. Accuracy of a selection of models trained on the original and reduced dimensionality datasets, when (a,b) classifying and quantifying concentrations previously seen in the training set using leave one out cross validation and (c, d) classifying an independent test set obtained using a concentration previously unseen in the training set. The effect of averaging two randomly sampled data points on accuracy (a, c) is compared to the case of no averaging (b, d)

However, the opposite is true for previously unseen concentration in the independent test set: training on the higher variance unaveraged data will lead to a more conservative model, with looser decision boundaries, which will be more generalizable to data not seen in the training set. In other words, pairwise averaging overfits to the proteins and concentrations the models have

seen before, reducing model robustness. The exception to this rationale is when PCA is used as a preprocessing step. In this case, since the result is already leading to models underfitting the data, the lower variance from pairwise averaging increases accuracy.

Overall, the best performance machine learning pipelines was obtained using pairwise averaging, preprocessing the data with LDA, and then applying SVM with a linear kernel, giving an accuracy of 100% for previously seen protein concentrations, and 87.5% for previously unseen concentrations (one protein was misclassified of the eight in the independent test set), illustrating the promise of this approach for classifying proteins of an unknown concentration. The accuracy of the classification for all models (Figure 3.4), could be increased with a larger array incorporating more pore sizes and pH values to give more discriminating power. Additionally, because no cross validation for the model selection or hyperparameter tuning was carried out due to the limited amount of data, the accuracies reported here are a lower bound of what could be achieved with more data and a more complex optimized model. To investigate the capability of this new approach to sensing without capture agents in more complex sensing scenarios, including detecting target molecules in biologically relevant media, future work will explore increasing the size of the sensing array to encompass additional degrees of freedom (e.g., including the ionic strength of analyte solution, surface charge and hydrophobicity, and the real-time optical monitoring of adsorption and diffusion). It is anticipated that this larger array would be able to distinguish between a larger number of proteins and other species of interest. Given that the average pore size of PSi is tunable in the range from <2 nm to >100 nm [7], the sensing array is potentially applicable to a wide range of molecules with a size of ≤ 100 nm. Moreover, the detection limits of the sensing array can be improved simply by reducing the size of the individual PSi sensor elements while

maintaining the same volume of solution, increasing the number of molecules per unit area, and, consequently, the magnitude of the spectral shift. Finally, we note that a scalable and cost-effective smartphone-based imaging approach to measuring the optical signals [178] could be implemented, enabling the response of an almost arbitrarily large array of PSi sensors to be captured as a function of time.

3.4 Summary

We report the first demonstration of a new approach to molecular identification and quantification based on an array of porous silicon sensors, each with a unique combination of properties but no functionalization or capture agents. This system was able to classify and quantify three proteins separately with a similar molecular size down to concentrations of ~300 nM using optical reflectance measurements and machine learning analysis. An accuracy of 100% was achieved for the proteins and concentrations previously encountered in the training set, and a previously unseen independent test set collected using an intermediate concentration of one of the proteins was classified with 87.5% accuracy. The design of this system could obviate the need for capture agents, paving the way for cheaper, more robust, and quicker-to-develop sensors that provide medical diagnostics, environmental monitoring, and food safety systems to resource-limited environments.

CHAPTER 4

Sensor Response Time Reduction using Long-Short Term Memory Network Forecasting

Parts of this chapter are adapted from "Reduction in Sensor Response Time using Long Short-Term Memory Network Forecasting" published in SPIE Proceedings and reproduced with permission from publisher.

4.1 Introduction

Detecting a target molecule quickly is crucial for a wide variety of safety critical sensing applications, spanning biosensing and chemical sensing. A faster turn-around time for medical diagnostic test results can improve patient outcomes [24,25,94,179–181], swifter warning of toxins in food or the environment can prevent harm to human health or wider ecosystems [182–186], and the sooner hazardous gases can be identified the more effectively preventative action can protect people, assets, and equipment [187–189]. However, rapid sensor response times can be inhibited by diffusion and advection as well as binding kinetics, all of which dictate the time it takes for the sensor to reach equilibrium [64,170,190]. There are several strategies for improvement of sensor response times, ranging from optimizing sensor architecture to achieve a more direct and less tortuous path from the bulk analyte solution to the sensing element or otherwise speed up the sensing mechanism [191–198], to introducing pumps to increase the analyte flow rate [64,170]. However, a much simpler and more cost-effective approach is to use

machine learning to predict the ultimate equilibrium state of the sensor based on initial time series response measurements collected over a much shorter timescale. This method requires no change in sensor design or additional components to achieve a higher flow rate, and it can be applied in parallel to such improvements for further gain in response-time reduction. Moreover, machine learning enabled time series forecasting for response time reduction is potentially applicable to a plethora of different systems focused on detecting either biological or chemical analytes, ranging from accurate, large and expensive benchtop instrumentation to cheap, easy to use and portable devices.

Machine learning and signal processing previously have been used to improve sensor response times by extracting features that provide a more expedient measure of sensor response [199–204], fitting analytical expressions to the incoming time series data [205,206], or predicting sensor response either dynamically based on the data available or by using a fixed or sliding window [207–210]. Often filtering is applied in conjunction with these strategies to provide a more stable prediction [200,202,203,205]. However, there are several drawbacks to these approaches. Firstly, they are often sensor-platform specific and require prior knowledge of the shape and form of the sensor response, either an analytical expression to approximate the time-evolution of the response or features that are characteristic of a given sensor architecture and system design. This prerequisite knowledge limits generalizability of the approach since it may not be portable between different sensor types or even across the same sensor platform. Secondly, noise susceptibility is a pervasive challenge, particularly for deconvolution algorithms which amplify noise [205]. Thirdly, in many previous relevant studies, dataset size is limited [199,204,205,207,208], sometimes consisting of less than 15 experiments because they are

expensive to perform, which makes it hard to claim generalizability. Additionally, uncertainty quantification, widely considered an important part of predictive modeling and, consequently, commonly incorporated across many fields [211], has not, to our knowledge, previously been considered in other work aiming to make predictions to decrease sensor response time. Finally, there has been little application of these techniques to biosensing. Almost all prior work focuses on gas sensing applications despite the fact that the response time of biosensors is typically more than one order of magnitude slower than gas sensors. This is due to lower diffusion coefficients for biomolecules, which are three orders of magnitude larger than gas molecules and are usually immersed in complex solution with many other constituent molecules, and thus biosensors have more to be gained by computationally reducing response time.

In this chapter, we introduce a machine learning-based approach, incorporating an ensemble of long short-term memory (LSTM) networks to accurately predict the final response of biosensors by a mean factor of 18.6x and median factor of 5.1x faster than the timescale of molecular attachment and capture. Importantly, this approach also provides an associated uncertainty of the predicted response. To estimate uncertainty, we followed the approach of aggregating probabilistic outputs of an ensemble of models as detailed elsewhere [212], due to its simple, scalable, well calibrated and high accuracy uncertainty estimation capabilities. Predictions are made dynamically at each time step from real-time measurements. Accordingly, the time taken to return the final result is variable based on prediction uncertainty and stability so the user is never waiting longer than necessary. If the uncertainty of the predicted response is unacceptably high, the test run-time can be extended until confidence in the predicted result improves sufficiently, or the test is concluded invalid. This data driven approach has the key advantage of portability

between sensor platforms and generalizability within a given sensing system because LSTM networks can learn (1) features from data rather than requiring manual feature engineering, (2) the distribution of response curve shape as a function of concentration without theoretical approximations, and (3) how to best distinguish signal from noise.

To demonstrate the utility of this approach leveraging ensembles of LSTM networks, we elected to use porous silicon (PSi) optical biosensors, a well-established sensing platform which has found success in applications including detection of DNA [213,214], glucose [215], bacteria [216] and other biological molecules [13,62]. While PSi has many advantages for biosensing, including tunable pore size and morphology, inexpensive and straightforward fabrication of thin film structures, and large internal surface area presenting a multitude of binding sites for biomolecule adsorption, mass transport is a formidable challenge for PSi biosensors [64–66]. Hence, demonstrating a method for reducing the response times of PSi biosensors could facilitate the use of PSi biosensors for point-of-care diagnostic devices.

4.2 Methods

4.2.1 Materials

All chemicals were of analytical grade and were used without further purification. Boron doped, single side polished, silicon wafers (⟨100⟩, 0.01−0.02 Ω cm) 100 mm in diameter and 500−550 μm thickness, purchased from Pure Wafer, were used to fabricate PSi thin films. De-ionized (DI) water with a resistivity of 15 MΩ cm from a Millipore Elix water purification system was used to wash equipment and samples. HEPES buffer was acquired from Sigma-Aldrich,

ethanol and BSA were obtained from Thermo Fisher Scientific, and aqueous hydrofluoric acid (HF) (48-51%) was purchased from Acros Organics.

4.2.2 Single Layer PSi Biosensor Fabrication

Single layer PSi thin films were fabricated via electrochemical etching of p-type silicon wafers immersed in a HF electrolyte using a platinum mesh cathode, described in detail elsewhere [7,217]. An Advanced Micromachining Tools (AMMT) MPSB etching system was used for wafer scale PSi etching. First a sacrificial layer was etched using a current density of 60 mA cm^{-2} for 100 s, and then removed through dissolution in 0.1 M aqueous NaOH mixed with ethanol in a ratio 1:4, in order to control surface pore size and remove any surface contaminants. The wafer was washed with ethanol, dried under nitrogen stream, and subsequently etched again using the same conditions as for the sacrificial layer: 60 mA·cm^{-2} for 100 s. The resulting PSi layer had an average pore size of 18 nm, and was 3.63 µm thick, as determined by scanning electron microscopy (SEM) and both top view and cross sectional image analysis [217]. The etched wafer was thermally oxidized in a Lindberg/Blue M box furnace at 800°C for 10 min to passivate the surface forming a layer of SiO_2, which increases stability, is less prone to corrosion, and is hydrophilic to allow analyte solution to fill the pores and promote infiltration of the target molecule into the pores. Finally, the wafer was diced into 8×8 mm^2 square samples using a DISCO DAD3220 dicing saw.

4.2.3 Optical Reflectance Measurements

Broadband white light from a Thorlabs SLS201L tungsten-halogen light source was coupled into one arm of a bifurcated optical fiber and focused to a spot size 5 mm in diameter onto each PSi biosensor using an Olympus SPlan 10x microscope lens. Reflected light was collected

by the other arm of the bifurcated fiber and coupled into an Ocean Optics USB4000 spectrometer connected via USB to a PC running Ocean Insight Ocean Direct software. The average of 300 consecutive spectra were collected using an integration time of 3.8 ms, resulting in a total measurement time of 1.14 s.

4.2.4 PSi Reflectance Spectra

Because the nanoscale pores comprising PSi are typically smaller than the shortest visible wavelengths of light used for measurement, PSi can often be considered an effective medium described by a single refractive index. The reflectance spectra of PSi single layer thin films contain approximately sinusoidal Fabry-Pérot interference fringes, which are equally spaced as a function of wavenumber, the inverse of wavelength. The frequency of the Fabry-Pérot fringes is equal to the effective optical thickness (EOT) of the thin film, 2nL, where n is the effective refractive index and L is the physical thickness of the film. As molecules infiltrate and adsorb inside the PSi layer, the volume fraction of air decreases, as it is replaced by higher refractive index biological material, increasing the effective refractive index and, accordingly, EOT of the PSi layer. The corresponding increase in frequency of the fringes can be quantified using the fast Fourier transform (FFT)-based reflective interferometric Fourier transform spectroscopy (RIFTS) method [77].

4.2.5 Real-Time Sensor Response Data Collection

A large experimental throughput is necessary to enable collection of sufficiently large datasets to allow analysis by machine learning algorithms. Typically, real time optical measurements of PSi are collected one sensor at a time in a single channel fluidic cell, or occasionally a fluidic cell with multiple channels has been used to measure a few (<5) locations on a PSi sensor [218,219]. However, in order to increase experimental throughput by many orders

of magnitude, we present the novel design of a multiplexed fluidic cell (Figure 4.1 (a)) accommodating a large number of PSi sensors which are measured in an automated and sequential manner using an addressable stepper motor to incrementally step between samples. The multi-channel fluidic cell was designed to house up to one hundred individual 8×8 mm^2 PSi biosensors. The fluidic cell consisted of two plexiglass sheets 3.175 mm thick, laser-cut into disks 260 mm in diameter with several screw holes to hold the sheets together, and guide holes to align them correctly. An inlet and outlet for each channel of the fluidic cell were also laser-cut to have a diameter of 1 mm. For each channel, the silicon substrate side of a PSi sample was secured to the lower plexiglass sheet using double sided scotch tape. O-rings 8 mm in diameter and with 1 mm thickness were placed over each PSi sensor. The upper plexiglass sheet was then guided onto the lower assembly, ensuring all o-rings lay within the boundaries of each PSi sensor and encompassed both the inlet and outlet of the upper plexiglass sheet to create an effective seal. Once secured with screws, the multi-channel fluidic cell was affixed to a Polulu 1206 stepper motor using the mounting hub. Python code was used automate and schedule both the setting of stepper motor position via the Tic T500 USB stepper motor controller board and yaml library, and processing and saving reflectance spectra using the Ocean Direct API. We note that it is imperative for the stepper motor to return to the same position with high accuracy for every sensor to prevent any non-uniformity of PSi film optical thickness from introducing error into the measurements; however, we found that even an inexpensive, low resolution stepper motor was able to return to the same position with micron precision, which provided sufficient repeatability and negligible error. To the best of our knowledge, this is the first experimental protocol in which real-time measurements of numerous PSi sensors are collected in parallel.

4.2.6 Experimental Procedure

Thirty PSi samples from an etched and diced wafer were washed using ethanol and dried under nitrogen stream before being secured into the multichannel fluidic cell. We note that the total capacity of the fluidic cell was 100 sensors, but there is a tradeoff between the time taken for each measurement in addition to the time to step between sensors, and the time resolution of consecutive measurements. Further speed optimizations would further increase experimental throughput. A dark spectrum corresponding to 0% reflectance measured without illumination from the light source and a reference spectrum indicating 100% reflectance measured with an unprotected gold mirror were collected to calibrate the reflectance measurements. A vial of 200 µL of BSA solution was prepared at one of 13 different concentrations: 40 mg/mL, 20 mg/mL, 10 mg/mL, 4 mg/mL, 2 mg/mL, 1 mg/mL, 0.4 mg/mL, 0.2 mg/mL, 0.1 mg/mL, 0.04 mg/mL, 0.02 mg/L, 0.002 mg/mL, and a control solution consisting of 100% HEPES buffer. The optimum stepper motor positions, as close as possible to the center of each PSi sample, were determined and hard coded into the python control software. The measurement cycle was initiated, which first measured each sensor in turn before application of analyte solution. On the second rotation, the control software paused for an additional 10s over every PSi sensor channel to allow the injection of 25 µL protein solution into the inlet of each fluidic channel in turn. Subsequent measurement loops continued for 250 measurements of each sensor, equivalent to an experiment length of 13 hours. The entire measurement setup, including optical fiber, reflectance probe, stepper motor and multi-channel fluidic cell were encased in an airtight container, with a beaker of water also enclosed to maintain a high humidity locally, which prevented BSA solution evaporation over the extended experiment runtime.

The time series of reflectance spectra for each PSi sensor were analyzed using the RIFTS method, and normalized according to the following equation: $\frac{EOT_n - EOT_0}{EOT_0}$, where EOT_0 and EOT_n are the effective optical thicknesses of the PSi at the first timestep and the nth timestep, respectively. In total, the dataset consisted of 387 experimental sensor response examples spread across the 13 concentrations.

4.2.7 Uncertainty Quantification

Of the numerous ways to quantify uncertainty associated with machine learning model predictions, including Bayesian neural networks [220] and Markov chain Monte Carlo (MCMC) [221], we follow the methodology outlined in Ref 211, to estimate uncertainty of the predictions. This work established that a particularly simple, scalable and effective way of estimating uncertainty for deep neural networks is to assume the output of the network is normally distributed, parameterized by predicted mean (μ) and variance (σ^2) which are captured by two nodes in the output layer. An ensemble of such neural networks were each individually trained by minimizing the negative log likelihood, and the mean and variance predictions of each of these base learners was aggregated to give a more accurate and better calibrated predicted uncertainty. In this study, these principles were applied to LSTM networks. The predictions of μ and σ^2 were averaged for each of the LSTM network base learners, taking into account both within class and between class variance, yielding a point prediction indicated by mean μ and a measure of uncertainty or prediction spread indicated by variance σ^2.

Rather than varying the architecture of the base learners or bootstrapping the dataset, which significantly reduces the amount of data each model is trained on, the diversity of the base learner

93

predictions is solely a result of random initializations of parameters and randomly reshuffling the data. This approach has been empirically found to give superior performance [212].

4.2.8 Data Analysis

LSTM networks are well suited for the rapid prediction of equilibrium sensor response due to their ability to learn features without requiring manual feature selection, to learn to distinguish signal from noise, and to learn long and short-term dependencies in sequential data, all of which promote generalizability. Models were implemented in TensorFlow using the Keras API [222] and built-in LSTM layers. Each LSTM layer was configured to return a sequence of 250 outputs, one for each input time step. The target output, used to compute the loss, is the final element of each input sequence, repeated in a vector with 250 elements. Each output prediction in the sequence is made having only seen data from the current and past timesteps, so will typically become increasingly more accurate as the sequence goes on and more data from the input sequence is seen by the model. The data was first randomly shuffled and split into train, validation and test sets at a ratio of 3:1:1, stratified by BSA concentration. Ensembles of 15 base learners [223] were trained in turn, by minimizing the negative log likelihood ($-\log p(y|x)$), using softplus activation at the output layer to ensure predictions are positive, and adam optimization [224]. Ensembles were used to increase accuracy and prediction stability, and for better calibrated uncertainty quantification [212,223]. The base learner architecture, informed by limited hyperparameter tuning using the validation set, was the following: 50 input neurons, 1 hidden layer with 500 neurons, and 2 output neurons. The maximum and minimum sensor response values across all time steps and all examples in the training set were used to normalize the train, validation and test sets, to avoid data leakage.

4.3   Results and Discussion

The achievable reduction in response time using the predictions from an ensemble of LSTM networks was investigated using the experimental dataset measured by exposing buffered BSA solutions to PSi biosensors and comparing the initial intrinsic experimental sensor response time to the response time of the model's predictions.

4.3.1   Experimental Dataset

The experimental dataset of real-time optical reflectance measurements collected by exposing BSA in HEPES buffer at one of 13 different concentrations to PSi biosensors is shown in Figure 4.1 (b, c). PSi reflectance spectra are analyzed using the RIFTS method and expressed in terms of the fractional change in EOT, which allows comparison between PSi sensors with slightly different baseline EOT. These variations are due in part to the random sampling of the distribution of pore size and morphology, and small spatial variations in PSi. It is clear from Figure 4.1 (b, c) that even when concentration is held constant there is large variability in equilibrium response, attributed primarily to the highly variable interactions between molecules and the internal PSi surface rather than variation in PSi sensor properties. In Figure 4.1 (b), this is manifested by the range of final equilibrium responses for a single concentration, illustrated by a single color, and in Figure 4.1 (c) this is captured in the sizeable error bars which represent the standard deviation of equilibrium responses at each concentration. We note that in Figure 4.1 (c), the Redlich Peterson adsorption isotherm [176], representing imperfect monolayer adsorption and previously found to best fit the data [78], provides general agreement with the data showing how the equilibrium fractional EOT change depends on BSA concentration. For the purposes of this study, the variation in equilibrium response for a given concentration is not a concern; in fact, it

95

ensures the equilibrium values in the training data are more uniformly distributed. Additionally, the approach of using LSTM networks is generalizable and portable to other higher affinity assays that rely on specific binding, and for which response curves generated using the same concentration of target molecules would be much more closely grouped, circumventing this issue.

While this BSA assay has long response times (mean of 3.95 hours), which even in the context of PSi biosensors and other platforms is relatively slow, the focus of this work was the relative reduction in experimental response time that predictions from LSTM network ensembles can provide, rather than the absolute value. Simple steps to improve response time for this assay, in addition to the predictive time-series modeling approach reported here, include flowing analyte solution across the sensors rather than using a configuration without analyte flow, decreasing the thickness of the PSi films, and increasing the pore size, all of which promote faster mass transport.

Figure 4.1 (b, c) also demonstrates the non-linearity of the complex molecular adsorption and diffusion dynamics of BSA in the pores, leading to a response curve with a shape that depends on concentration, and cannot be accurately fit with a simple analytical expression, which may be in part a consequence of the non-uniformity of the size and morphology of the pores across a given silicon wafer. For BSA concentrations below 0.4 mg/mL, the signal to noise ratio (S/N) is particularly low and there is no systematic difference in the final equilibrium response.
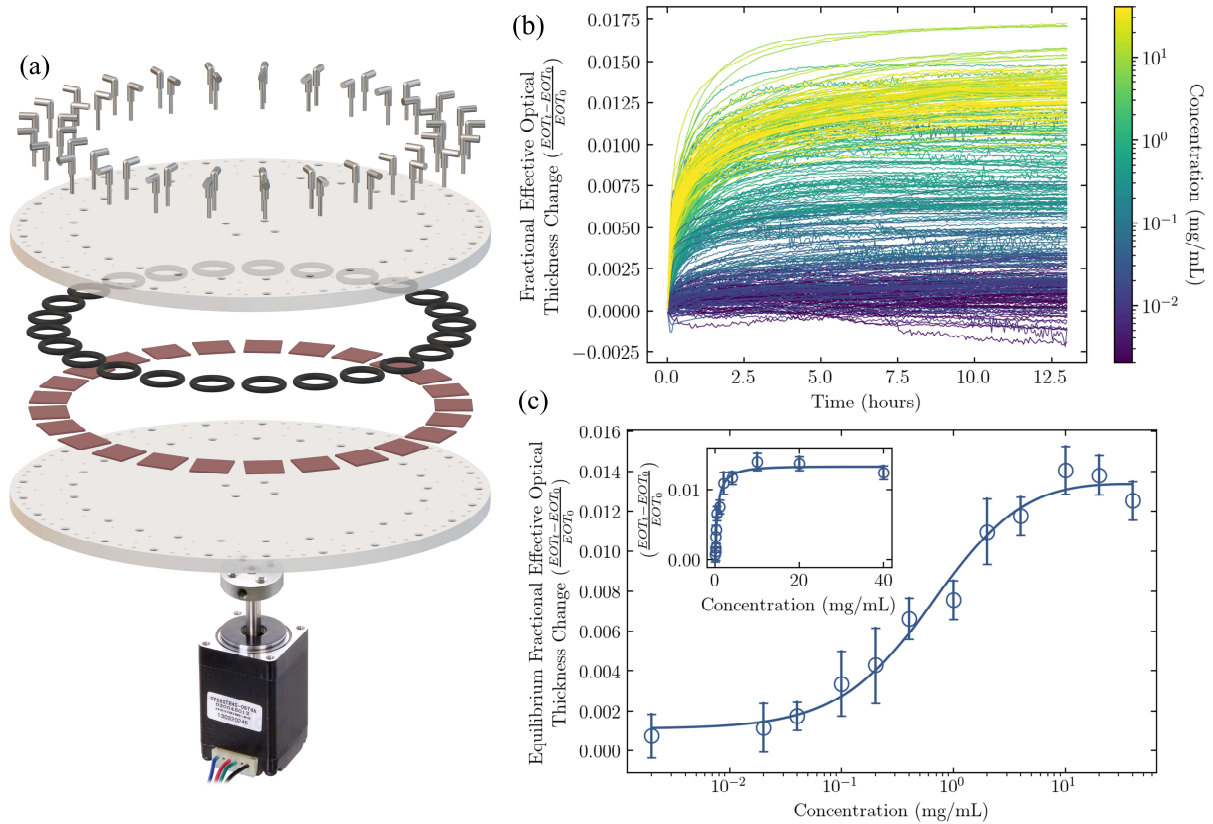
Figure 4.1. Diagram of the multi-channel fluidic cell for high throughput real-time data collected by exposing single layer PSi sensors to solu-tions of BSA in HEPES buffer, including the stepper motor, mounting hub, bottom laser cut plexiglass sheet, PSi sensors, o-rings, top laser cut plexiglass sheet, and inlet and outlet tubing (a). The experimental dataset expressed in terms of the fractional change in EOT, is shown in both (b) the raw temporal sensor response curves, and (c) adsorption isotherm fit with the Redlich Peterson model [176] on a log scale. The inset of (c) shows the same data on a linear scale, and the error bars indicate the standard deviation of between 26 and 40 measurements for a single concentration.

In contrast, for concentrations between 0.2 mg/ml and 2 mg/ml, the equilibrium response is highly correlated with increasing concentration and S/N also rises accordingly. Finally, at concentrations above 10 mg/ml, the equilibrium response plateaus as all adsorption sites in the pores are filled, and the PSi sensors are saturated.

4.3.2 Comparison of Models

While there are a vast number of models that can be applied to time series forecasting problems, many are not well suited for this specific task due to the non-stationary nature of the sensor response data, including autoregressive ARIMA models and Kalman filters. Other algorithms that rely on fewer assumptions about the data including stationarity, such as RNNs and gated recurrent unit (GRU) networks, were investigated alongside LSTM networks, due to their flexibility. As part of the neural network family, they are all universal approximators, and are consequently able to learn features and relationships between features rather than requiring feature selection or prior knowledge of an analytical expression to approximate a sensor response.

Figure 4.2 shows the ratio between experimental t90 times and t90 times of predictions from LSTM, RNN and GRU models, which equates to the factor of improvement that predictions from these models afford, as a function of concentration. As can be observed, for LSTM, GRU, and RNN models, the improvements in response time gained from the model predictions are proportional to the concentration, and by extension the S/N. It is also clear that the LSTM network predictions have a much greater impact on response time than RNNs and GRUs, with a mean and median decrease in response time of up to a factor of 18.5 and 32, respectively, demonstrating the importance of enhanced gradient flow in the network and cell memory to more effectively capture the long- and short-term dependencies in the sensor response kinetics.
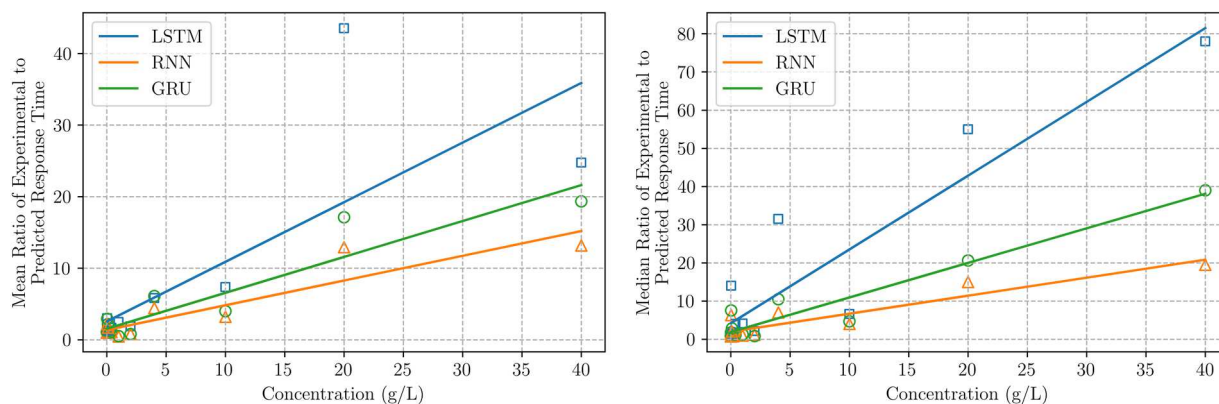
Figure 4.2. Average factor of improvement of response time for predictions from LSTM, RNN, and GRU networks using different concentrations of BSA in HEPES buffer: between 0 g/L (control, no protein) to 40 g/L, reporting a) mean and b) median response time reduction.

The improvements for LSTM, GRU and RNN predictions converge as the concentration of BSA solutions and consequently S/N decreases. This is because the flexibility of maintaining and updating the memory cell, which is supported by the LSTM network, becomes less important as sequential real-time sensor response measurements become less correlated and dominated by noise sources such as small changes in experimental conditions including temperature, humidity, and vibrations, among others.

4.3.3 Evaluation of Model Performance

Several representative examples of sensor response curves from the previously unseen test set alongside the LSTM ensemble model predictions are shown in Figure 4.3. The ideal predictive model response is shown with the dashed line, which initially lies at half the normalized range of sensor responses, and instantaneously jumps to the target equilibrium response, with an infinitesimally small response time. The uncertainty of model predictions is illustrated by the blue shaded regions, spanning two standard deviations on either side of the mean prediction of the ensemble, encompassing 95% of the predicted distribution. The model's predictive ability is

99

shown through the quick convergence to the equilibrium response value–making predictions on relatively few initial time series data points and with low variance–for examples with relatively high S/N (Figure 4.3 (a), (b), and (c)). These high S/N examples are typically obtained using higher concentrations. In other cases, particularly for response curves with low S/N which correlates with low BSA concentration, the model predictions take a lot longer and a lot more time series data to converge, sometimes never stabilizing at the correct equilibrium response (Figure 4.3 (d), (e), and (f)). Noise sources which reduce S/N include drift in temperature, humidity, and precise positioning of the experimental setup, as well as vibrations. While for this work it was advantageous to have a range of S/N examples in the experimental dataset to test the limits of the model, these noise signatures could be drastically reduced when using an assay with antifouling layers and stronger binding affinity. Furthermore, the degraded model performance due to poor S/N was reassuringly accompanied by increased prediction uncertainty indicated by the shaded regions in Figure 4.3. The uncertainty is always initially high as the model is making predictions on a very small number of data points, but in most cases decreases over time as more data is available, the model gains confidence, and predictions become more accurate. When deploying this model, an acceptable threshold of both uncertainty and prediction stability would be chosen; the decision of when to return the test result could then be made dynamically according to when the model output is within these thresholds. This results in a test time that is never longer than necessary, which is not the case when a predetermined fixed window of data is used for prediction.
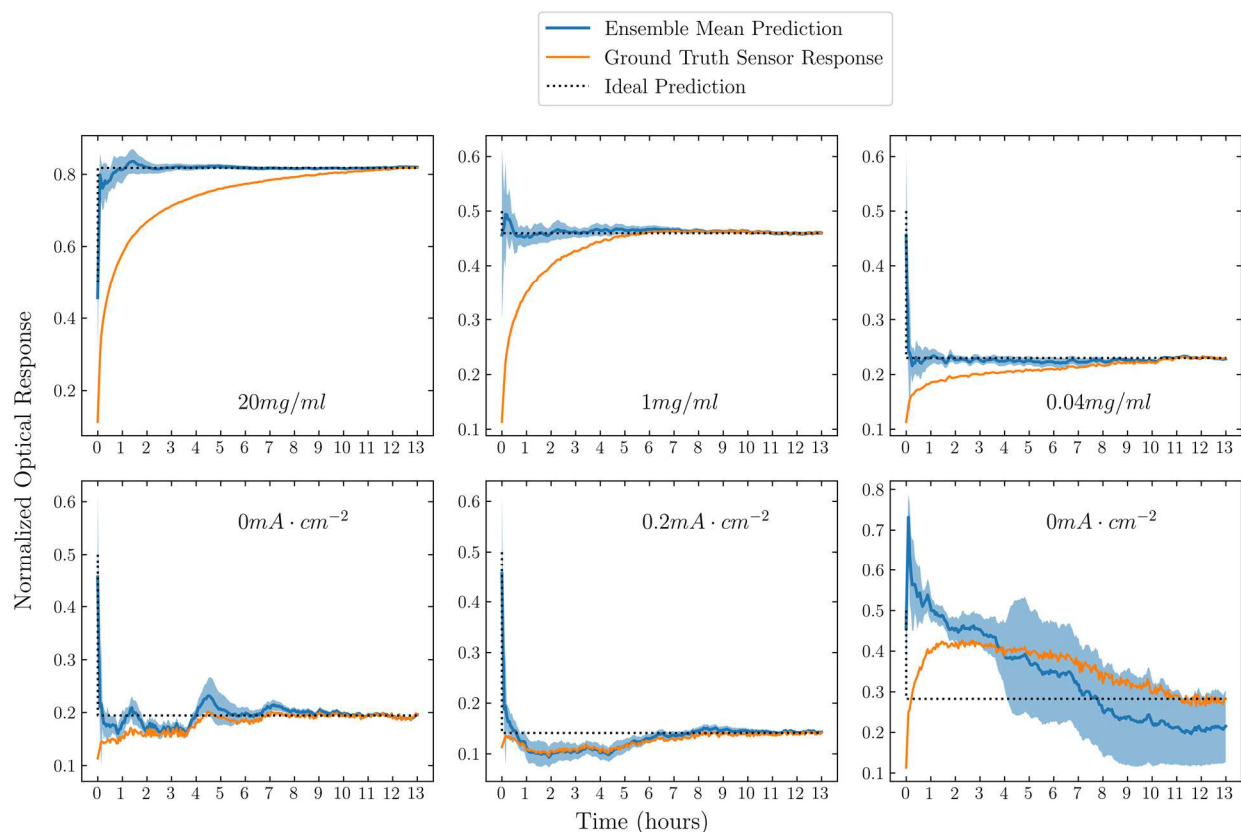
Figure 4.3. Series of examples of PSi biosensor time-series responses from the test dataset (orange) which are previously unseen by the model, and corresponding model predictions (dark blue) at every timestep using only data from the current and all previous timesteps. The shaded blue region is a measure of the predicted variance, or uncertainty, in the equilibrium response prediction, encompassing two standard deviations on either side of the ensemble mean, capturing 95% of the distribution. The black dotted line is the ideal model prediction, which is initially a normalized response of ~0.5 at t=0 when the model has no information about the sensor response, then instantly converges to the equilibrium sensor response.

In order to determine the best size of the ensemble to use for this application, the number of base learners was varied and the accuracy of ensemble predictions was evaluated on the validation dataset, which was not explicitly used during training. The ensemble size chosen was 15 base learners: increasing ensemble size beyond that offered negligible improvement in response time and only served to increase the complexity and computational burden of the model (Figure 4.4).
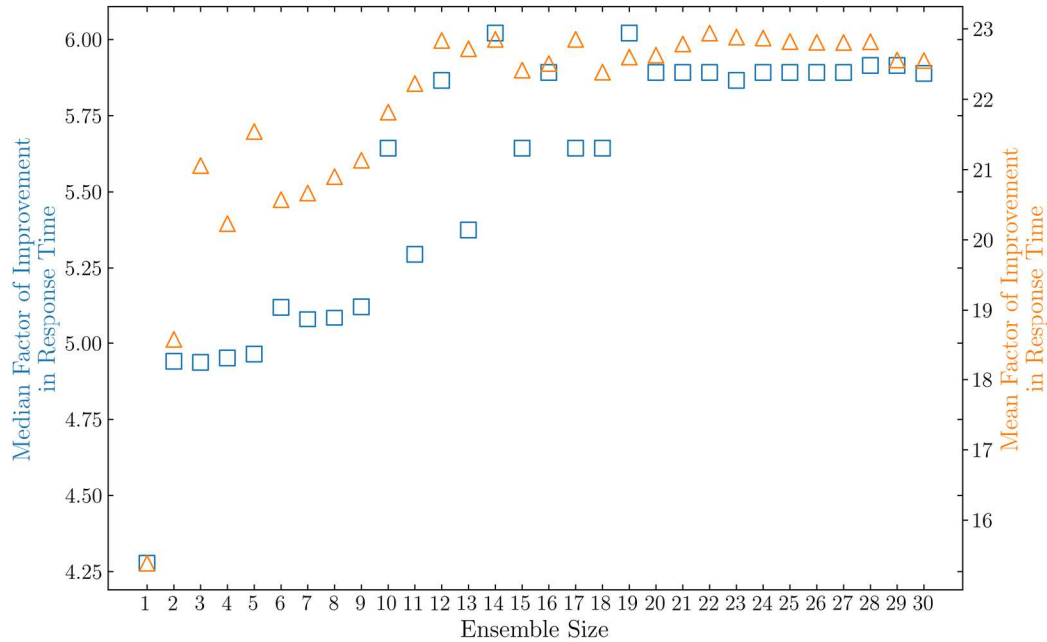
Figure 4.4. Mean and Median factor of improvement in biosensor response time realized when using ensembles composed of different numbers of base learners.

A comparison of the experimental response time and response time resulting from the predictions of an ensemble of 15 LSTM networks is shown in Figure 4.5. The standard measure of the speed of response of a sensor is the t90 time, which is defined as the length of time taken for a sensor response to reach 90% of its ultimate equilibrium value. This definition was slightly modified for this work to account for the possibility of overshooting the equilibrium response, due to low S/N or initial model prediction instability, and became the time for the sensor response to settle within 10% of the final equilibrium value. Specifically, Figure 4.5 (b) shows a histogram illustrating the distribution of t90 response times for the original experimental dataset and the LSTM ensemble model predictions. The improvement in response time afforded by the model predictions is demonstrated through the large shift in the overall distribution to lower response times. However, there are still some prediction-based response times that remain high, which can

be understood with reference to the normalized variance plot in Figure 4.5 (a). The normalized variance for each experimental sensor response curve is $\frac{\overline{(\sigma^2)}}{Response(t=13\ hrs)}$ where $\overline{(\sigma^2)}$ is the average predicted variance, or uncertainty, for every time point in a given sensor response, and Response(t=13 hrs) is the corresponding equilibrium sensor response at the end of the experiment. Normalized variance is therefore a measure of the model's confidence (correlated to S/N); the linearly increasing trend in Figure 4.5 (a) indicates that when the model performed poorly this was accompanied by increased uncertainty. An alternative representation of the distribution of factor of improvement in response time provided by the LSTM network ensemble model is shown in Figure 4.5 (b, c). The ratio of original experimental t90 time to model prediction t90 time is presented in the form of a box and whisker plot, also including the summary statistics reporting the mean and median improvement of 18.6 and 5.1 respectively.

Further improvement in response time could be achieved with larger or augmented dataset. To this end, the utility of finite element method (FEM) modeling [64,65] to provide a physics informed simulated dataset was explored. However, both transfer learning, and a single augmented training dataset containing experimental examples as well as FEM simulations, led to decreased performance rather than higher accuracy. This is likely a consequence of the complexity of the system, which cannot be captured using simulations in a sufficiently accurate, timely, and computationally feasible manner. Additionally, other augmentation strategies such as interpolation could also enhance performance.
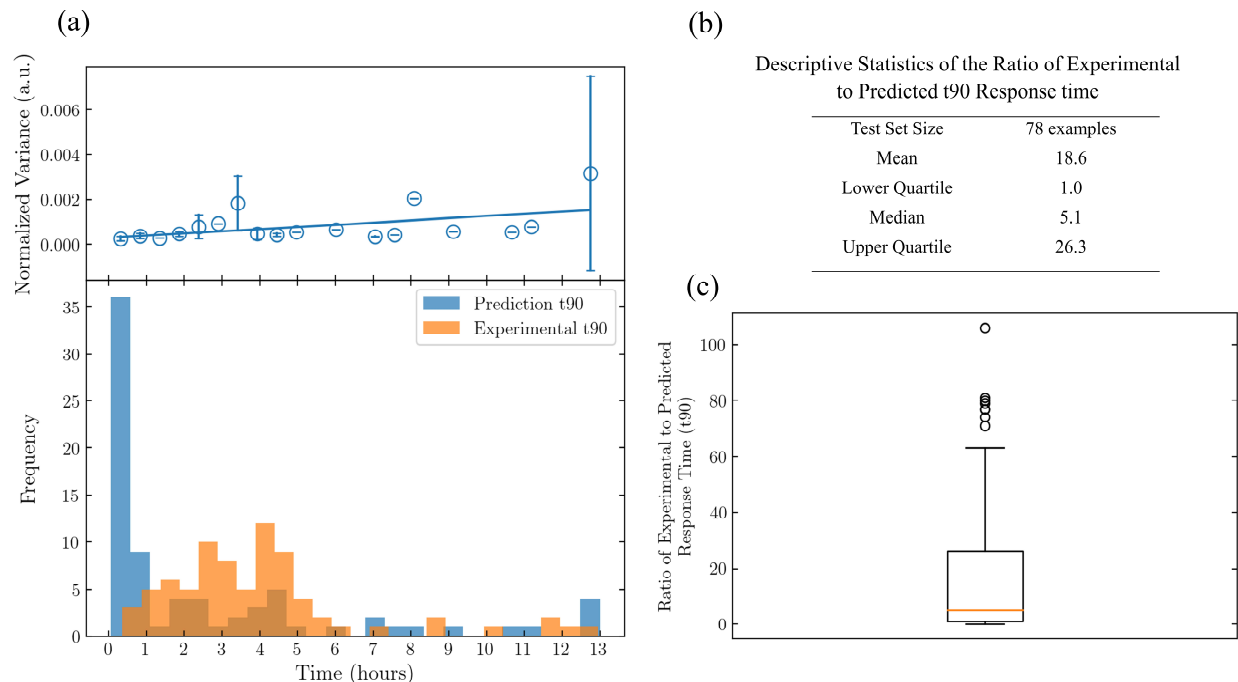
Figure 4.5. Comparison of t90 response times of the unprocessed experimental data and after application of the model comprised of an ensemble of LSTM networks, illustrated by (a) a histogram showing the two distributions of t90 response times, and the ratio of experimental to model prediction t90 response time displayed in the form of (b) descriptive statistics and (c) a box and whisker plot. The higher this ratio, the greater the factor of improvement. Additionally, (a) includes the time averaged predicted variance, or uncertainty, of the ensemble of LSTM networks for each sensor response in each bin of the histogram. This average variance is normalized by the equilibrium value of the sensor response, indicative of S/N.

4.4 Conclusion

In summary, we have demonstrated that ensembles of LSTM networks can reduce biosensor response time by predicting the ultimate equilibrium response, alongside a well calibrated measure of uncertainty, using a small quantity of initial time series sensor response data. The key advantages of the approach presented in this work are: indication of the confidence of the model's predictions which lays a crucial foundation for important safety-related decisions; no requirement for prior domain knowledge of sensor response kinetics or manual feature

engineering; relatively high noise immunity learned by the model; generalizability and portability across different concentrations, systems, and sensor platforms; scalability and high throughput data collection methodology enabling large datasets; and applicability in tandem with other response time reduction strategies. Through application to an experimental dataset collected by carrying out a BSA assay using PSi optical biosensors, for which mass transport and consequently response time is a significant limitation, a mean and median factor of improvement of 18.6 and 5.1 respectively, was realized. For the majority of sensors in the test dataset, the LSTM networks accurately predicted the sensor response in 45 minutes or less while the average experiment required nearly 4 hours to reach the equilibrium response. The demonstrated dramatic reduction in biosensor response time sets the stage for faster medical diagnostics, improving patient outcomes and healthcare access, and earlier warning of toxins and harmful biomolecules in food and the environment.

CHAPTER 6

Conclusions

6.1 Summary

Improving biosensor performance is crucial to meeting the global need for robust, cheap, portable, easy-to-use, and fast-responding point of care tests with low detection limits in the fields of medical diagnostics, environmental monitoring, and food safety, particularly in low resource geographic regions experiencing extreme climates in dire need of such assays. This dissertation demonstrates the value of a diverse range of machine learning, statistical, and signal processing techniques as tools to improve biosensor performance metrics, with a particular focus on lowering limits of detection; increasing robustness while reducing cost and complexity; and faster response times. First, we showed the utility of signal processing techniques to reduce the detection limit of optical biosensors, which is often limited by various noise sources including those introduced by the optical measurement setup. Among the plethora of signal processing pipelines considered, it was found that applying complex Morlet wavelet convolution to Fabry-Pérot interference fringes characteristic of thin film reflectometric biosensors effectively filters out white noise and low frequency reflectance variations. Subsequent calculation of an average difference in extracted phase between the filtered analyte and reference signals enables a significant reduction in the limit of detection. This method was applied on experimental data sets of thin film porous silicon sensors (PSi) in buffered solution and complex media obtained from two different laboratories, to showcase the potential improvement to detection limits afforded by this work. Second, we demonstrated a new biosensing approach to improve robustness to harsh environments; reduce

106

cost, complexity, and development time; and potentially increase biosensor detection coverage dramatically. Typically, biosensors are designed to detect specific analytes through functionalization with the appropriate capture agents. However, the use of capture agents limits the number of analytes that can be simultaneously detected and reduces the robustness of the biosensor. To address these issues we designed a versatile, capture agent free biosensor platform based on an array of porous silicon (PSi) thin films, which has the potential to robustly detect a wide variety of analytes based on their physical and chemical properties in the nanoscale porous media. The ability of this system to reproducibly classify, quantify, and discriminate among three proteins is demonstrated to concentrations down to at least 0.02 mg/mL (between 300 nM and 450 nM) by utilizing PSi array elements with a unique combination of pore size and buffer pH, employing linear discriminant analysis for dimensionality reduction and support vector machines as a classifier. This approach represents a significant step towards a low cost, simple, and robust biosensor platform able to detect a vast range of biomolecules. Finally, we showed how response time of biosensors can be reduced, by using ensembles of long short-term memory networks for time-series forecasting to predict the ultimate steady-state response of a biosensor, the direct measurement of which can require waiting many hours, in a much shorter time. The response time of a biosensor is a crucial metric, particular in safety-critical applications; however, the speed at which a biosensor reaches a final equilibrium state is often limited by poor mass transport and long diffusion times. We showed that the predictions of ensembles of long short-term memory (LSTM) networks from a small quantity of initial time series data allows for a significant reduction in response time by a mean and median factor of improvement of 18.6 and 5.1, respectively. The ensemble of models also provides simultaneous estimation of uncertainty, which is vital if any

107

confidence is to be placed in the predictions and urgent safety-related decisions are to be made on that basis. This approach is demonstrated on real-time experimental data collected by exposing porous silicon biosensors to buffered protein solutions using a multi-channel fluidic cell designed to expand experimental throughput. The dramatic improvement in sensor response time achieved using LSTM network ensembles and associated uncertainty quantification opens the door to trustworthy and faster responding biosensors, enabling rapid medical diagnostics for improved patient outcomes and healthcare access, or quicker identification of toxins in food or the environment.

6.2 Outlook and future avenues

The exploration of applying machine learning to biosensor data, with the objective of enhancing performance metrics to expand the application space of current and future technology, is arguably still in its infancy. There exists a vast reservoir of untapped potential in this domain. This dissertation seeks to elucidate several ways in which machine learning can address and potentially overcome significant obstacles hindering the widespread commercialization and adoption of biosensors, and provide solutions to the most pressing problems in the fields of medical diagnostics, food safety, and environmental monitoring.

It is evident that the insights presented in this dissertation only scratch the surface, aiming to inspire further ideas on how machine learning can creatively enhance biosensor technologies in terms of specificity, sensitivity, stability, and response time, by leveraging algorithms for regression, classification, clustering, dimensionality reduction, and potentially even reinforcement learning.

108

A major challenge in applying machine learning to biosensors lies in the expensive data collection process. Although strides have been made in this dissertation to address this issue, it is anticipated that incorporating smartphones for optical measurements, rather than relying solely on spectrometers, could result in orders of magnitude growth in dataset size. Unlike spectrometers, smartphones enable the parallel measurement of an almost arbitrarily large number of sensors, limited only by the number of pixels in the smartphone image, among other advantages such as cost and form factor. The ultimate vision is a machine learning enabled quantitative, sensitive, specific, fast responding, inexpensive, and portable "lab on a chip", compatible with a smartphone for measurement, inference, and interface to display test results. Such systems hold the potential to democratize high-quality medical diagnostic, food safety, and environmental monitoring tests, making them accessible anywhere and administered by anyone, with significantly benefit to society.

REFERENCES

1.   S. Rodriguez-Mozaz, M. J. L. De Alda, M. P. Marco, and D. Barceló, "Biosensors for environmental monitoring: A global perspective," Talanta **65**, 291–297 (2005).

2.   V. Scognamiglio, F. Arduini, G. Palleschi, and G. Rea, "Biosensing technology for sustainable food safety," TrAC - Trends Anal. Chem. **62**, 1–10 (2014).

3.   T. Vo-Dinh and B. Cullum, "Biosensors and biochips: Advances in biological and medical diagnostics," Fresenius. J. Anal. Chem. **366**, 540–551 (2000).

4.   A. K. Yetisen, M. S. Akram, and C. R. Lowe, "Paper-based microfluidic point-of-care diagnostic devices," Lab Chip **13**, 2210–2251 (2013).

5.   M. N. Velasco-Garcia and T. Mottram, "Biosensor technology addressing agricultural problems," Biosyst. Eng. **84**, 1–12 (2003).

6.   D. Griffiths and G. Hall, "Biosensors - what real progress is being made?," Trends Biotechnol. **11**, 122–130 (1993).

7.   M. J. Sailor, *Porous Silicon in Practice: Preparation, Characterization and Applications*, 1st ed. (Wiley-VCH, 2012).

8.   M. Holzinger, A. Le Goff, and S. Cosnier, "Nanomaterials for biosensing applications: A review," Front. Chem. **2**, 1–10 (2014).

9.   C. Fenzl, T. Hirsch, and O. S. Wolfbeis, "Photonic crystals for chemical sensing and biosensing," Angew. Chemie Int. Ed. **53**, 3318–3335 (2014).

10.   S. Vigneshvar, C. C. Sudhakumari, B. Senthilkumaran, and H. Prakash, "Recent advances in biosensor technology for potential applications - an overview," Front. Bioeng. Biotechnol. **4**, 1–9 (2016).

11.	K. Urmann, E. Tenenbaum, J.-G. Walter, and E. Segal, "Porous Silicon Biosensors Employing Emerging Capture Probes," in *Electrochemically Engineered Nanoporous Materials*, A. Santos and D. Losic, eds. (Springer, 2015), pp. 93–116.

12.	S. Mittal, H. Kaur, N. Gautam, and A. K. Mantha, "Biosensors for breast cancer diagnosis: A review of bioreceptors, biotransducers and signal amplification strategies," Biosens. Bioelectron. **88**, 217–231 (2017).

13.	V. S. Y. Lin, K. Motesharei, K. P. S. Dancil, M. J. Sailor, and M. R. Ghadiri, "A porous silicon-based optical interferometric biosensor," Science (80-.). **278**, 840–843 (1997).

14.	V. Naresh and N. Lee, "A Review on Biosensors and Recent Development of Nanostructured Materials-Enabled Biosensors," Sensors **21**, 1109 (2021).

15.	D. Grieshaber, R. MacKenzie, J. Vörös, and E. Reimhult, "Electrochemical Biosensors - Sensor Principles and Architectures," Sensors **8**, 1400–1458 (2008).

16.	P. Damborský, J. Švitel, and J. Katrlík, "Optical Biosensors," Essays Biochem. **60**, 91–100 (2016).

17.	K. Ramanathan and B. Danielsson, "Principles and Applications of Thermal Biosensors," Biosens. Bioelectron. **16**, 417–423 (2001).

18.	I. Voiculescu and A. N. Nordin, "Acoustic wave based MEMS devices for biosensing applications," Biosens. Bioelectron. **33**, 1–9 (2012).

19.	F. Calderón-Celis, J. R. Encinar, and A. Sanz-Medel, "Standardization approaches in absolute quantitative proteomics with mass spectrometry," Mass Spectrom. Rev. **37**, 715–737 (2018).

20.	J. W. F. Law, N. S. A. Mutalib, K. G. Chan, and L. H. Lee, "Rapid methods for the detection

of foodborne bacterial pathogens: Principles, applications, advantages and limitations," Front. Microbiol. **5**, 1–19 (2014).

21.   D. W. Kim, "Real time quantitative PCR," Exp. Mol. Med. **33**, 101–109 (2001).

22.   S. Aydin, "A short history, principles, and types of ELISA, and our laboratory experience with peptide/protein analyses using ELISA," Peptides **72**, 4–15 (2015).

23.   B. Domon and R. Aebersold, "Mass spectrometry and protein analysis," Science (80-.). **312**, 212–217 (2006).

24.   V. Gubala, L. F. Harris, A. J. Ricco, M. X. Tan, and D. E. Williams, "Point of care diagnostics: Status and future," Anal. Chem. **84**, 487–515 (2012).

25.   H. Chen, K. Liu, Z. Li, and P. Wang, "Point of care testing for infectious diseases," Clin. Chim. Acta **493**, 138–147 (2019).

26.   C. P. Price, "Point of care testing," Br. Med. J. **322**, 1285–1288 (2001).

27.   A. J. Singer, J. Ardise, J. Gulla, and J. Cangro, "Point-of-care testing reduces length of stay in emergency department chest pain patients," Ann. Emerg. Med. **45**, 587–591 (2005).

28.   S. F. Clarke and J. R. Foster, "A history of blood glucose meters and their role in self-monitoring of diabetes mellitus," Br. J. Biomed. Sci. **69**, 83–93 (2012).

29.   J. Hu, S. Q. Wang, L. Wang, F. Li, B. Pingguan-Murphy, T. J. Lu, and F. Xu, "Advances in paper-based point-of-care diagnostics," Biosens. Bioelectron. **54**, 585–597 (2014).

30.   P. Patel, "Paper Diagnostic Tests Could Save Thousands of Lives," Sci. Am. (2016).

31.   S. Kemp, "Digital 2021: Global Overview Report," https://datareportal.com/reports/digital-2021-global-overview-report.

32.   R. D. Stedtfeld, D. M. Tourlousse, G. Seyrig, T. M. Stedtfeld, M. Kronlein, S. Price, F.

Ahmad, E. Gulari, J. M. Tiedje, and S. A. Hashsham, "Gene-Z: A device for point of care genetic testing using a smartphone," Lab Chip **12**, 1454–1462 (2012).

33.　T. Laksanasopin, T. W. Guo, S. Nayak, A. A. Sridhara, S. Xie, O. O. Olowookere, P. Cadinu, F. Meng, N. H. Chee, J. Kim, C. D. Chin, E. Munyazesa, P. Mugwaneza, A. J. Rai, V. Mugisha, A. R. Castro, D. Steinmiller, V. Linder, J. E. Justman, S. Nsanzimana, and S. K. Sia, "A smartphone dongle for diagnosis of infectious diseases at the point of care," Sci. Transl. Med. **7**, 273re1 (2015).

34.　L. Shen, J. A. Hagen, and I. Papautsky, "Point-of-care colorimetric detection with a smartphone," Lab Chip **12**, 4240–4243 (2012).

35.　F. Cui, Y. Yue, Y. Zhang, Z. Zhang, and H. S. Zhou, "Advancing Biosensors with Machine Learning," ACS Sensors **5**, 3346–3364 (2020).

36.　K. E. Schackart and J. Y. Yoon, "Machine Learning Enhances the Performance of Bioreceptor-Free Biosensors," Sensors **21**, 5519 (2021).

37.　M. Mafi and A. H. Esmaile, "Inverse design of a high-quality factor multi-purpose optical biosensor," IET Optoelectron. 1–11 (2022).

38.　C. Angermueller, T. Pärnamaa, L. Parts, and O. Stegle, "Deep learning for computational biology," Mol. Syst. Biol. **12**, 878 (2016).

39.　Z. Li, J. R. Askim, and K. S. Suslick, "The Optoelectronic Nose: Colorimetric and Fluorometric Sensor Arrays," Chem. Rev. **119**, 231–292 (2019).

40.　S. Marco and A. Gutierrez-Galvez, "Signal and data processing for machine olfaction and chemical sensing: A review," IEEE Sens. J. **12**, 3189–3214 (2012).

41.　K. Pearson, "On lines and planes of closest fit to systems of points in space," London,

Edinburgh, Dublin Philos. Mag. J. Sci. **2**, 559–572 (1901).

42.   F. Douglas, L. Pat, and R. Fisher, "Methods of Conceptual Clustering and their Relation to Numerical Taxonomy," Ann. Eugen. **7**, 179–188 (1985).

43.   C. C. Chang and C. J. Lin, "LIBSVM: A Library for support vector machines," ACM Trans. Intell. Syst. Technol. **2**, 27 (2011).

44.   E. Fix and J. L. Hodges, "Discriminatory Analysis. Nonparametric Discrimination: Consistency Properties," Int. Stat. Rev. **57**, 238 (1989).

45.   F. Rosenblatt, "The Perceptron — A Perceiving and Recognizing Automaton," Concours médical **84**, 1715–1722 (1962).

46.   J. Mao, "Artificial Neural Networks: A Tutorial," Computer (Long. Beach. Calif). **29**, 31–44 (1996).

47.   T. K. Ho, "Random decision forests," Proc. Int. Conf. Doc. Anal. Recognition, ICDAR **1**, 278–282 (1995).

48.   L. Breiman, "Random Forests," Mach. Learn. **45**, 5–32 (2001).

49.   A. J. A. Nelder, R. W. M. Wedderburn, S. Journal, R. Statistical, and S. Series, "Generalized Linear Models," **135**, 370–384 (1972).

50.   A. Sherstinsky, "Fundamentals of Recurrent Neural Network (RNN) and Long Short-Term Memory (LSTM) network," Phys. D Nonlinear Phenom. **404**, 132306 (2020).

51.   S. Hochreiter and J. Schmidhuber, "Long Short-Term Memory," Neural Comput. **9**, 1735–1780 (1997).

52.   R. Zhao, R. Yan, J. Wang, and K. Mao, "Learning to monitor machine health with convolutional Bi-directional LSTM networks," Sensors (Switzerland) **17**, 1–18 (2017).

53.   F. Weninger, H. Erdogan, S. Watanabe, E. Vincent, J. Le Roux, J. R. Hershey, and B. Schuller, "Speech Enhancement with LSTM Recurrent Neural Networks and its Application to Noise-Robust ASR," in *Brain Research Bulletin* (2015), Vol. 53, pp. 91–99.

54.   X. H. Le, H. V. Ho, G. Lee, and S. Jung, "Application of Long Short-Term Memory (LSTM) neural network for flood forecasting," Water **11**, (2019).

55.   C. Zhou, C. Sun, Z. Liu, and F. C. M. Lau, "A C-LSTM Neural Network for Text Classification," ArXiv **abs/1511.0**, (2015).

56.   J. Homola, "Surface plasmon resonance sensors for detection of chemical and biological species," Chem. Rev. **108**, 462–493 (2008).

57.   J. Xu, X. Luo, and H. Chen, "Analytical Aspects of FET-Based Biosensors," Anal. Chem. **10**, 420–430 (2005).

58.   J. Wang, "Amperometric biosensors for clinical and therapeutic drug monitoring: A review," J. Pharm. Biomed. Anal. **19**, 47–53 (1999).

59.   A. Uhlir, "Electrolytic Shaping of Germanium and Silicon," Bell Syst. Tech. J. **35**, 333–347 (1956).

60.   L. T. Canham, "Silicon quantum wire array fabrication by electrochemical and chemical dissolution of wafers," Appl. Phys. Lett. **57**, 1046–1048 (1990).

61.   V. Lehmann and U. Gösele, "Porous silicon formation: A quantum wire effect," Appl. Phys. Lett. **58**, 856–858 (1991).

62.   A. Jane, R. Dronov, A. Hodges, and N. H. Voelcker, "Porous silicon biosensors on the advance," Trends Biotechnol. **27**, 230–239 (2009).

63.   S. Arshavsky-Graham, N. Massad-Ivanir, E. Segal, and S. Weiss, "Porous Silicon-Based

Photonic Biosensors: Current Status and Emerging Applications," Anal. Chem. **91**, 441–467 (2019).

64.   Y. Zhao, G. Gaur, S. T. Retterer, P. E. Laibinis, and S. M. Weiss, "Flow-through porous silicon membranes for real-time label-free biosensing," Anal. Chem. **88**, 10940–10948 (2016).

65.   S. Arshavsky Graham, E. Boyko, R. Salama, and E. Segal, "Mass Transfer Limitations of Porous Silicon-Based Biosensors for Protein Detection," ACS Sensors **5**, 3058–3069 (2020).

66.   D. Martín-Sánchez, S. Ponce-Alcántara, and J. García-Rupérez, "Sensitivity Comparison of a Self-Standing Porous Silicon Membrane under Flow-Through and Flow-Over Conditions," IEEE Sens. J. **19**, 3276–3281 (2019).

67.   H. H. Nguyen, J. Park, S. Kang, and M. Kim, "Surface plasmon resonance: A versatile technique for biosensor applications," Sensors **15**, 10481–10510 (2015).

68.   R. Moretta, L. De Stefano, M. Terracciano, and I. Rea, "Porous Silicon Optical Devices: Recent Advances in Biosensing Applications," Sensors **21**, 1336 (2021).

69.   W. TheiB, "Optical properties of porous silicon," Solid State Commun. **92**, 101–112 (1994).

70.   J. C. Maxwell Garnett, "Colours in Metal Glasses and in Metallic Films," **203**, 385–420 (1904).

71.   Von D. A. G. Bruggeman, "Berechnung verschiedener physikalischer Konstanten von heterogenen Substanzen. I. Dielektrizitätskonstanten und Leitfähigkeiten der Mischkörper aus isotropen Substanzen," Ann. Phys. **416**, 665–679 (1935).

72.   H. Looyenga, "Dielectric Constants of Heterogenous Mixtures," Mol. Phys. **9**, 501–511 (1965).

73.   C. Pickering, M. I. J. Beale, D. J. Robbins, P. J. Pearson, and R. Greef, "Optical properties of porous silicon films," Thin Solid Films **125**, 157–163 (1985).

74.   E. J. Anglin, M. P. Schwartz, V. P. Ng, L. A. Perelman, and M. J. Sailor, "Engineering the chemistry and nanostructure of porous silicon fabry-pérot films for loading and release of a steroid," Langmuir **20**, 11264–11269 (2004).

75.   M. Khardani, M. Bouaïcha, and B. Bessaïs, "Bruggeman effective medium approach for modelling optical properties of porous silicon: Comparison with experiment," Phys. Status Solidi Curr. Top. Solid State Phys. **4**, 1986–1990 (2007).

76.   E. Hecht, *Optics*, 5th ed. (Pearson, 2017).

77.   C. Pacholski, M. Sartor, M. J. Sailor, F. Cunin, and G. M. Miskelly, "Biosensing using porous silicon double-layer interferometers: Reflective interferometric fourier transform spectroscopy," J. Am. Chem. Soc. **127**, 11636–11645 (2005).

78.   S. J. Ward, R. Layouni, S. Arshavsky-Graham, E. Segal, and S. M. Weiss, "Morlet Wavelet Filtering and Phase Analysis to Reduce the Limit of Detection for Thin Film Optical Biosensors," ACS Sensors **6**, 2967–2978 (2021).

79.   C. J. Jacobus and R. T. Chien, "Two New Edge Detectors," IEEE Trans. Pattern Anal. Mach. Intell. **PAMI**-**3**, 581–592 (1981).

80.   G. G. Nenninger, M. Piliarik, and J. Homola, "Data analysis for optical sensors based on spectroscopy of surface plasmons," Meas. Sci. Technol. **13**, 2038–2046 (2002).

81.   T. M. Chinowsky, L. S. Jung, and S. S. Yee, "Optimal linear data analysis for surface plasmon resonance biosensors," Sensors Actuators, B Chem. **54**, 89–97 (1999).

82.   A. P. F. Turner, "Biosensors: Sense and Sensibility," Chem. Soc. Rev. **42**, 3184–3196

(2013).

83.   S. Ihne, C. Morbach, C. Sommer, A. Geier, S. Knop, and S. Störk, "Amyloidosis—the diagnosis and treatment of an underdiagnosed disease," Dtsch. Arztebl. Int. **117**, 159–166 (2020).

84.   N. Bhalla, P. Jolly, N. Formisano, and P. Estrela, "Introduction to biosensors," Essays Biochem. **60**, 1–8 (2016).

85.   S. Ellison, Stephen L R ; Barwick, Vicki J ; Farrant, Trevor J Duguid ; Hardcastle, William A ; Upton, *Practical Statistics for the Analytical Scientist*, 2nd ed. (RSC, 2009).

86.   O. Lazcka, F. J. Del Campo, and F. X. Muñoz, "Pathogen detection: A perspective of traditional methods and biosensors," Biosens. Bioelectron. **22**, 1205–1217 (2007).

87.   C. Werlen, M. C. M. Jaspers, and J. R. Van Der Meer, "Measurement of Biologically Available Naphthalene in Gas and Aqueous Phases by Use of a Pseudomonas putida Biosensor," Appl. Environ. Microbiol. **70**, 43–51 (2004).

88.   J. Chobtang, I. J. M. de Boer, R. L. A. P. Hoogenboom, W. Haasnoot, A. Kijlstra, and B. G. Meerburg, "The need and potential of biosensors to detect dioxins and dioxin-like polychlorinated biphenyls along the milk, eggs and meat food chain," Sensors **11**, 11692–11716 (2011).

89.   G. Gaur, D. S. Koktysh, and S. M. Weiss, "Immobilization of quantum dots in nanostructured porous silicon films: Characterizations and signal amplification for dual-mode optical biosensing," Adv. Funct. Mater. **23**, 3604–3614 (2013).

90.   R. Layouni, M. Dubrovsky, M. Bao, H. Chung, K. Du, S. V. Boriskina, S. M. Weiss, and Di. Vermeulen, "High contrast reporter cleavage detection for enhancing porous silicon

sensor sensitivity," 2021 Conf. Lasers Electro-Optics, CLEO 2021 - Proc. **29**, 1–11 (2021).

91. W. Wang, X. Wang, N. Cheng, Y. Luo, Y. Lin, W. Xu, and D. Du, "Recent advances in nanomaterials-based electrochemical (bio)sensors for pesticides detection," Trends Anal. Chem. **132**, 116041 (2020).

92. W. Wang, S. Singh, D. L. Zeng, K. King, and S. Nema, "Antibody structure, instability, and formulation," J. Pharm. Sci. **96**, 1–26 (2007).

93. S. Arshavsky-Graham, C. Heuer, X. Jiang, and E. Segal, "Aptasensors versus immunosensors—Which will prevail?," Eng. Life Sci. **22**, 319–333 (2022).

94. F. Ko and S. J. Drews, "The impact of commercial rapid respiratory virus diagnostic tests on patient outcomes and health system utilization," Expert Rev. Mol. Diagn. **17**, 917–931 (2017).

95. A. S. Gritte, K. M. Morneau, C. R. Frei, J. A. Cadena-Zuluaga, E. A. Walter, and T. L. Hopkins, "Clinical impact of implementation of rapid diagnostic testing of blood cultures with Staphylococcus aureus on patient outcomes," Diagn. Microbiol. Infect. Dis. **101**, 115474 (2021).

96. S. Arshavsky-Graham, S. J. Ward, N. Massad-Ivanir, T. Scheper, S. M. Weiss, and E. Segal, "Porous Silicon-Based Aptasensors: Toward Cancer Protein Biomarker Detection," ACS Meas. Sci. Au **1**, 82–94 (2021).

97. J. Sabaté del Río, O. Y. F. Henry, P. Jolly, and D. E. Ingber, "An antifouling coating that enables affinity-based electrochemical biosensing in complex biological fluids," Nat. Nanotechnol. **14**, 1143–1149 (2019).

98. N. Wisniewski and M. Reichert, "Methods for reducing biosensor membrane biofouling,"

Colloids Surfaces B Biointerfaces **18**, 197–219 (2000).

99.   J. Y. Lichtenberg, Y. Ling, and S. Kim, "Non-specific adsorption reduction methods in biosensing," Sensors (Switzerland) **19**, 1–17 (2019).

100.   L. Buck and R. Axel, "A novel multigene family may encode odorant receptors: A molecular basis for odor recognition," Cell **65**, 175–187 (1991).

101.   R. Axel, "The Molecular Logic of Smell," Sci. Am. **273**, 154–159 (1995).

102.   C. Bushdid, M. O. Magnasco, L. B. Vosshall, and A. Keller, "Humans Can Discriminate More than 1 Trillion Olfactory Stimuli," Science (80-.). **343**, 1370–1372 (2014).

103.   T. T. Dung, Y. Oh, S.-J. Choi, I.-D. Kim, M.-K. Oh, and M. Kim, "Applications and Advances in Bioelectronic Noses for Odour Sensing," Sensors **18**, 103 (2018).

104.   N. A. Rakow and K. S. Suslick, "A Colorimetric Sensor Array For Odour Visualization," Nature **406**, 710–713 (2000).

105.   J. R. Stetter, P. C. Jurs, and S. L. Rose, "Detection of Hazardous Gases and Vapors: Pattern Recognition Analysis of Data from an Electrochemical Sensor Array," Anal. Chem. **58**, 860–866 (1986).

106.   K. Persaud and G. Dodd, "Analysis of Discrimination Mechanisms in the Mammalian Olfactory System Using a Model Nose," Nature **299**, 352–355 (1982).

107.   W. Patrick Carey, K. R. Beebe, B. R. Kowalski, D. L. Illman, and T. Hirschfeld, "Selection of Adsorbates for Chemical Sensor Arrays by Pattern Recognition," Anal. Chem. **58**, 149–153 (1986).

108.   D. S. Ballantine, S. L. Rose, J. W. Grate, and H. Wohltjen, "Correlation of Surface Acoustic Wave Device Coating Responses with Solubility Properties and Chemical Structure Using

Pattern Recognition," Anal. Chem. **58**, 3058–3066 (1986).

109.   S. Lee, H. Huang, and M. Zelen, "Early detection of disease and scheduling of screening examinations," Stat. Methods Med. Res. **13**, 443–456 (2004).

110.   B. P. Lanphear, "Low-level toxicity of chemicals: No acceptable levels?," PLoS Biol. **15**, 1–8 (2017).

111.   S. Sjölander and C. Urbaniczky, "Integrated Fluid Handling System for Biomolecular Interaction Analysis," Anal. Chem. **63**, 2338–2345 (1991).

112.   C. Thirstrup and W. Zong, "Data analysis for surface plasmon resonance sensors using dynamic baseline algorithm," Sensors Actuators, B Chem. **106**, 796–802 (2005).

113.   K. S. Johnston, S. S. Yee, and K. S. Booksh, "Calibration of Surface Plasmon Resonance Refractometers Using Locally Weighted Parametric Regression," Anal. Chem. **69**, 1844–1851 (1997).

114.   A. Karabchevsky, S. Karabchevsky, and I. Abdulhalim, "Fast surface plasmon resonance imaging sensor using Radon transform," Sensors Actuators, B Chem. **155**, 361–365 (2011).

115.   A. Zhou and Y. Q. Chen, "Fractional order processing of quartz crystal microbalance based DNA biosensor signals," IFAC Proc. Vol. **2**, 188–193 (2006).

116.   S. C. Chang, I. J. Chao, B. Da Liu, C. Y. Huang, M. H. Lee, and H. Y. Lin, "Design of a signal processing circuit for quartz crystal microbalance biosensors," in *Proceedings of International Conference on ASIC* (IEEE, 2011), pp. 180–183.

117.   S. N. Songkhla and T. Nakamoto, "Signal Processing of Vector Network Analyzer Measurement for Quartz Crystal Microbalance with Viscous Damping," IEEE Sens. J. **19**, 10386–10392 (2019).

118. J. Su, A. F. G. Goldberg, and B. M. Stoltz, "Label-free detection of single nanoparticles and biological molecules using microtoroid optical resonators," Light Sci. Appl. **5**, 1–7 (2016).

119. H. P. Pien, W. C. Karl, D. Puff, P. Li, and B. Cunningham, "Method and apparatus for biosensor spectral shift detection," U.S. patent US7718440B2 (2007).

120. S. Mariani, L. Pino, L. M. Strambini, L. Tedeschi, and G. Barillaro, "10 000-Fold Improvement in Protein Detection Using Nanostructured Porous Silicon Interferometric Aptasensors," ACS Sensors **1**, 1471–1479 (2016).

121. S. Mariani, L. M. Strambini, and G. Barillaro, "Femtomole Detection of Proteins Using a Label-Free Nanostructured Porous Silicon Interferometer for Perspective Ultrasensitive Biosensing," Anal. Chem. **88**, 8502–8509 (2016).

122. C. Pacholski, "Photonic crystal sensors based on porous silicon," Sensors (Switzerland) **13**, 4694–4713 (2013).

123. S. J. Schiff, A. Aldroubi, M. Unser, and S. Sato, "Fast wavelet transformation of EEG," Electroencephalogr. Clin. Neurophysiol. **91**, 442–455 (1994).

124. P. Goupillaud, A. Grossmann, and J. Morlet, "Cycle-octave and related transforms in seismic signal analysis," Geoexploration **23**, 85–102 (1984).

125. S. J. Ward and S. M. Weiss, "Reducing detection limits of porous silicon thin film optical sensors using signal processing," Proc. SPIE **11662**, (2021).

126. C. Huang, W. Jing, K. Liu, Y. Zhang, and G. D. Peng, "Demodulation of fiber bragg grating sensor using cross-correlation algorithm," IEEE Photonics Technol. Lett. **19**, 707–709 (2007).

127. Y. Wang, P. Li, J. Zhang, X. Liu, Q. Bai, D. Wang, M. Zhang, and B. Jin, "Distributed optical fiber vibration sensor using generalized cross-correlation algorithm," Meas. J. Int. Meas. Confed. **144**, 58–66 (2019).

128. R. O. Schmidt, "Multiple emitter location and signal parameter estimation," Adapt. Antennas Wirel. Commun. **34**, 190–194 (2009).

129. F. Shen and A. Wang, "Frequency-estimation-based signal-processing algorithm for white-light optical fiber Fabry – Perot interferometers," Appl. Opt. **44**, 5206–14 (2005).

130. R. Lawrence and B. Gold, *Theory and Application of Digital Signal Processing*, 1st ed. (Prentice-Hall Inc., 1975).

131. D. Sundararajan, *Discrete Wavelet Transform : A Signal Processing Approach*, 1st ed. (Wiley, 2015).

132. M. X. Cohen, "A better way to define and describe Morlet wavelets for time-frequency analysis," Neuroimage **199**, 81–86 (2019).

133. Weiss Group, "Morlet Wavelet Phase Application," (2021).

134. E. Xifré-Pérez, J. Ferré-Borrull, J. Pallarés, and L. F. Marsal, "Methods, properties and applications of porous silicon," in *Springer Series in Materials Science*, D. Losic and A. Santos, eds. (Springer, 2015), Vol. 220, pp. 37–63.

135. A. Janshoff, K. S. Dancil, C. Steinem, D. P. Greiner, V. S. Lin, C. Gurtner, K. Motesharei, M. J. Sailor, and M. R. Ghadiri, "Macroporous p-Type Silicon Fabry-Perot Layers . Fabrication, Characterization, and Applications in Biosensing," J. Am. Chem. Soc. **120**, 12108–12116 (1998).

136. K. Urmann, J. G. Walter, T. Scheper, and E. Segal, "Label-free optical biosensors based on

aptamer-functionalized porous silicon scaffolds," Anal. Chem. **87**, 1999–2006 (2015).

137. E. Tenenbaum, N. Ben-Dov, and E. Segal, "Tethered lipid bilayers within porous Si nanostructures: A platform for (optical) real-time monitoring of membrane-associated processes," Langmuir **31**, 5244–5251 (2015).

138. K. Urmann, P. Reich, J. G. Walter, D. Beckmann, E. Segal, and T. Scheper, "Rapid and label-free detection of protein a by aptamer-tethered porous silicon nanostructures," J. Biotechnol. **257**, 171–177 (2017).

139. A. Ukil and A. Bärlocher, "Implementation of discrete wavelet transform for embedded applications using TMS320VC5510," in *2007 Symposium on Industrial Embedded Systems Proceeedings* (2007), pp. 357–360.

140. M. A. Al-Ghouti and D. A. Da'ana, "Guidelines for the use and interpretation of adsorption isotherm models: A review," J. Hazard. Mater. **393**, 122383 (2020).

141. V. Gold, ed., *The IUPAC Compendium of Chemical Terminology* (International Union of Pure and Applied Chemistry (IUPAC), 2019).

142. J. Wu, C. Wang, X. Li, Y. Song, W. Wang, C. Li, J. Hu, Z. Zhu, J. Li, W. Zhang, Z. Lu, and C. J. Yang, "Identification, Characterization and Application of a G-Quadruplex Structured DNA Aptamer against Cancer Biomarker Protein Anterior Gradient Homolog 2," PLoS One **7**, e46393 (2012).

143. M. G. Sande, J. L. Rodrigues, D. Ferreira, C. J. Silva, and L. R. Rodrigues, "Novel biorecognition elements against pathogens in the design of state-of-the-art diagnostics," Biosensors **11**, 418 (2021).

144. T. Kodadek, "Protein microarrays: Prospects and problems," Chem. Biol. **8**, 105–115

(2001).

145. C. Di Natale, E. Battista, V. Lettera, N. Reddy, G. Pitingolo, R. Vecchione, F. Causa, and P. A. Netti, "Easy Surface Functionalization and Bioconjugation of Peptides as Capture Agents of a Microfluidic Biosensing Platform for Multiplex Assay in Serum," Bioconjug. Chem. **32**, 1593–1601 (2021).

146. H. J. Byrne, F. Bonnier, J. McIntyre, and D. R. Parachalil, "Quantitative Analysis of Human Blood Serum using Vibrational Spectroscopy," Clin. Spectrosc. **2**, 100004 (2020).

147. L. Chen, X. Wang, W. Lu, X. Wu, and J. Li, "Molecular imprinting: Perspectives and applications," Chem. Soc. Rev. **45**, 2137–2211 (2016).

148. L. Uzun and A. P. F. Turner, "Molecularly-imprinted polymer sensors: Realising their potential," Biosens. Bioelectron. **76**, 131–144 (2016).

149. C. Zhang and K. S. Suslick, "A Colorimetric Sensor Array for Organics in Water," J. Am. Chem. Soc. **127**, 11548–11549 (2005).

150. M. De, S. Rana, H. Akpinar, O. R. Miranda, R. R. Arvizo, U. H. F. Bunz, and V. M. Rotello, "Sensing of proteins in human serum using conjugates of nanoparticles and green fluorescent protein," Nat. Chem. **1**, 461–465 (2009).

151. J. Han, H. Cheng, B. Wang, M. S. Braun, X. Fan, M. Bender, W. Huang, C. Domhan, W. Mier, T. Lindner, K. Seehafer, M. Wink, and U. H. F. Bunz, "A Polymer/Peptide Complex-Based Sensor Array That Discriminates Bacteria in Urine," Angew. Chemie - Int. Ed. **56**, 15246–15251 (2017).

152. J. Han, C. Ma, B. Wang, M. Bender, M. Bojanowski, M. Hergert, K. Seehafer, A. Herrmann, and U. H. F. Bunz, "A Hypothesis-Free Sensor Array Discriminates Whiskies for Brand,

Age, and Taste," Chem **2**, 817–824 (2017).

153.   L. Feng, X. Li, H. Li, W. Yang, L. Chen, and Y. Guan, "Enhancement of sensitivity of paper-based sensor array for the identification of heavy-metal ions," Anal. Chim. Acta **780**, 74–80 (2013).

154.   W. J. Peveler, A. Roldan, N. Hollingsworth, M. J. Porter, and I. P. Parkin, "Multichannel detection and differentiation of explosives with a quantum dot array," ACS Nano **10**, 1139– 1146 (2016).

155.   J. Dian, A. Macek, D. Nižňanský, I. Němec, V. Vrkoslav, T. Chvojka, and I. Jelínek, "SEM and HRTEM study of porous silicon - Relationship between fabrication, morphology and optical properties," Appl. Surf. Sci. **238**, 169–174 (2004).

156.   R. Herino, G. Bomchil, K. Barla, C. Bertrand, and J. L. Ginoux, "Porosity and Pore Size Distributions of Porous Silicon Layers," J. Electrochem. Soc. **134**, 1994–2000 (1987).

157.   P. Granitzer and K. Rumpf, "Porous silicon-a versatile host material," Materials (Basel). **3**, 943–998 (2010).

158.   F. C. Goodland, "Detection Limits for Protein after Electrophoresis on Cellulose Acetate," Ann. Clin. Biochem. **19**, 117–119 (1982).

159.   D. F. Keren, "Proteins in Serum Identified by High-Resolution Electrophoresis," in *High-Resolution Electrophoresis and Immunofixation*, 2nd ed. (Elsevier, 1994), pp. 41–96.

160.   A. K. Y. Tsui, D. Thomas, A. Hunt, M. Estey, C. Lou Christensen, T. Higgins, I. Sandhu, and K. Rodriguez-Capote, "Analytical sensitivity and diagnostic performance of serum protein electrophoresis on the HYDRAGEL 30 PROTEIN(E) β1-β2 Sebia Hydrasys system," Clin. Biochem. **51**, 80–84 (2018).

161.   F. Dai, J. Zai, R. Yi, M. L. Gordin, H. Sohn, S. Chen, and D. Wang, "Bottom-up synthesis of high surface area mesoporous crystalline silicon and evaluation of its hydrogen evolution performance," Nat. Commun. **5**, (2014).

162.   Weiss Group, "Pore Size Distribution MATLAB Code," https://my.vanderbilt.edu/vuphotonics/resources.

163.   P. Elia, E. Nativ-Roth, Y. Zeiri, and Z. Porat, "Determination of the average pore-size and total porosity in porous silicon layers by image processing of SEM micrographs," Microporous Mesoporous Mater. **225**, 465–471 (2016).

164.   K. Zuiderveld, "Contrast Limited Adaptive Histogram Equalization," in *Graphics Gems*, P. S. Heckbert, ed., 4th ed. (Morgan Kaufmann, 1994), pp. 474–485.

165.   F. Pedregosa, G. Varoquaux, A. Gramfort, V. Michel, B. Thirion, O. Grisel, M. Blondel, P. Prettenhofer, R. Weiss, V. Dubourg, J. Vanderplas, A. Passos, D. Cournapeau, M. Brucher, M. Perrot, and E. Duchesnay, "Scikit-learn: Machine Learning in Python," J. Mach. Learn. Res. **12**, 2825–2830 (2011).

166.   C. M. Bishop, *Pattern Recognition and Machine Learning* (Springer, 2007), Vol. 1.

167.   Y. He, D. Bourrier, E. Imbernon, and T. Leichle, "Lateral porous silicon membranes with size and charge selectivity," in *2017 IEEE 12th International Conference on Nano/Micro Engineered and Molecular Systems (NEMS)* (2017), pp. 770–773.

168.   R. S. Dubey and D. K. Gautam, "Fabrication and characterization of porous silicon layers for applications in optoelectronics," Opt. Quantum Electron. **41**, 189–201 (2009).

169.   R. L. Smith and S. D. Collins, "Porous silicon formation mechanisms," J. Appl. Phys. **71**, R1–R22 (1992).

170.   Y. Zhao, G. Gaur, R. L. Mernaugh, P. E. Laibinis, and S. M. Weiss, "Comparative Kinetic Analysis of Closed-Ended and Open-Ended Porous Sensors," Nanoscale Res. Lett. **11**, (2016).

171.   D. Nadarassan, "Biomolecule Adsorption and Release from Porous Silicon," in *Handbook of Porous Silicon*, L. Canham, ed. (Springer, 2016), pp. 1–18.

172.   M. Y. Chen and M. J. Sailor, "Charge-gated transport of proteins in nanostructured optical films of mesoporous silica," Anal. Chem. **83**, 7186–7193 (2011).

173.   G. A. Parks, "The Isoelectric Points of Solid Oxides, Solid Hydroxides, and Aqueous Hydroxo Complex Systems," Chem. Rev. **65**, 177–198 (1965).

174.   A. Wada and H. Nakamura, "Nature of the Charge Distribution in Proteins," Nature **293**, 757–758 (1981).

175.   M. Bhattacharya, N. Jain, K. Bhasne, V. Kumari, and S. Mukhopadhyay, "pH-induced Conformational Isomerization of Bovine Serum Albumin Studied by Extrinsic and Intrinsic Protein Fluorescence," J. Fluoresc. **21**, 1083–1090 (2011).

176.   O. Redlich and D. L. Peterson, "A Useful Adsorption Isotherm," J. Phys. Chem. **63**, 1024 (1959).

177.   C. K. Tsang, T. L. Kelly, M. J. Sailor, and Y. Y. Li, "Highly stable porous silicon-carbon composites as label-free optical biosensors," ACS Nano **6**, 10546–10554 (2012).

178.   T. Cao, Y. Zhao, C. A. Nattoo, R. Layouni, and S. M. Weiss, "A smartphone biosensor based on analysing structural colour of porous silicon," Analyst **144**, 3942–3948 (2019).

179.   P. Valenstein, "Laboratory turnaround time," Am. J. Clin. Pathol. **105**, 676–688 (1996).

180.   J. Barenfanger, C. Drake, N. Leon, T. Mueller, and T. Troutt, "Clinical and financial

benefits of rapid detection of respiratory viruses: An outcomes study," J. Clin. Microbiol. **38**, 2824–2828 (2000).

181. B. B. Rogers, P. Shankar, R. C. Jerris, D. Kotzbauer, E. J. Anderson, J. R. Watson, L. A. O'Brien, F. Uwindatwa, K. McNamara, and J. E. Bost, "Impact of a rapid respiratory panel test on patient outcomes," Arch. Pathol. Lab. Med. **139**, 636–641 (2015).

182. J. Wang and H. Yue, "Food safety pre-warning system based on data mining for a sustainable food supply chain," Food Control **73**, 223–229 (2017).

183. Z. Q. Geng, S. S. Zhao, G. C. Tao, and Y. M. Han, "Early warning modeling and analysis based on analytic hierarchy process integrated extreme learning machine (AHP-ELM): Application to food safety," Food Control **78**, 33–42 (2017).

184. J. Chang, H. Meng, C. Li, J. Gao, S. Chen, Q. Hu, H. Li, and L. Feng, "A Wearable Toxic Gas-Monitoring Device Based on Triboelectric Nanogenerator for Self-Powered Aniline Early Warning," Adv. Mater. Technol. **5**, 1–9 (2020).

185. J. Hellou, "Behavioural ecotoxicology, an "early warning" signal to assess environmental quality," Environ. Sci. Pollut. Res. **18**, 1–11 (2011).

186. F. Long, A. Zhu, and H. Shi, "Recent advances in optical biosensors for environmental monitoring and early warning," Sensors (Switzerland) **13**, 13928–13948 (2013).

187. Z. Li, S. Yan, Z. Wu, H. Li, J. Wang, W. Shen, Z. Wang, and Y. Q. Fu, "Hydrogen gas sensor based on mesoporous In2O3 with fast response/recovery and ppb level detection limit," Int. J. Hydrogen Energy **43**, 22746–22755 (2018).

188. L. T. Duy, T. Q. Trung, V. Q. Dang, B. U. Hwang, S. Siddiqui, I. Y. Son, S. K. Yoon, D. J. Chung, and N. E. Lee, "Flexible Transparent Reduced Graphene Oxide Sensor Coupled

with Organic Dye Molecules for Rapid Dual-Mode Ammonia Gas Detection," Adv. Funct. Mater. **26**, 4329–4338 (2016).

189. X. Meng, M. Bi, Q. Xiao, and W. Gao, "Ultra-fast response and highly selectivity hydrogen gas sensor based on Pd/SnO2 nanoparticles," Int. J. Hydrogen Energy **47**, 3157–3169 (2022).

190. I. Jokić, Z. Djurić, K. Radulović, M. Frantlović, G. V. Milovanović, and P. M. Krstajić, "Stochastic time response and ultimate noise performance of adsorption-based microfluidic biosensors," Biosensors **11**, (2021).

191. M. R. Leyden, R. J. Messinger, C. Schuman, T. Sharf, V. T. Remcho, T. M. Squires, and E. D. Minot, "Increasing the detection speed of an all-electronic real-time biosensor," Lab Chip **12**, 954–959 (2012).

192. D. Soni, D. Sharma, M. Aslam, and S. Yadav, "Approach for the improvement of sensitivity and sensing speed of TFET-based biosensor by using plasma formation concept," Micro Nano Lett. **13**, 1728–1733 (2018).

193. O. Akhavan and E. Ghaderi, "Copper oxide nanoflakes as highly sensitive and fast response self-sterilizing biosensors," J. Mater. Chem. **21**, 12935–12940 (2011).

194. J. Lu, I. Do, L. T. Drzal, R. M. Worden, and I. Lee, "Nanometal-decorated exfoliated graphite nanoplatelet based glucose biosensors with high sensitivity and fast response," ACS Nano **2**, 1825–1832 (2008).

195. L. Soleymani and F. Li, "Mechanistic Challenges and Advantages of Biosensor Miniaturization into the Nanoscale," ACS Sensors **2**, 458–467 (2017).

196. R. Pohle, "Transient operation techniques for gas sensor applications," Procedia Eng. **47**, 1466–1473 (2012).

197. X. Pan, X. Zhao, J. Chen, A. Bermak, and Z. Fan, "A fast-response/recovery ZnO hierarchical nanostructure based gas sensor with ultra-high room-temperature output response," Sensors Actuators, B Chem. **206**, 764–771 (2015).

198. L. Zhihua, Z. Xucheng, S. Jiyong, Z. Xiaobo, H. Xiaowei, H. E. Tahir, and M. Holmes, "Fast response ammonia sensor based on porous thin film of polyaniline/sulfonated nickel phthalocyanine composites," Sensors Actuators, B Chem. **226**, 553–562 (2016).

199. J. Zhang, P. Srivatsa, F. H. Ahmadzai, Y. Liu, X. Song, A. Karpatne, Z. Kong, and B. N. Johnson, "Reduction of Biosensor False Responses and Time Delay Using Dynamic Response and Theory-Guided Machine Learning," ACS Sensors **8**, 4079–4090 (2023).

200. J. Burgues and S. Marco, "Wind-independent estimation of gas source distance from transient features of metal oxide sensor signals," IEEE Access **7**, 140460–140469 (2019).

201. M. K. Muezzinoglu, A. Vergara, R. Huerta, N. Rulkov, M. I. Rabinovich, A. Selverston, and H. D. I. Abarbanel, "Acceleration of chemo-sensory information processing using transient features," Sensors Actuators, B Chem. **137**, 507–512 (2009).

202. I. Publishing, M. Siadat, E. Losson, D. Ahmadou, and M. Lumbreras, "Detection Optimization Using a Transient Feature from a Metal Oxide Gas Sensor Array," **27**, 340–346 (2014).

203. M. Siadat, H. Sambemana, and M. Lumbrerasa, "New transient feature for metal oxide gas sensor response processing," Procedia Eng. **47**, 52–55 (2012).

204. S. Kanaparthi and S. G. Singh, "Reduction of the Measurement Time of a Chemiresistive Gas Sensor Using Transient Analysis and the Cantor Pairing Function," ACS Meas. Sci. Au **2**, 113–119 (2022).

205.   D. Ziaian, P. Rostalski, A. E. Berggreen, S. Brandt, M. Grossherr, H. Gehring, A. Hengstenberg, and S. Zimmermann, "Improving Systems Dynamics by Means of Advanced Signal Processing – Mathematical , Laboratorial and Clinical Evaluation of Propofol Monitoring in Breathing Gas," Sensors & Transducers **193**, 145–153 (2015).

206.   D. L. Osorio-Arrieta, J. L. Muñoz-Mata, G. Beltrán-Pérez, J. Castillo-Mixcóatl, C. O. Mendoza-Barrera, V. Altuzar-Aguilar, and S. Muñoz-Aguirre, "Reduction of the measurement time by the prediction of the steady-state response for quartz crystal microbalance gas sensors," Sensors **18**, (2018).

207.   J. Fonollosa, S. Sheik, R. Huerta, and S. Marco, "Reservoir computing compensates slow response of chemosensor arrays exposed to fast varying gas concentrations in continuous monitoring," Sensors Actuators, B Chem. **215**, 618–629 (2015).

208.   Q. Zhang, S. Li, W. Tang, and X. Guo, "Fast Measurement with Chemical Sensors Based on Sliding Window Sampling and Mixed-Feature Extraction," IEEE Sens. J. **20**, 8740–8745 (2020).

209.   J. Lee, H. Hong, J. M. Song, and E. Yeom, "Neural network ensemble model for prediction of erythrocyte sedimentation rate (ESR) using partial least squares regression," Sci. Rep. **12**, 1–13 (2022).

210.   J. Culic Gambiroza, T. Mastelic, T. Kovacevic, and M. Cagalj, "Predicting Low-Cost Gas Sensor Readings from Transients Using Long Short-Term Memory Neural Networks," IEEE Internet Things J. **7**, 8451–8461 (2020).

211.   M. Abdar, F. Pourpanah, S. Hussain, D. Rezazadegan, and L. Liu, "A review of uncertainty quantification in deep learning: Techniques , applications and challenges," Inf. Fusion **76**,

243–297 (2021).

212.   B. Lakshminarayanan, A. Pritzel, and C. Blundell, "Simple and scalable predictive uncertainty estimation using deep ensembles," in *Proceedings of the 31st International Conference on Neural Information Processing Systems (NIPS'17)* (2017), pp. 6403–6414.

213.   G. Rong, A. Najmaie, J. E. Sipe, and S. M. Weiss, "Nanoscale porous silicon waveguide for label-free DNA sensing," **23**, 1572–1576 (2008).

214.   G. Di, V. La, S. Manzo, and S. Chiavarini, "Towards a label-free optical porous silicon DNA sensor," **21**, 661–665 (2005).

215.   O. Syshchyk, V. A. Skryshevsky, O. O. Soldatkin, and A. P. Soldatkin, "Enzyme biosensor systems based on porous silicon photoluminescence for detection of glucose, urea and heavy metals," Biosens. Bioelectron. **66**, 89–94 (2015).

216.   N. Massad-Ivanir, G. Shtenberg, N. Raz, C. Gazenbeek, D. Budding, M. P. Bos, and E. Segal, "Porous Silicon-Based Biosensors: Towards Real-Time Optical Detection of Target Bacteria in the Food Industry," Sci. Rep. **6**, (2016).

217.   S. J. Ward, T. Cao, X. Zhou, C. Chang, and S. M. Weiss, "Protein Identification and Quantification Using Porous Silicon Arrays, Optical Measurements , and Machine Learning," Biosensors **13**, 1–12 (2023).

218.   I. Rea, E. Orabona, A. Lamberti, I. Rendina, and L. De Stefano, "A microfluidics assisted porous silicon array for optical label-free biochemical sensing," Biomicrofluidics **5**, 1–10 (2011).

219.   S. Arshavsky-Graham, A. Enders, S. Ackerman, J. Bahnemann, and E. Segal, "3D-printed microfluidics integrated with optical nanostructured porous aptasensors for protein

detection," Microchim. Acta **188**, (2021).

220.   D. J. C. MacKay, "Probable networks and plausible predictions - a review of practical Bayesian methods for supervised neural networks," Netw. Comput. neural Syst. **6**, 469–505 (1995).

221.   N. Metropolis, A. W. Rosenbluth, M. N. Rosenbluth, A. H. Teller, and E. Teller, "Equation of State Calculations by Fast Computing Machines," (2004).

222.   F. Chollet and others, "Keras," (2015).

223.   L. K. Hansen and P. Salamon, "Neural network ensembles," IEEE Trans. Pattern Anal. Mach. Intell. **12**, 993–1001 (1990).

224.   D. P. Kingma and J. L. Ba, "Adam: A method for stochastic optimization," ArXiv **abs/1412.6**, 1–15 (2015).